Imperial College Thesis

Name of Author:_Martin Cloke_ Year:__2004____

Imperial College
of Science, Technology and Medicine

Martin Cloke

Vortical equilibria of the Euler equations: construction and stability

---

A thesis presented for the degree of
Doctor of Philosophy of the University of London
and the
Diploma of Imperial College
London 2004

Abstract

The subject of this thesis is exact solutions of the two-dimensional inviscid Euler equations, consisting of both finite area vorticity and point vorticity, based on a method of Crowdy [3]. There are only a small number of exact finite area vortex distributions known at present, so these solutions are naturally of interest. In addition, this thesis broadly aims to show that solutions produced by this method are valuable as models of known atmospheric and electromagnetic phenomena. To this end, new classes of solution are presented, both on the sphere and on the plane, and the stability of solutions created using this method is examined.

The solutions derived utilize the Schwarz function of some domain to combine a patch of constant vorticity with some array of point vortices. We show that these solutions behave in a manner consistent with physically observed coherent vortical structures, and also argue that the form of an isolated point vortex on the sphere motivates the combination of patch and point vorticity.

The content is divided into chapters detailing the process of obtaining solutions and chapters analysing the stability of the solutions. An existing class of multipolar planar solutions, derived using the Crowdy Schwarz function method, is reviewed and then the linear stability of these planar structures examined. Also for this case, a contour dynamics code is used to examine evolution of the structure under various perturbations and these results are compared with results of numerical and physical studies. The methods used to construct the planar solutions is then extended to the surface of the sphere, utilizing a stereographic projection from the complex plane. An analogous class of solutions lying on the surface of a sphere is hence obtained. The stability of this class of solutions on the surface of the sphere will be examined and compared with simpler spherical results. Finally, a class of solutions on the plane is presented which possesses a singly periodic vortex patch with superposed line vortices. This is created by considering the Schwarz function associated with a quasi-loxodromic conformal map.

In loving memory of my father, John Cloke.

Acknowledgments

I would like to acknowledge the help and supervision of Dr Darren Crowdy during my PhD studies, and additionally the EPSRC for their funding. I would also like to thank my parents and siblings for their multifarious and unstinting support throughout, without which I plainly would not have submitted. Finally, I would very much like to thank my all my friends for entertaining me, and particularly William, Matthew, James, Joanna, Nick, Pete, Tom, Ruth and Hannah for doing so well beyond the call of duty. They have all made the years I have spent completing my thesis immeasurably more worthwhile. I would additionally like to thank Nick for taking the time to read my thesis and criticise my use of English!

Contents

List of Figures

List of Tables

CHAPTER 1

Introduction

1.1 Background

In the last 20 years, considerable interest has arisen in the coherent vortical structures occurring in inviscid fluid mechanics. These are long-lived, horizontally recirculating fluid motions through closed streamlines of compact size. These structures play an essential role in transient flows, such as unstable ocean currents [1], or two-dimensional turbulence [2]. It has been known for some time that these are important in the dynamics of large scale fluid systems, such as the Gulf Stream rings, and the 'spots' on Jupiter.

The simplest and most commonly observed of these structures is the monopolar vortex. The interactions of pairs of monopoles with opposite signs can give rise to dipoles, structures which are best described as a self-propelling compound vortex. Flierl [17] shows how baroclinic two-contour Rankine vortices can form more complex vortical structures, or break down into pairs of dipoles. More complex structures have also been observed, in meteorological data, laboratory experiments and in numerical simulations. One of the more common of these complex structures, observed in [7], [8], [10], [11], is the *multipolar vortex.*

Multipolar vortices can be defined using the following qualitative features:

1. Multipolar vortices are isolated *finite-area* regions of nonzero vorticity surrounded by irrotational flow;
2. The vorticity distribution of multipolar vortex of order n is characterised by a central core vortex of one sign, surrounded by a distribution of n satellite vortices, all of opposite polarity from the central region;
3. They are steadily-rotating with a constant angular velocity Ω;

4. The approximate shape of a multipolar structure of order n (for $n \geq 3$) is an n-polygonal core region with n semicircular satellite regions on each side of the central polygon;

5. The multipolar structures calculated in numerical simulations often have zero total circulation since they are frequently generated by the instability of zero circulation monopolar vortices;

6. The streamline patterns in the vortical region typically display saddle points joined by separatrix streamlines, as well as regions of closed streamlines.

1.2 Literature

1.2.1 Known finite area exact solutions

Only a small number of solutions of the two-dimensional Euler equations are known which have finite area vortex distribution. The simplest of these is the Rankine vortex, a circular region of vorticity surrounded by irrotational flow. A more interesting distribution is the Kirchoff elliptical vortex, a region of constant vorticity, bounded by an ellipse rotating with constant angular velocity(see Lamb, [39]§159). As the ratio between the major and minor axes tends to unity, the Kirchoff vortex can be viewed as a perturbation to the boundary of the Rankine vortex. Moore and Saffman [6] generalised this to include a steady straining flow exterior to the patch. The Rankine, Kirchoff and Moore-Saffman results are the only known exact steady solutions for uniform vortex patches.

1.2.2 Multipolar Papers

Following observations in meteorological data in the early 1980s, a series of papers appeared detailing approaches to modeling multipolar vortices, both experimentally and numerically. The most common method used to produce multipolar equilibria, in both laboratory and numerical experiments, is to destabilise a monopolar vortex structure through azimuthal perturbations into a distribution with a distributed vorticity with at least 3 maxima of vorticity, of alternating polarity. It has been also possible to form higher order equilibria, through stronger perturbations of vortices. Some of these forms, particularly the tripole and quadrupole, having three and four vortical maxima respectively, appear to be relatively common dynamical attractors.

Polvani and Carton, in their 1990 paper [11], were the first to reproduce the tripole numerically, using a contour dynamics code. Their model consists of patch vorticity, also called V-states, and rotating multipolar steady states are obtained using a relaxation algorithm. The speed of rotation and evolution of small patches is compared with a purely point vortex model, and the results are found to correspond. Stability analysis is carried out on these steady states using contour dynamics and a pseudo-spectral code. In conclusion, they find that the majority of the parameter space for their structures is stable, and any unstable structures break down into asymmetric dipoles of a shielded axisymmetric vortex. They remark that the formation and breakdown of multipolar vortices may well be a reversible transition.

Carneval and Kloosterziel, in their 1994 paper [7] create multipolar vortices in laboratory conditions, and then model them numerically. The laboratory multipolar vortex is formed by the use of a rotating tank filled with dyed fluid. A circular dividing barrier is placed in the tank, and within the barrier, anti-cyclonic vorticity is induced. When the barrier is removed, the two regions mix. The fluid is filmed, and the marks enable streak-lines to be followed, and vorticity fields to be calculated. If the barrier is perturbed with some symmetric perturbations, then the resulting form can evolve to a multipolar structure. Although the tank has significant depth, it is shown in [22] that rotation effects cause the flow to become quasi-two-dimensional. Carnevale and Kloosterziel find it is possible to form robust quadrupole vortices in this manner, and higher order multipoles for short time periods. As the experiment is fully three dimensional, this shows these structures are indeed physically present using these initial conditions, and not merely artifacts produced by taking the two dimensional limit of the Euler equations. After several rotation periods, the quadrupole vortices break down into a pair of dipoles travelling in opposite directions. Also in this paper, a numerical multipolar vortex simulation is examined. Adding dissipation terms to the vorticity equation, they aim to reproduce the laboratory results using patch vortices. To this end, a two-contour Rankine vortex is perturbed azimuthally at some wavenumber, and time evolved to create rotating quadrupoles or higher multipoles. They find it easier to produce quadrupoles than higher order multipoles using this method. The quadrupole is found to be a more robust structure than higher order structures. The stability results from these patch vortex models are compared with the point vortex limit, and found to be qualitatively the same.

Morel and Carton [18] also published on the stability of multipolar vortices. Their paper is entirely numerical and concentrates on an investigation of barotropic instability. They find it is possible to produce multipolar vortices from three-contour Rankine vortices. They utilise a relaxation algorithm of [31]. Once this algorithm reaches a steady state, stability is examined using contour surgery and pseudo-spectral methods. They conclude that quadrupoles are relatively robust, while higher order multipoles degenerate quickly. Interestingly, they consider only vortex structures with zero total circulation, stating that their study of non-zero circulation models shows they do not exhibit significant differences [18].

1.2.3 Tornado models

Similar structures have also been observed in tornado dynamics. In [43], Snow notes that a characteristic of tornadoes is often a central core of vorticity surrounded by up to six outer regions of vorticity of an opposite sign. In additions, he notes that tornados possess vorticity at two different scales, a large outer region of low vorticity and a small region of extremely high vorticity.

A numerical paper by Shian-Jiann Lin [42] also uses the methods of contour dynamics to perturb a variety of multi-contour Rankine vortices to create a multipolar model of tornado behaviour. He also presents a contour dynamics simulation of a large region of low vorticity with a superposed small region of high vorticity. This is shown to entrain boundary elements as it numerically evolves.

1.2.4 Magneto-dynamic results

Experimental work has also been performed more recently by various researchers. Many of these have been utilising the equivalence of the 2-D Euler equations and the equations of motion of highly magnetised plasma fields. This approach is used because of the difficulty in modelling patch vorticity and point vorticity combinations. The laboratory fluids are difficult to manipulate in the twin length scales required for point/patch combinations. The recent development of the Malmberg-Penning trap has enabled experiments involving background magnetic fields and trapped electrons. Hence these strongly magnetised electrons are a valuable tool to study patch and point vortex interactions.

The 1999 paper [20] examines the formation of vortex crystals. A vortex crystal is a lattice of intense, small diameter vortices which rotate rigidly in a lower vorticity background. The paper compares the process of formation of vortex crystals experimentally and numerically. Firstly, a vortex crystal is formed using a Penning-Malmberg trap. Two crystal types are formed by perturbations of an annular distribution of vorticity. The first is equivalent to the J.J. Thompson distribution, [32] of N point vortices in a ring. The second consists of a ring of N point vortices with a central vortex, as in the Morikawa and Swenson case [19]. Both of these are superposed over a patch of constant vorticity. This is then compared with a vortex-in-cell numerical simulation, which is a discretised numerical integration of the two dimensional Euler equations. In both cases, the vorticity when perturbed self-organises into these vortex crystals.

In their paper [23], Durkin and Fajans form a combination of patch vorticity and point vorticity using electrons in a Malmberg-Penning trap. In this experiment, an electron is placed in a magnetic field using the trap. When the electron, equivalent to a point vortex in two-dimensional Euler equations, is close enough to the patch edge, it entrains a region of irrotational flow. This occurs through a wave forming on the boundary of the patch. When this wave breaks, a region of irrotational flow is trapped, which in the frame of the patch is equivalent to a vortex of opposite polarity.

Also in this paper, they describe how N-vortices are placed in a ring within the background patch by a identical method. If placed near the perimeter, a similar entrainment of irrotational flow acts as a mechanism to move the electrons inwards, seemingly to form a stable solution of the Euler equations.

Jin and Dubin [24] consider an idealised model of the patch and point vortex interaction, within the context of the Malmberg-Penning trap. They confine their considerations to a nearly circular vortex, and to point vortices whose circulation, λ, is weak compared to the background vorticity. They show waves forming on the patch boundary break after a time of order $\lambda^{-1}\log(\lambda^{-1})$.

1.2.5 Exact solutions

Until recently, no exact solutions of the two-dimensional Euler equations have been known which possess these general features, although point vortex models have qualitatively similar properties (see [19]), but provide no information about the shape of vortex patches. Similarly, numerical patch vortex models of the structures also exist, but must be perturbed from different equilibria and then time-evolved, and hence are not exact. Previously, stability calculations pertaining to multipolar vortices modelled using vortex patches have therefore involved two stages. Firstly, an initial distribution of patches of constant vorticity, often a shielded monopole perturbed azimuthally at wavenumber–n, is numerically time evolved using the Euler equations with the aim of forming a multipolar structure. If such a structure is found, this is then perturbed in some systematic manner and also time evolved. In numerical simulations, the evolution is often tracked using Dritschel's technique of *contour surgery* [12], a form of contour dynamics [13] in which the vortex boundary is divide into multiply connected regions if the boundary begins to form loops connected to the main region by narrow bottlenecks. As a result of this, investigations of the properties of the structures have necessarily been carried out in a somewhat *ad-hoc* manner.

However, in [3], Crowdy presents a novel class of exact analytic solutions which satisfy the criteria (1)–(6). Crowdy demonstrates the efficacy of superposing line vortices on a patch of vorticity to form a model with all the characteristics of multipolar vortices. The resulting class of solutions captures the shape of the boundary and also models, through point vorticity, internal structure observed in experimental and meteorological data. These solutions utilise the *Schwarz function* to map from the unit circle to some region with a more complex boundary. The properties of this function allow the creation of exact solutions to the two-dimensional Euler equations, with merely a stationarity condition to be satisfied. The use of the Schwarz function to form exact solutions of the Euler equations is common through out this thesis. It is perhaps worth mentioning that while the Schwarz function has been utilised in other work, [13, 15], the paper [3] seems to be the first in which the geometric properties of the Schwarz function are utilised to create exact solutions of the Euler equations. These properties allow information to be gained about the boundary shape, while the equations of motion remain tractable, as the dynamics of point vortex to point vortex are governed by a finite system of O.D.E.s. In [3], Crowdy demonstrates how a one parameter family of solutions of the Euler equations consisting of regions of patch vorticity with superposed point vortices can be derived from a certain class of conformal maps. The Euler equations are shown to be automatically satisfied, and it is straightforward to show that continuity of pressure is satisfied, and similarly the boundary is a streamline. Provided the boundary is a simple closed curve the remaining condition is then to choose conformal map parameters such that the structure is stationary. This however turns out to be non-trivial, with many classes of maps not possessing stationary parameter regimes.

Systematic stability calculations are much facilitated by the exact nature of Crowdy's solutions. Hence in the investigation of linear stability, analytic expressions are available for all the entries in the final eigenvalue problem. The majority of these expressions reveal themselves as quite intractable integrals, but can be evaluated numerically. In the nonlinear case, contour dynamics software can be used to numerically evolve perturbations of the exact base state. As these base states are known exactly, a systematic approach is possible.

1.2.6 Vortical structures on the surface of a sphere

Work on vortex equilibria on the surface of the sphere is comparatively recent. The first consideration of such problems was by Bogomolov in 1977 [26], considering the motion of point vortices on a spherical surface. Kimano and Okamoto [36] later retrieved these equations and also the equations of motion for a patch of constant vorticity. In [28], Polvani and Dritschel extend Dritschel's contour surgery code to the surface of the sphere. This is then used to study roll-up of vorticity strips on a sphere, and also study interaction of patched of vorticity. DiBattista and Polvani [37] have constructed models combining point vortices and uniform vortex patches to study barotropic vortex pairs on a rotating sphere.

The 1977 paper [26] considers a thin layer of fluid on the the surface of a rotating sphere. This is the first time a spherical geometry was considered, as opposed to the planar β-plane approximation previously used in models of fluids on a rotating sphere. The layer is considered as being placed between two spherical shells. As the distance between the shells tends to zero, gravitational effects disappear, and the flow becomes two dimensional. By a process of replacing vortices in two dimensions with an infinite line of vortices in three dimensions, Bogomolov derives the stream function of a line vortex on the surface of a sphere, and shows an isolated vortex cannot exist, as the integral of vorticity over the surface of the sphere must be zero.

In the paper [27], Bogomolov considers the dynamics of point vortices on the sphere. The paper compares the behaviour of three point vortex exact solutions in the β-plane approximation and on the rotating sphere. They conclude that the cascade of energy to larger scales occurs more rapidly on the sphere than in the β-plane approximation, and that point vortex arrays tend to be more unstable on the sphere.

Dynamics of linear and nonlinear waves in patch vorticity on a sphere are considered in [28]. A zonal vorticity interface is taken on the surface of a sphere, with two-dimensional barotropic equations of motion. They find that non-linear waves are nonlinearly stable for large wave amplitudes. Finite area multi-vortex equilibria are investigated using contour dynamics techniques. Also considered in this paper is the equivalent of the Thompson n-vortex ring on the sphere. The barotropic model can provide a model of the polar vortex. The instability of the patches manifests itself through “pinch off” of regions of vorticity. Polvani and Dritschel find that, in general, vortex structures on the sphere are found to be less stable than those on the plane. It is hence to be assumed that the curvature of the sphere provides some mechanism for instability which is not present on the plane.

Approaches other than contour dynamics are possible to model the behaviour of vorticity on the sphere. A group theory approach is utilised in [29] towards point vortex equilibria. The paper [30] considers vortex motion on surfaces with constant curvature. After introducing the stereographic projection, the dynamics of vortex structures on both spherical and hyperbolic two-dimensional surfaces are considered.

1.3 Layout of thesis

In Chapter 2, we review the class of exact solutions to the two-dimensional Euler equations, presented by Crowdy in [3]. These possess the characteristics of atmospherically and experimentally observed multipolar vortex structures. Hence after this review, we examine their stability properties and compare those properties to those observed for other multipolar models. The shielded Rankine vortex is also considered, as it forms the simplest example of our paradigm of patch vortex and point vortex combinations. A methodology is presented for analysing the linear stability of structures defined by a conformal map from a simply connected region and its numerical implementation is discussed. Stability is also examined using the contour surgery methods of Dritschel.

Multipolar vortices have been observed atmospherically, and motivated by this, extension of the solutions of [3] to the surface of a sphere is presented in Chapter 3. Crucial to the method is the introduction of the stereographic projection, which allows the sphere to be projected onto the complex plane. This allows techniques of complex analysis, necessary for the methods of [3], to be utilised. Consideration of the form of point vorticity on the surface of the sphere will also reveal that on the sphere, a point vortex cannot exist in isolation, but must be surrounded by a region of patch vorticity. This retrospectively justifies the superposition of line vortices upon regions of constant vorticity. Using this methodology, it becomes clear that the same conformal map used on the plane can be used for the spherical solutions. However, due to curvature effects, different stationarity conditions apply, and hence different parameters values for the conformal map are obtained.

In Chapter 4, the linear stability of various vortical structures on the sphere are considered. These are a generalisation of the Morikawa and Swenson point vortex model, a generalisation of the shielded Rankine vortex and the stability of the multipolar vortices presented in Chapter 3. The results from the simpler point vortex and shielded Rankine vortex stability are calculated to provide checks for the stability of the full multipolar stability.

Finally, Chapter 5 presents a new class of planar solutions to the two-dimensional Euler equations. This consists of an periodic infinite band of patch vorticity with point vortices superposed.

CHAPTER 2

Linear stability of multipolar vortices

2.1 Two dimensional incompressible fluid flow

We present a brief review of two dimensional fluid flow on the unbounded plane. We restrict attention to flows with vorticity only in the form of isolated delta functions or regions of constant vorticity. We introduce the notation

$$\mathbf{u}(\mathbf{x}) = (u(\mathbf{x}), v(\mathbf{x})) \,, \tag{2.1}$$

where $\mathbf{x} = (x, y)$ is a point on the plane. The scalar value u represents the velocity of the fluid at the point $\mathbf{x}$ in the x-direction, while v represents the same in the y-direction. We define the vorticity at the point $\mathbf{x}$ as $\nabla \times \mathbf{u} = \omega$. The incompressible nature of the flow is enforced by $\nabla . \mathbf{u} = 0$. Where the flow is irrotational, $\nabla \times \mathbf{u} = 0$. These can equivalently be written as

$$u_x + v_y = \quad 0, \tag{2.2}$$

$$u_y - v_x = \quad 0, \tag{2.3}$$

which are the Cauchy-Riemann equations for a complex function $F(z) = u(z) - iv(z)$, where $z = x + iy$. If we define the complex potential $W(z)$ by

$$W(z) = \int^z F(z')dz' = \phi + i\psi, \tag{2.4}$$

where we call ϕ the scalar potential and ψ the streamfunction. Then given either ϕ or ψ, we can construct the velocity field by applying

$$\frac{\partial \psi}{\partial y} = u, \quad -\frac{\partial \psi}{\partial x} = v, \tag{2.5}$$

$$\frac{\partial \phi}{\partial x} = u, \quad \frac{\partial \phi}{\partial y} = v. \tag{2.6}$$

Examining (2.5), we see that in addition

$$\nabla^2 \psi = -\omega. \tag{2.7}$$

2.1.1 Point vorticity

Introduce a delta function into the vorticity expression,

$$\begin{aligned} \nabla \times \mathbf{u} &= \Gamma \delta(z - z_0) \qquad (2.8) \\ \nabla^2 \psi &= -\Gamma \delta(z - z_0). \qquad (2.9) \end{aligned}$$

We say this defines a point vortex with circulation Γ at the point $z = z_0$. Using Green's function for the unbounded plane, we see that

$$\psi = \frac{-\Gamma}{2\pi} \log |z - z_0|. \tag{2.10}$$

As

$$\psi = \mathbf{Im}(W(z)) = \frac{W(z) - \overline{W(z)}}{2i}, \tag{2.11}$$

then $u - iv = 2i\psi_z$. Then

$$u - iv = -i\frac{\Gamma}{2\pi}\frac{1}{z - z_0}. \tag{2.12}$$

Expanding a general velocity field near a line vortex at $z = z_0$ will result in a Laurent series expansion of form

$$u - iv = -i\frac{\Gamma}{2\pi}\frac{1}{z - z_0} + G(z), \tag{2.13}$$

where $G(z)$ is some function analytic near $z = z_0$. The line vortex itself is advected by the part of the flow which is locally analytic,

$$u(z_0) - iv(z_0) = G(z_0). \tag{2.14}$$

This is referred to as the *non-self-induction* condition, as the removed non-analytic part is induced by the line vortex.

2.1.2 Regions of constant vorticity

Suppose that in some simply connected region D, there is a constant vorticity ω_0, and outside this area the flow is irrotational. Then

$$\nabla^2\psi = \begin{cases} -\omega_0, & z \in D \\ 0, & z \notin D, \end{cases} \tag{2.15}$$

or

$$4\frac{\partial^2\psi}{\partial z\partial\bar{z}} = \begin{cases} -\omega_0, & z \in D \\ 0, & z \notin D. \end{cases} \tag{2.16}$$

Then integrating, we have

$$\psi_z = \begin{cases} -\frac{\omega_0}{4}\bar{z} - \frac{\omega_0}{4}F(z), & z \in D \\ \\ -\frac{\omega_0}{4}G(z), & z \notin D, \end{cases} \tag{2.17}$$

where $F(z)$ is a function analytic inside D, $G(z)$ is a function analytic outside D, both introduced by integration. These functions are determined by the shape of the boundary ∂D. By requiring that the boundary is a material surface and that the velocity is continuous across the boundary, we enforce continuity of pressure. To see this, consider pairs of points A,C and B,D adjacent across the boundary,

$$\begin{aligned} \frac{D}{Dt}\int_A^B \mathbf{u}.d\mathbf{l} &= \int_A^B \left(\frac{D\mathbf{u}}{Dt}.d\mathbf{l} + \mathbf{u}\frac{D}{Dt}(\delta\mathbf{l})\right) \\ &= \int_A^B \left(-\frac{1}{\rho}\nabla p + \nabla(\frac{\mathbf{u}^2}{2})\right).\mathrm{dl}. \end{aligned} \tag{2.18}$$

Making the assumption that the fluid is barotropic, $p = p(\rho)$. Then $-\frac{1}{\rho}\nabla p = \nabla h(\rho)$, for some $h(\rho)$. Then

$$\frac{D}{Dt}\int_A^B \mathbf{u}.\mathrm{d}\mathbf{l} = \left(-h(\rho) + \frac{1}{2}\mathbf{u}^2\right)\Big|_A^B. \tag{2.19}$$

This applies also to the integral from C to D, as the surface is material, and velocity continuous. Therefore

$$\frac{D}{Dt}\int_A^B \mathbf{u}.\mathrm{d}\mathbf{l} = \frac{D}{Dt}\int_C^D \mathbf{u}.\mathrm{d}\mathbf{l}, \tag{2.20}$$

and

$$(-h(\rho) + \frac{1}{2}\mathbf{u}^2)\Big|_A^B = (-h(\rho) + \frac{1}{2}\mathbf{u}^2)\Big|_C^D, \tag{2.21}$$

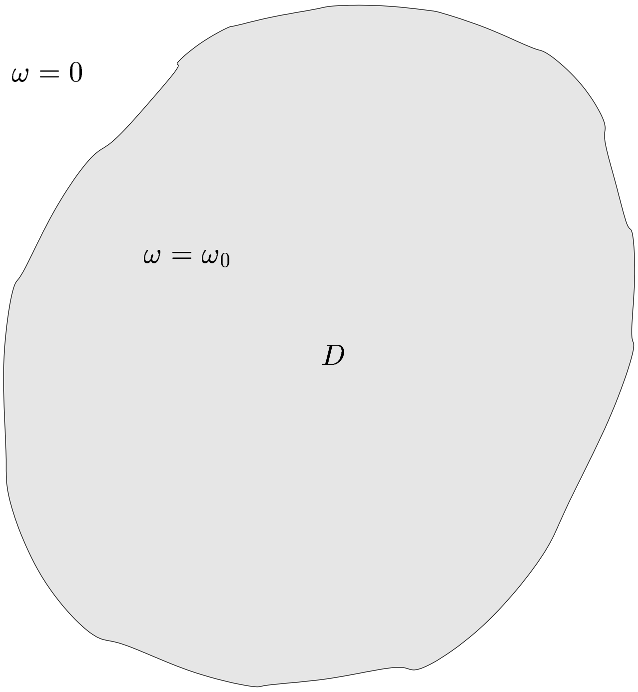

Fig. 2.1: Diagram of a patch of constant vorticity

which implies

$$(-h(\rho) + \frac{1}{2}\mathbf{u}^2)\Big|_D^B = (-h(\rho) + \frac{1}{2}\mathbf{u}^2)\Big|_C^A. \tag{2.22}$$

Applying continuity of velocity, then

$$-h(\rho)\Big|_D^B = -h(\rho)\Big|_C^A, \tag{2.23}$$

which implies

$$p(\rho)\Big|_D^B = p(\rho)\Big|_C^A. \tag{2.24}$$

Hence if the pressure is continuous anywhere on the surface, it is continuous everywhere.

Hence enforcing that the velocity is continuous and the patch boundary is a material surface enforces continuity of pressure, for incompressible or barotropic flows.

2.2 Mathematical formulation of exact solutions

2.2.1 Shielded Rankine vortex

Consider the vorticity distribution, commonly known as the Rankine vortex, given by

$$u_\theta = \begin{cases} \dfrac{\omega_0 r}{2}, & r < r_0 \\ \\ \dfrac{\omega_0 r_0^2}{2r}, & r > r_0 \end{cases} \tag{2.25}$$

Consider then the two contour Rankine vortex, taken to be the vortex distribution consisting of a Rankine vortex of vorticity ω_I surrounded by an annular region of vorticity ω_O. Note that this is the initial vorticity distribution for many of the numerical and experimental models for multipolar vortices.

If the limit as $r_o \to 0$ and $\omega_I \to \infty$ is then taken in such a way that the total circulation remains finite, an important precursor to the class of solutions presented in [3] is obtained. This is named the *shielded Rankine vortex* or *shielded point vortex.* This is equivalent to adding a line vortex at the origin of the Rankine vortex (2.25). The velocity field is then

$$u_\theta = \begin{cases} \dfrac{\omega_0 r}{2} - \dfrac{\omega_0 r_0^2}{2r} & r < r_0 \\ 0 & r > r_0 \end{cases} . \tag{2.26}$$

The shielded Rankine vortex consists of a patch of constant vorticity, with a a line vortex superposed at the origin. The patch is surrounded by quiescent fluid. Dynamically, we require that the velocity is continuous at the patch boundary, which is well known to imply continuity of pressure for vortex patches [13], while kinematically the boundary must be a streamline, which is clearly true. For this to be a steady solution of the Euler equations, the line vortex must be stationary under the *non-self-induction hypothesis*, and this is trivially satisfied here. Hence (2.26) is a steady solution of the two dimensional Euler equations.

2.2.2 The Schwarz function

Definition 2.2.1 *The Schwarz function*

> Given a domain $D \in \mathbf{C}$ with boundary ∂D, a closed curve, then the *Schwarz function*, $S(z)$, is the unique, locally analytic complex function such that
>
> $$S(z) = \bar{z}, \qquad \forall z \in \partial D.$$

The stream function associated with (2.26) can now be written inside $r = r_0$ as

$$\psi(x,y) = \frac{\omega_0}{4} z\bar{z} - \frac{\omega_0}{2}\mathbf{Re}\left[\int_z S(z')dz'\right], \tag{2.27}$$

where $z = x + iy$ and $S(z)$ is the Schwarz function of the domain $D = \{z | z\bar{z} < {r_0}^2\}$. Using def. (2.2.1), it is apparent that for this geometry,

$$S(z) = \frac{r_0^2}{z}. \tag{2.28}$$

Then integrating $S(z)$,

$$\int_z S(z')dz' = r_0^2 \log z, \tag{2.29}$$

and (2.27) consists of a patch of vorticity with superposed point vortex of strength $\kappa = \pi\omega_0 r_0^2$, at $z = 0$. Note that the Schwarz function is not only equal to $\bar{z}$ on ∂D but, with this domain, is also in the form of a point vortex. This behaviour will be crucial for the creation of the multipolar equilibria.

2.3 Multipolar solutions

Consider the streamfunction

$$\psi(x,y) = \begin{cases} \dfrac{\omega_0 z\bar{z}}{4} - \dfrac{\omega_0}{4}\left(\displaystyle\int^z S(z')\,dz' + \int^{\bar{z}} \bar{S}(z')\,dz'\right) & z \in D \\ 0 & z \notin D. \end{cases} \tag{2.30}$$

In the case where $D = \{z | z\bar{z} \leq 1\}$, this is identical to the streamfunction (2.27). Suppose, however, that instead of taking D to be a circular disc, a general domain is taken. We still require a valid solution to the Euler equations however, so the kinematic and dynamic boundary conditions hold still be satisfies. Examining the total derivative on ∂D and using (2.30),

$$\begin{aligned} d\psi = & \ \psi_z dz + \psi_{\bar{z}} d\bar{z} \\ = & \ \frac{\omega_0}{4}(\bar{z} - S(z)))dz + \frac{\omega_0}{4}(z - \bar{S}(\bar{z}))d\bar{z} \\ = & \ 0, \end{aligned} \tag{2.31}$$

by the definition of the Schwarz function, and hence the patch boundary is a streamline, satisfying the kinematic boundary condition.

The fluid velocity is given by $u - iv = 2i\psi_z$, and is clearly continuous across ∂D, and equal to 0 there. Therefore, before specifying a domain, this streamfunction satisfies the dynamic and kinematic boundary conditions on ∂D. It was shown in §2.2.2 that the Schwarz function of the map from the ζ-circle with radius r_0^2 has a point vortex at the origin. It is desirable that we map from domains which will produce Schwarz functions analytic inside D, except perhaps for simple poles with real residue. This will correspond to the presence of line vortices within the patch of constant vorticity. Assume a mapping from the interior of the unit circle in the ζ-plane to the inside of a domain D in the z-plane. It can be shown (see [38]) that if the Schwarz function is meromorphic within D, then the conformal map $z(\zeta)$ is necessarily a rational function of ζ. Hence consideration is given only to these conformal maps. The Riemann mapping theorem guarantees that we may enforce that $z(0) = 0$ [35].

For a steady solution, it is then necessary to impose the condition that each line vortex be steady under the non-self-induction hypothesis. After choosing a conformal map, it then remains to pick any parameters in the conformal map to enforce stationarity of the line vortices. Note that this *may not in general be possible*, and hence the choice of conformal map is a crucial part of this method of creating solutions.

2.3.1 Conformal Map

The conformal map presented in [3] is

$$z(\zeta) = R(a;n)\zeta\left(1 + \frac{b(a;n)}{\zeta^n - a^n}\right), \qquad a, b, R \in \mathbf{R}, \quad |a| > 1 \ . \tag{2.32}$$

Take the domain $D = \{z(\zeta) | \zeta\bar{\zeta} \leq 1\}$, with associated Schwarz function

$$S(z(\zeta)) = \frac{R}{\zeta}\left(1 + \frac{\zeta^n b}{1 - a^n \zeta^n}\right). \tag{2.33}$$

This is singular at $\zeta = 0$ and $\zeta = e^{(2\pi i k/n)}/a$, where $k = 1, \ldots, n$. These correspond to line vortices in the velocity field. As $z(\zeta)$ is non-trivial function of ζ, the inverse $\zeta(z)$ is unknown, hence $S(z(\zeta))$ is written in terms of ζ. It is shown in [3] that satisfying the stationarity condition for the satellite line vortices provides non-linear equations for $R(a; n)$ and $b(a; n)$, where the a parameterises the solutions space for given n. We specify that the line vortices lie on the $z\bar{z} = 1$ circle in the z-plane. Hence the equations given in [3] become:

$$\frac{1}{b}\left(1 + \frac{ba^n}{(1 - a^{2n})}\right) - a + \frac{b(n-1)}{2na^{n-1}} + \frac{b}{2na^n}\frac{z_{\zeta\zeta}(a^{-1})}{z_\zeta(a^{-1})} = 0, \tag{2.34}$$

which can be solved as a quadratic for b, and

$$R = \frac{a^{2n+1} - a}{1 - a^{2n} + ba^n}. \tag{2.35}$$

The strength of these line vortices is then given by

$$\begin{aligned} \Gamma_0 = & \quad \omega\pi R z_\zeta(0) & (2.36) \\ \Gamma_s = & \quad -\tfrac{\omega\pi R b z_\zeta(a_{-1})}{na^n} & (2.37) \end{aligned}$$

2.3.2 Solutions

As $b(a; n)$ and $R(a; n)$ are now known, the Schwarz function type solutions specified by (2.32) can be examined. A typical quadrupolar ($n = 3$) vortex structure is shown in Fig. (2.2). Note how it possesses the characteristics (1) - (6) used to define a multipolar vortex in §1.1. The vortex structures produced by this map for all n satisfy the qualitative features of multipolar vortices, as described in Section 1.1. The presence of line vortices provide some inner structure to the distribution, and the placing of the line vortices are analogous to the distribution of vorticity mentioned in (2) of our definition of multipolar vortices. Some general features of the solutions can be detailed. For large values of the parameter a, the patch becomes approximately circular, and the $n + 1$ point vortices are close together.

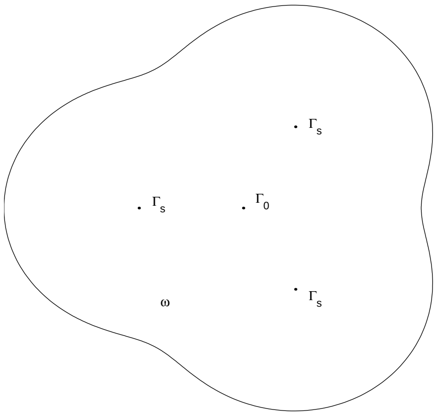

Fig. 2.2: Schematic of a quadrupolar vortex consisting of a uniform patch of vorticity ω with four superposed line vortices – a central line vortex of strength Γ_0 and 3 satellite line vortices each of strength Γ_s.

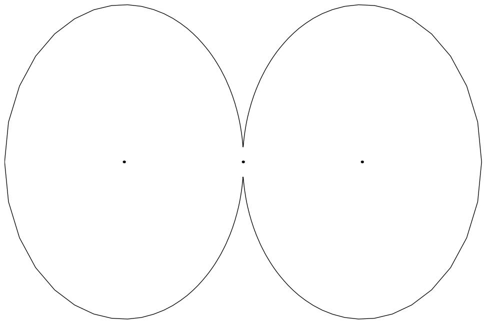

Fig. 2.3: Patch boundary for $N = 2$ and $a = 1.05$. Line vortices are shown as bold dots.

As $a \to 1$, the patch boundary becomes more distorted and the line vortices move further apart. For some value a_{crit}, the patch boundary becomes cusped (see Fig. 2.4) and a values below this are inadmissible, as the patch boundary crosses itself. Figure 2.3 shows a tripole ($n = 2$), which is close to cusped - note how the patch of vorticity approaches two touching circles, with a point vortex at the point where there would be an intersection.

The value a_{asymp} is the value at which the strength of the central line vortex is zero. For values of $a > a_{asymp}$, Γ_s and Γ_0 are opposite signs, Γ_s being of the opposite sign from the patch vorticity. This is in common with condition (2) of our definition of

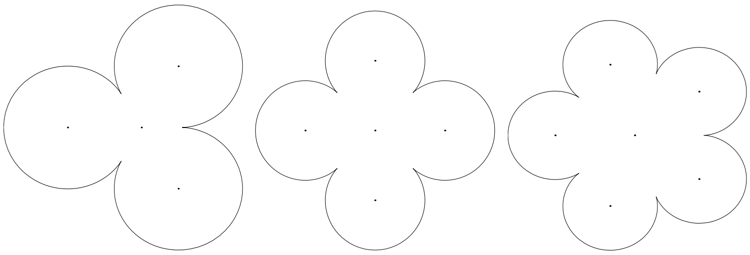

Fig. 2.4: Vortex patch shapes for a close to $a_{crit}^{(N)}$: $N = 3$, $a_{crit}^{(3)} = 1.211$; $N = 4$, $a_{crit}^{(4)} = 1.241$; $N = 5$, $a_{crit}^{(5)} = 1.232$. These are close to the limiting states in the sense of Overman [16] and exhibit near-cusp singularities in the patch boundary. Line vortices are shown as bold dots.

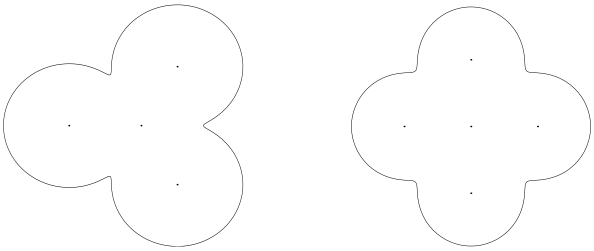

Fig. 2.5: Vortex patch shapes for a close to $a_{asymp}^{(N)}$: $N = 3$, $a = 1.385$; $N = 4$, $a = 1.485$ (cf. Figure 8 of [3]). Line vortices are shown as bold dots.

a multipolar vortex from §1.1. However, for $a < a_{asymp}$, Γ_s and Γ_c have the same sign, both opposite to the patch vorticity. This is contrary to condition (2) of §1.1. Fig. 2.5 shows solutions near a_{asymp}. Figs. 2.6 and 2.8 show b against a for $n = 3$ and $n = 4$ respectively. The asymptotes and cusp values can be seen. Figs. 2.7 and 2.9 show the ratio of the central point vortex circulation to the patch circulation and satellite point vortices to the the patch circulation for $n = 3$ and $n = 4$.

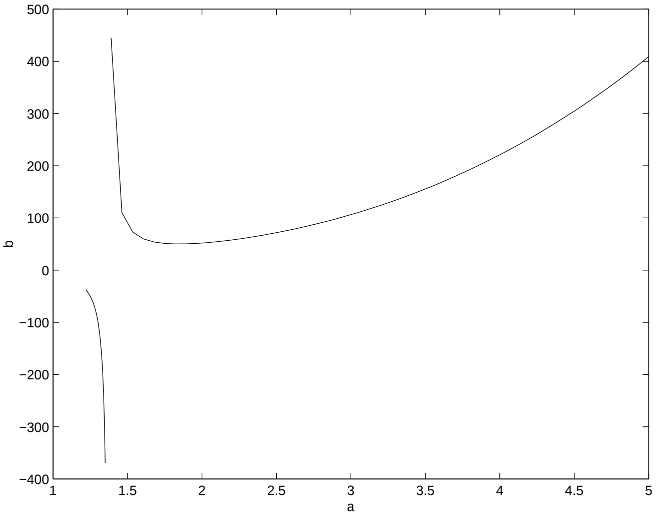

Fig. 2.6: b against a for $N = 3$: $a^{(3)}_{crit} = 1.211; a^{(3)}_{asymp} = 1.371$.

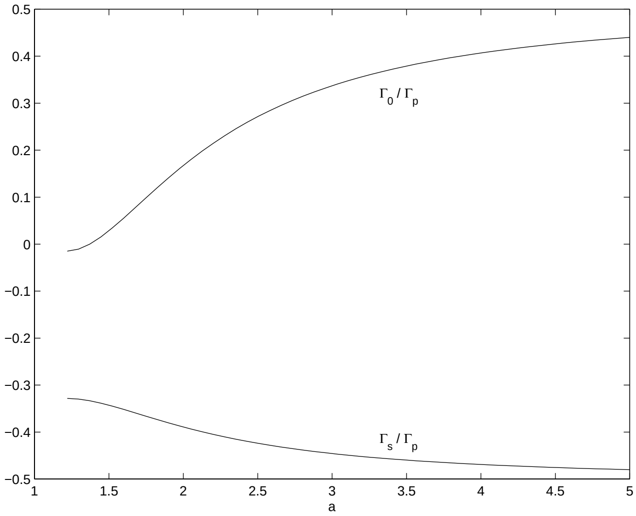

Fig. 2.7: Graph of $\frac{\Gamma_0}{\Gamma_p}$ and $\frac{\Gamma_s}{\Gamma_p}$ against a for $N = 3$.

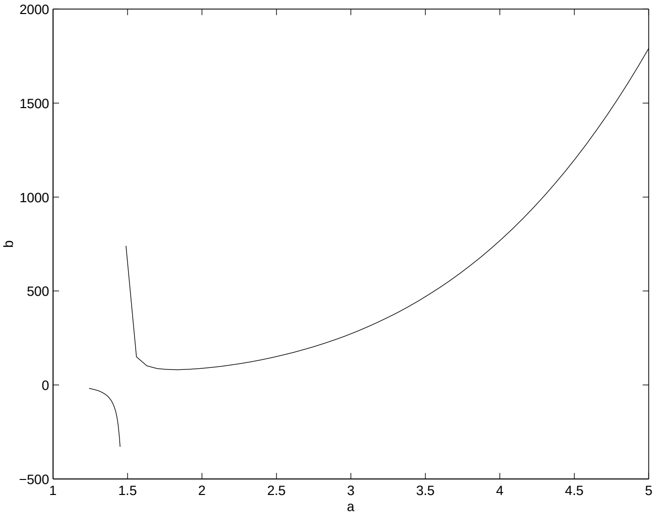

Fig. 2.8: b against a for $N = 4$: $a^{(4)}_{crit} = 1.241; a^{(4)}_{asymp} = 1.477$.

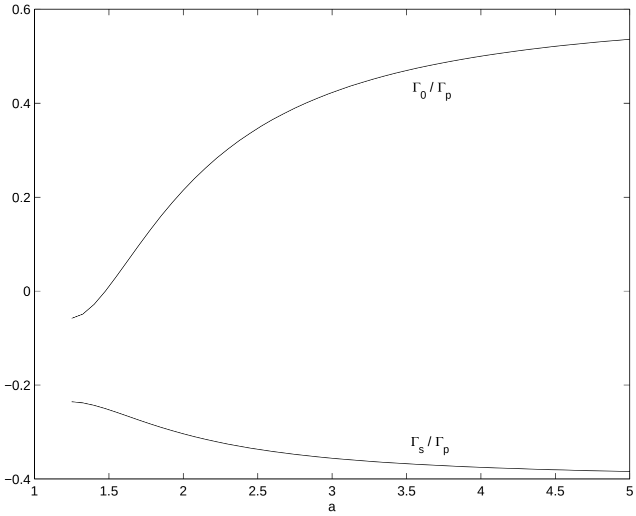

Fig. 2.9: Graph of $\frac{\Gamma_0}{\Gamma_p}$ and $\frac{\Gamma_s}{\Gamma_p}$ against a for $N = 4$.

2.4 Stability analysis of planar multipoles

We now examine the stability of the planar multipolar solutions. Firstly we consider the stability of a distribution consisting of a circular patch of constant vorticity, with a superposed line vortex at the origin, and some flow outside. The case where the flow outside is quiescent corresponds to the shielded Rankine vortex (2.26). Stability of this case is tractable analytically, and will provide a check of the numerical results of the full multipolar solutions. This analysis will then be generalised to the full multipolar solutions.

2.4.1 Shielded Rankine Vortex

Consider the case of a circular patch with constant vorticity ω_0, and a superposed line vortex at the origin of circulation Γ, with some irrotational flow outside. Then

$$u_\theta = \begin{cases} \dfrac{\omega_0 r}{2} - \dfrac{\Gamma\omega_0}{2\pi r}, & r < 1 \\ \\ \omega_0 \dfrac{2}{r}\left(1 - \dfrac{\Gamma}{4\pi}\right), & r > 1. \end{cases} \tag{2.38}$$

Without loss of generality, we may set $\omega_0 = 1$. Then the velocity field is given by

$$u - iv = \begin{cases} 2i\bar{z} - \dfrac{i\Gamma}{2\pi z}, & z \in D \\ \\ \dfrac{2i}{z}\left(1 - \dfrac{\Gamma}{4\pi}\right), & z \notin D, \end{cases} \tag{2.39}$$

where the unperturbed conformal map is taken to be

$$z_0(\zeta) = \zeta, \tag{2.40}$$

in the domain

$$D = \{z(\zeta); |\zeta| < 1\}. \tag{2.41}$$

The conformal map must now be perturbed. In general, we wish to find the values of σ in the perturbed conformal map which are valid solutions of the Euler equations. Equation (2.41) requires that this perturbation also perturb the patch boundary and position of the central line vortex. The Helmholtz laws require that the vorticity of any fluid element must be conserved; hence the area of the vorticity patch must also be constant, and the strength of any line vortex must be constant. The perturbed expression for $u - iv$ thus becomes

$$u - iv = \begin{cases} 2i\bar{z} - \dfrac{i\Gamma}{2\pi(z - \epsilon z_c(t))} + 2iF(z,t), & z \in D(t) \\ \\ 2iG(z,t) + \dfrac{2i}{z - \epsilon z_c}\left(1 - \dfrac{\Gamma}{4\pi}\right), & z \notin D(t), \end{cases} \tag{2.42}$$

where z_c denotes the position of the line vortex, $F(z,t)$ is some function analytic within $D(t)$, and $G(z,t)$ some function analytic outside $D(t)$. $F(z,t)$ and $G(z,t)$ therefore represent the irrotational correction to the velocity field caused by the perturbation to the conformal map.

2.4.2 Riemann-Hilbert problem

Applying continuity of velocity on the patch boundary, it is required that

$$\bar{z} - \frac{1}{(z - \epsilon z_c(t))} = G(z,t) - F(z,t), \quad z \in \partial D \ . \tag{2.43}$$

As $G(z,t)$ is analytic outside $D(t)$ and $F(z,t)$ inside $D(t)$, and $G(z,t) - F(z,t) = P(z,t)$, this is in the form of a Riemann-Hilbert problem (see [14] for details). Hence it admits a Plemelj solution, so

$$F(z,t) = \frac{1}{2\pi i}\oint \frac{P(Z,t)}{z - Z} dZ, \quad z \in D \tag{2.44}$$

and

$$G(z,t) = \frac{1}{2\pi i}\oint \frac{P(Z,t)}{z - Z} dZ, \quad z \notin D \tag{2.45}$$

However, it will be shown that in this case, as the conformal map from the ζ-plane to the z-plane is trivial, the function $P(z,t)$ can be split by inspection into parts analytic inside and outside the patch.

The perturbed conformal map is now taken to have form $z(\zeta) = z_0(\zeta) + \hat{z}(\zeta,t) = \zeta + \epsilon \sum_{n=1}^{\infty} \zeta^n \hat{a}_n$, where $\hat{a}_n = e^{\sigma_n t}$. The perturbed point vortex position will be taken to be $\hat{z}_c = \epsilon\hat{\zeta}_c$. We assume the perturbation is infinitesimal, i.e. $\epsilon \ll 1$, and terms of order ϵ^2 and higher will be vanishingly small. However, due to the high degree of symmetry in the shielded Rankine vortex, the ansatz

$$z(\zeta) = \zeta + \epsilon \hat{a}_n \zeta^n, \quad n \in \mathcal{N} \tag{2.46}$$

is taken, which effectively implies the modes of perturbation decouple. $\hat{a}_0$ can legitimately be set to 0 as this corresponds to setting $\hat{z}(0) = 0$, which is allowed under the Riemann mapping theorem (see [35]). Similarly, it is also required that for small ζ, $\arg(z(\zeta)) = 0$, which sets the condition on $\hat{a}_1$, $\hat{\hat{a}}_1 = \hat{a}_1$.

For $z \in \partial D$, $\zeta\bar{\zeta} = 1$, hence $\bar{\zeta} = 1/\zeta$. Substituting into (2.46), it can be seen that

$$\bar{z}(1/\zeta) = \frac{1}{\zeta} + \epsilon \frac{\hat{\hat{a}}_n}{\zeta^n}, \tag{2.47}$$

and

$$\frac{1}{\zeta} = \frac{1}{z(1/\zeta)}(1 + \epsilon \zeta^{n-1} \hat{a}_n). \tag{2.48}$$

Substituting (2.46) into (2.48), we obtain

$$\frac{1}{\zeta} = \frac{1}{z(1/\zeta)}(1 + \epsilon z(\zeta)^{n-1} \hat{a}_n) + O(\epsilon^2) \tag{2.49}$$

and hence

$$\bar{z}(1/\zeta) = \frac{1}{z(1/\zeta)}(1 + \epsilon z(\zeta)^{n-1} a_n) + \frac{\epsilon \hat{\hat{a}}_n}{z(\zeta)^n} + O(\epsilon^2) \tag{2.50}$$

$$\Rightarrow \bar{z}(1/\zeta) - \frac{i\Gamma}{2\pi(z(\zeta) - \hat{z}_c(t))} = \frac{1}{z(\zeta)}(1 + \epsilon \hat{a}_n z(\zeta)^{n-1}) + \frac{\epsilon \hat{\hat{a}}_n}{z(\zeta)^n} - \frac{i\Gamma}{2\pi(z(\zeta) - \hat{z}_c(t))}. \tag{2.51}$$

Clearly, (2.51) can be divided into parts analytic inside and outside ∂D, so it is apparent that

$$G(z,t) = \frac{1}{z(\zeta)} + \frac{\epsilon \hat{\hat{a}}_n}{z^n} - \frac{2i}{(z(\zeta) - \hat{z}_c(t))}, \tag{2.52}$$

and

$$F(z,t) = -\epsilon \hat{a}_n z(\zeta)^{n-2}. \tag{2.53}$$

2.4.3 Kinematic Boundary Condition

The boundary of the patch of vorticity is a material surface (see [13]), and as such, must move with the local velocity field. This is enforced by the kinematic boundary condition, that

$$\mathrm{Im}[z_t \bar{z}_s] = \mathrm{Im}[(u + iv)\bar{z}_s]. \tag{2.54}$$

As

$$z_s = \frac{i\zeta z_\zeta}{|z_\zeta|}\ , \qquad z \in \partial D, \tag{2.55}$$

this can be rearranged to give

$$\mathrm{Re}\left[\frac{z_t(\zeta)\bar{z}_\zeta(\zeta^{-1})}{\zeta}\right] = \mathrm{Re}\left[\frac{(u+iv)\bar{z}_\zeta(\zeta^{-1})}{\zeta}\right]. \tag{2.56}$$

Written out in full, (2.56) becomes

$$\frac{z_t(\zeta)\bar{z}_\zeta(\zeta^{-1})}{\zeta} + \bar{z}_t(\zeta^{-1})\zeta z_\zeta(\zeta) = \frac{(u+iv)\bar{z}_\zeta(\zeta^{-1})}{\zeta} + (u-iv)\zeta z_\zeta(\zeta). \tag{2.57}$$

$u - iv$ is determined from equation (2.42), with $F(\zeta)$ given by equation (2.53).

Then expanding $u - iv$ to order ϵ, it can be seen that

$$u - iv = 2i(\frac{1}{\zeta} + \epsilon\hat{\hat{a}}_n\frac{1}{\zeta^{n-2}}) - \frac{i\Gamma}{2\pi}(\frac{1}{\zeta} + \frac{\epsilon\hat{\hat{z}}_c}{\zeta^2} - \epsilon\hat{a}_n\zeta^{n-2}) - 2i\epsilon\hat{a}_n\zeta^{n-2} + \mathcal{O}(\epsilon^2). \tag{2.58}$$

Then, considering only terms which arise from $(u-iv)\zeta z_\zeta(\zeta)$ on the right hand side,

$$\begin{aligned}(u-iv)\zeta z_\zeta(\zeta) = \quad & 2i(1 + \frac{\epsilon\hat{\hat{a}}_n}{\zeta^{n-1}}) - \frac{i\Gamma}{2\pi}(1 + \frac{\hat{\hat{z}}_c}{\zeta} - \epsilon\hat{a}_n\zeta^{n-1}) \\ & -2i\epsilon\hat{a}_n\zeta^{n-1} + 2i\epsilon n\hat{a}_n\zeta^{n-1} - \frac{i\Gamma}{2\pi}\epsilon n\hat{a}_n\zeta^{n-1},\end{aligned} \tag{2.59}$$

with $(u+iv)\bar{z}_\zeta(\zeta^{-1})/\zeta$ the complex conjugate of this.

Considering only positive powers of ζ on both sides of the kinematic condition (negative powers consist are given by the complex conjugate),

$$\begin{aligned}\epsilon\sigma_n\hat{a}_n\zeta^{n-1} = \quad & -2i\epsilon\hat{a}_n\zeta^{n-1} + \frac{i\Gamma}{2\pi}\hat{\hat{z}}_c\zeta + \frac{i\Gamma}{2\pi}\epsilon\hat{a}_n\zeta^{n-1} \\ & -2i\epsilon\hat{a}_n\zeta^{n-1} + 2i\epsilon n\hat{a}_n\zeta^{n-1} - \frac{i\epsilon\Gamma}{2\pi}n\hat{a}_n\zeta^{n-1}.\end{aligned} \tag{2.60}$$

Equating powers of ζ, the perturbations must satisfy

$$\sigma_n\hat{a}_n = \begin{cases} \dfrac{-i\Gamma}{2\pi}\hat{a}_2 + \dfrac{i\Gamma}{2\pi}\hat{\hat{z}}_c, & n = 2 \\ 2i\hat{a}_n((n-2) + \dfrac{\Gamma}{4\pi}(1-n)), & n > 2. \end{cases} \tag{2.61}$$

2.4.4 Line Vortex

The central line vortex must also move with the non-self-induced local velocity. Hence

$$\begin{aligned}\frac{d\bar{z}_c}{dt} &= 2i\bar{z} + 2iF(z,t)|_{z=\hat{z}_c} \\ &= 2i\hat{\bar{z}}_c - 2ia_n\hat{z}_c^{n-2} \\ &= 2i\epsilon\hat{\zeta}_c - 2ia_n(\epsilon\hat{\zeta}_c)^{n-2}.\end{aligned} \tag{2.62}$$

This gives us

$$\sigma_n\hat{\bar{\zeta}}_c = \begin{cases} 2i\hat{\bar{\zeta}}_c - 2i\hat{a}_2, & n = 2 \\ 2i\hat{\bar{\zeta}}_c, & n > 2. \end{cases} \tag{2.63}$$

Note that both equation (2.63) and equation (2.61) decouple for $n > 2$, so only in the elliptic modes (i.e. $n = 2$) is there interaction between the boundary and the line vortex motions.

2.4.5 Eigenvalue problem

An eigenvalue problem can now be formed,

$$\sigma\mathbf{x} = A\mathbf{x} \tag{2.64}$$

where

$$\mathbf{x} = \begin{pmatrix} a_n \\ \bar{\zeta}_c \end{pmatrix}, \tag{2.65}$$

and

$$A = \begin{cases} \begin{pmatrix} -\frac{i\Gamma}{2\pi} & \frac{i\Gamma}{2\pi} \\ -2i & 2i \end{pmatrix}, & n = 2 \\ \\ \begin{pmatrix} 2i((n-2) + \frac{\Gamma}{4\pi}(1-n)) & 0 \\ 0 & 2i \end{pmatrix}, & n > 2. \end{cases} \tag{2.66}$$

Solving this gives

$$\sigma = \begin{cases} \{0, 2i(1 - \frac{\Gamma}{4\pi})\}, & n = 2 \\ \{2i((n-2) + \frac{\Gamma}{4\pi}(1-n)), 2i\}, & n > 2. \end{cases} \tag{2.67}$$

The following observations can be made:

1. The eigenvalues have zero real part, and thus the structure is *neutrally stable.*
2. The eigenmode $a_1\zeta$ has a zero eigenvalue, which corresponds to area changing perturbations (which are inadmissible in this formulation).
3. When $\Gamma = 0$, the central line vortex is not present, and the eigenvalue $2i(n-2)$ is recovered. This eigenvalue corresponds to the value obtained by considering the Rankine vortex [13]. In this case, the zero ($n = 2$) eigenvalue in (2.67) corresponds to steady bifurcation to the *Kirchoff elliptical vortex patch.*
4. When $\Gamma = 4\pi$, the total circulation of the vortex is zero, and the fluid outside is quiescent. In this case, the $n = 2$ eigenvalues are both zero, and for $n > 2$, repeated eigenvalues of $\pm 2i$ are obtained.

Note that in the $\Gamma = 4\pi$ case, the representation from (2.30) can be used to express the streamfunction as

$$\psi(x,y) = \begin{cases} \dfrac{\omega_0 z\bar{z}}{4} - \dfrac{\omega_0}{4}\left(\displaystyle\int^z S(z')\,dz' - \int^{\bar{z}} \bar{S}(z')\,dz'\right) & z \in D \\ 0 & z \notin D. \end{cases} \tag{2.68}$$

where $D = \{z(\zeta); |\zeta| < 1\}$ and $z = \zeta + \sum_{n=1}^{\infty} \zeta^n a_n$. In this case, the Schwarz function is

$$-2iS(z) = -\frac{i\Gamma}{2\pi(z - z_c)}. \tag{2.69}$$

The velocity field is then given by

$$u - iv = 2i\psi_z = \begin{cases} 2i\bar{z} - 2iS(z), & z \in D \\ 0, & z \notin D. \end{cases} \tag{2.70}$$

2.5 Linear stability of multipolar exact solutions

We now generalise the methods applied to the shielded Rankine vortex to the full multipolar solutions.

Taking the conformal map for the planar multipolar solutions from §2.3

$$z(\zeta) = R\zeta\left(1 + \frac{b}{\zeta^N - a^N}\right), \tag{2.71}$$

the following streamfunction is formed:

$$\psi(x,y) = \begin{cases} \dfrac{\omega_0 z\bar{z}}{4} - \dfrac{\omega_0}{4}\left(\displaystyle\int^{z} S(z')\,dz' - \int^{\bar{z}} \bar{S}(z')\,dz'\right), & z \in D \\ 0, & z \notin D. \end{cases} \tag{2.72}$$

D is taken as the domain $\{z(\zeta); |\zeta| < 1\}$. The velocity field is given by

$$\begin{aligned} u - iv = \;& 2i\psi_\zeta \\ = \;& \begin{cases} \dfrac{i\omega_0 \bar{z}}{2} - \dfrac{i\omega_0}{2} S(z), & z \in D \\ 0, & z \notin D \end{cases} \end{aligned} \tag{2.73}$$

2.5.1 The Schwarz function in the z-plane

Note that while the Schwarz function $S(z)$ is known explicitly in the ζ–plane, it is *not* in general known in the z–plane. However, $S(z)$ can always be written as

$$S(z) = H_{in}(z) + H_{out}(z), \tag{2.74}$$

where H_{in} is analytic within the patch, and H_{out} is analytic outside the patch. In fact, for the general n-th order exact solution, the Schwarz function can be divided into parts of form $\Gamma_j/(z - z_j)$ where z_j is the position of a line vortex, and some function $F(z)$, which is analytic within the patch. Hence,

$$-2iS(z) = -\sum_j \left\{ \frac{i\Gamma_j}{2\pi(z - z_j)} \right\} + 2iF(z), \tag{2.75}$$

where Γ_j is the strength of the line vortex z_j, which is fixed by the stationarity condition.

2.5.2 General Method

The method of §2.4.1 must now be extended to the multipolar case. The steps which must be performed are as follows:

1. $u - iv$ must be rewritten as
$$u - iv = \begin{cases} \dfrac{i\omega_0}{2}\left(\bar{z} - \sum \dfrac{\kappa_j}{z - z_j} - F(z)\right), & z \in D \\ 0, & z \notin D \end{cases} \tag{2.76}$$
where z_j and κ_j represent the position and strength of the j line vortices. The term $S(z)$ in (2.73) contains the line vortices, plus some irrotational flow. Hence we split the Schwarz function into line vortex terms and some unknown analytic function, $F(z)$.

2. Introduce a time dependent perturbation to the conformal map $z(\zeta)$, so that $z(\zeta) = z_0(\zeta) + \epsilon\hat{z}(\zeta, t)$, where $z_0(\zeta)$ is the base state conformal map, and $\hat{z}(\zeta, t)$ is the perturbation to the conformal map. Consequently the line vortex positions are perturbed to $z_j = z_{j0} + \epsilon\hat{z}_j(t)$, where z_{k0} is the unperturbed line vortex position, and $\hat{z}_j(t)$ is the perturbation to the line vortex position. $\hat{\zeta}_k$ will denote the pre-image of this perturbation in the ζ-plane. Note that the perturbations, while altering infinitesimally the position of the line vortices, do not alter the line vortex strength. They may, however, induce an irrotational flow exterior to the patch. We hence introduce an analytic function $G(z, t) = \epsilon\hat{G}(z, t)$ in the region exterior to the domain D, and note the $F(z)$ after perturbation becomes $F(z, t) = F_0(z) + \epsilon\hat{F}(z, t)$. Again, $F_0(z)$ represents the unperturbed F function, and $\hat{F}(z, t)$ represents the alteration after perturbation. Hence the velocity field after perturbation can be expressed as
$$u - iv = \begin{cases} \dfrac{-i\omega}{2}\left(\bar{z} - \sum_{k=1}^{N} \dfrac{\gamma_s}{z - z_k(t)} - \dfrac{\gamma_0}{z - z_0(t)} - F(z, t)\right), & z \in D(t), \\ \dfrac{-i\omega}{2} G(z, t), & z \notin D(t); \end{cases} \tag{2.77}$$

3. Continuity of velocity across the patch boundary must still hold. Applying this condition, we form a Riemann-Hilbert problem for $F(z)$ and $G(z)$, which will allow the expression of $F(z)$ and $G(z)$ in terms of the perturbation coefficients by using the Plemelj formulae;

4. Expand the kinematic boundary condition and equations of motion for the line vortices to obtain a generalized eigenvalue problem, of form $\mathbf{Ax} = \sigma\mathbf{Bx}$, where $\mathbf{x}$ will be a vector consisting of the some boundary perturbation coefficients and the pre-images of the perturbed point vortex positions .

2.5.3 Numerical Method

Due to the more complicated conformal map, many calculations performed analytically for the shielded Rankine vortex become intractable for multipoles of higher order. Hence numerical methods must be applied. A spectral method based on Laurent series is used, which will ultimately result in a generalized eigenvalue problem. Much of the numerical work can be viewed as problems in linear algebra, and so the commercial package MATLAB was used, due to its powerful numerical linear algebra libraries.

The form of the perturbation is taken to be

$$\begin{aligned} z(\zeta,t) &= z_0(\zeta) + \epsilon\hat{z}(t) \\ \bar{z}(1/\zeta,t) &= \bar{z}_0(1/\zeta) + \epsilon\hat{\bar{z}}(t), \end{aligned} \tag{2.78}$$

where $\epsilon \ll 1$, and terms of $\mathcal{O}(\epsilon^2)$ are taken to be infinitesimally small. Line vortex perturbations are taken as

$$z_k(t) = z_{k0} + \epsilon\hat{z}_k, \quad k = 0, ..., N, \tag{2.79}$$

where z_{k0} is the unperturbed position of the k-th vortex, and $\hat{z}_k$ is the perturbation to it's position. The circulations of the line vortices are unchanged by the perturbation.

The unknown perturbation to the conformal map $\hat{z}(\zeta,t)$ is expressed as

$$\hat{z}(\zeta,t) = e^{\sigma t}\sum_{k=0}^{\infty}\hat{a}_k\zeta^k, \qquad \hat{\bar{z}}(1/\zeta,t) = e^{\sigma^* t}\sum_{k=0}^{\infty}\hat{a}_k^*\zeta^{-k}. \tag{2.80}$$

where $\{\hat{a}_n^*\}$ are assumed independent of $\{\hat{a}_n\}$. This is standard in stability analysis of patches of vorticity (see [44], [45]). In treating the boundary perturbation coefficients and their complex conjugates as independent variables, we simplify the stability calculation. The resulting solutions allow us to recreate the physical perturbations: consider the perturbation $\hat{z} = e^{\sigma t}F + e^{\bar{\sigma}t}\bar{G}$, with complex conjugate given by $\hat{\bar{z}} = e^{\bar{\sigma}t}\bar{F} + e^{\sigma t}G$. The σ are linearly independent, as they will be solutions of an eigenvalue problem, hence the computational technique will yield $(\hat{z}, \hat{\bar{z}}) = e^{\sigma t}(F, G)$ and $(\hat{z}, \hat{\bar{z}}) = e^{\bar{\sigma}t}(\bar{F}, \bar{G})$. From these, the physical perturbations can be reconstructed. This is then truncated at order $\mathcal{N}$ so that the unknown is now

$$\hat{z}(\zeta,t) \approx e^{\sigma t}\sum_{k=0}^{\mathcal{N}} \hat{a}_k \zeta^k \tag{2.81}$$

In the numerical method, the value of $\mathcal{N}$ is picked by choosing some $\mathcal{M}$, a power of two, and applying a fast Fourier transform (FFT) of order $\mathcal{M}$. The integer $\mathcal{N}$ will be chosen to be a power of 2 also, and $\mathcal{M}$ is chosen at least two powers of 2 larger than $\mathcal{N}$ to avoid aliasing errors. For example, with $\mathcal{M} = 64$, take $\mathcal{N} = 16$ and all functions will be expanded in the following spectral representation

$$G(\zeta) = \frac{G_{-6}}{\zeta^6} + \frac{G_{-5}}{\zeta^5} + ... + G_0 + ...G_5\zeta^5 + G_6\zeta^6 \tag{2.82}$$

so that there are precisely $2\mathcal{N} - 3$ spectral coefficients.

As discussed in §2.5.3 the $\{\hat{a}_n\}$ are to be determined numerically and the infinite set $\hat{a}_n$ is truncated to $\mathcal{N}/2 - 1$ terms, where $\mathcal{N}$ is a power of two. As in section 2.4.1, we set $\hat{\hat{a}}_1 = \hat{a}_1$ and $\hat{a}_0 = 0$.

As ζ is evaluated on $|\zeta| = 1$, or alternatively $\zeta = e^{is}$, and the FFT provides a series of form $X = \sum_n x_n e^{ins}$, the components of the Fourier transform provide the coefficients of the Laurent expansion of X. This allows us to utilise the convolution properties of Fourier transforms throughout our code , so providing significant speed increases. It is well known that fast Fourier transforms of n points requires computational effort of order $n \log n$, which compares favourably with other methods of calculating the Laurent coefficients.

If the quantities $\{\zeta_{k0}\}$ are defined as pre-images in the ζ-plane of the points $\{z_k\}$, then it is consistent to define the quantities $\{\hat{\zeta}_k\}$ by

$$z_k(t) = z_{k0} + \epsilon e^{\sigma t}\hat{z}_k \equiv z(\zeta_{k0} + \epsilon\hat{\zeta}_k, t), \quad k = 0, ..., N. \tag{2.83}$$

Similarly,

$$\hat{z}_k = \hat{\zeta}_k z_{0\zeta}(\zeta_{k0}) + \hat{z}(\zeta_{k0}), \quad k = 0, ..., N. \tag{2.84}$$

The quantities $\{\hat{\zeta}_k^*\}$ are again independent of $\{\hat{\zeta}_k\}$.

$$\hat{\hat{z}}_k = \hat{\zeta}_k^* z_{0\zeta}(\bar{\zeta}_{k0}) + \hat{\hat{z}}(\zeta_{k0}), \quad k = 0, ..., N. \tag{2.85}$$

Using the Riemann mapping theorem [35], the condition $z(0,t) = 0$ is specified. As for the shielded Rankine vortex, we can specify $a_0 = a_0^* = 0$. Additionally, we enforce $a_1 = a_1^*$, eliminating a rotational degree of freedom. This provides the set of $\mathcal{N} + 2N - 1$ unknowns

$$\begin{array}{ll} \left\{\hat{a}_k | k = 1 ... \frac{\mathcal{N}}{2} - 1\right\}, & \left\{\hat{a}_k^* | k = 2 ... \frac{\mathcal{N}}{2} - 1\right\}, \\ \left\{\hat{\zeta}_k | k = 0 ... N\right\}, & \left\{\hat{\zeta}_k^* | k = 0 ... N\right\}, \end{array} \tag{2.86}$$

which, after enforcing that the perturbed flow satisfies the Euler equations, will form a generalised eigenvalue problem.

2.5.4 Riemann-Hilbert Problem

From (2.87), the velocity field (2.73) for the general multipole case can be written as:

$$u - iv = \begin{cases} \dfrac{-i\omega}{2}\left(\bar{z} - \displaystyle\sum_{k=1}^{N} \frac{\gamma_s}{z - z_k(t)} - \frac{\gamma_0}{z - z_0(t)} - F(z,t)\right), & z \in D(t) \\ \dfrac{-i\omega}{2} G(z,t), & z \notin D(t), \end{cases} \tag{2.87}$$

where

$$\gamma_0 = -R z_{0\zeta}(0), \tag{2.88}$$

$$\gamma_s = \frac{R b z_{0\zeta}(a_{-1})}{N a^N}, \tag{2.89}$$

from [3]. $D(t)$ represents the perturbed vortex patch, with F analytic inside the patch, G analytic outside the patch. The $z_k(t)$ represent the perturbed vortex positions. Applying continuity of velocity on the patch gives

$$F(z,t) - G(z,t) = -\bar{z} + \sum_{k=1}^{N} \frac{\gamma_s}{z - z_k(t)} + \frac{\gamma_0}{z - z_0(t)} \qquad z \in \partial D(t). \tag{2.90}$$

which is, as for the shielded Rankine vortex (2.43), a Riemann-Hilbert problem (see [14]). In the case of the shielded Rankine vortex, this was solved by inspection. However, this case is too complex for solution by inspection. It is necessary to solve using the Plemelj formulae. This gives

$$\begin{aligned} F(z,t) &= \frac{1}{2\pi i}\oint_{\partial D(t)}\left(-\bar{z}' + \sum_{k=1}^{N}\frac{\gamma_s}{z'-z_k(t)}\right. \\ &\qquad \left. + \frac{\gamma_0}{z'-z_0(t)}\right)\frac{\mathrm{d}z'}{z'-z} \qquad z \in D(t), \end{aligned} \tag{2.91}$$

and

$$\begin{aligned} G(z,t) &= \frac{1}{2\pi i}\oint_{\partial D(t)}\left(-\bar{z}' + \sum_{k=1}^{N}\frac{\gamma_s}{z'-z_k(t)}\right. \\ &\qquad \left. + \frac{\gamma_0}{z'-z_0(t)}\right)\frac{\mathrm{d}z'}{z'-z} \qquad z \notin D(t). \end{aligned} \tag{2.92}$$

As the line vortices z_k are within D, this reduces to

$$F(z,t) = -\frac{1}{2\pi i}\oint_{\partial D(t)}\frac{\bar{z}'\mathrm{d}z'}{z'-z}, \qquad z \in D(t). \tag{2.93}$$

2.5.5 F functions

F functions on the patch boundary

The dependence of the function $F(z,t)$ on the perturbation coefficients (2.86) must now be determined. To do so, $F(z,t)$ is expanded in a Taylor series - by definition, F is analytic in the domain D, so this is valid. We shall then expand in terms of ζ, so we are implicitly defining the functions $\mathcal{F}_0(\zeta)$ and $\hat{\mathcal{F}}(\zeta)$ by the relation

$$F(z(\zeta,t),t) = \mathcal{F}_0(\zeta) + \epsilon\hat{\mathcal{F}}(\zeta)e^{\sigma t} + \emptyset(\epsilon^2). \tag{2.94}$$

Writing

$$F(z(\zeta),t) = \sum_{k=0}^{\infty} F_k z^k, \tag{2.95}$$

where the $F_k \in \mathbb{C}$ are the constant coefficients of the Taylor series, and expanding equation (2.93), it can be seen that

$$F_k = -\frac{1}{2\pi i}\oint_{\partial D}\frac{\bar{z}'}{z'^{k+1}}\mathrm{d}z', \quad k = 0,1,2,\ldots. \tag{2.96}$$

Then, as $z(\zeta) = z_0(\zeta) + \epsilon\hat{z}(\zeta,t)$, F_k can itself be expanded in ϵ, and

$$F_k = F_{k0} + \epsilon \hat{F}_k + \mathcal{O}(\epsilon^2). \tag{2.97}$$

Substituting $z(\zeta) = z_0(\zeta) + \epsilon \hat{z}(\zeta)$ into equation (2.93) and expanding, it follows that

$$F_{k0} = -\frac{1}{2\pi i} \oint_{\partial D} \frac{\bar{z}_0(\zeta^{-1}) z_{0\zeta}(\zeta)}{z_0(\zeta)^{k+1}} \mathrm{d}\zeta \tag{2.98}$$

and

$$\begin{aligned} \hat{F}_k \quad = \quad -\frac{1}{2\pi i} \quad & \left[\oint_{|\zeta|=1} \frac{\bar{z}_0(\zeta^{-1}) z_{0\zeta}(\zeta)}{z_0(\zeta)^{k+1}} \bar{\hat{z}}(\zeta) \mathrm{d}\zeta \right. \\ & - \oint_{|\zeta|=1} (k+1) \frac{\bar{z}_0(\zeta^{-1}) z_{0\zeta}(\zeta)}{(z_0(\zeta))^{k+2}} \hat{z}(\zeta) \mathrm{d}\zeta \\ & \left. + \oint_{|\zeta|=1} \frac{\bar{z}_0(\zeta^{-1})}{z_0(\zeta)^{k+1}} \hat{z}_\zeta(\zeta) \mathrm{d}\zeta \right]. \end{aligned} \tag{2.99}$$

The dependence of $\bar{\hat{z}}(1/\zeta)$ on the $\hat{a}_n^*$, and $\hat{z}(\zeta)$ and $\hat{z}_\zeta(\zeta)$ on the $\hat{a}_n$ is known, and hence we can calculate the dependence of the perturbations to the Taylor coefficients $\hat{F}_k$ on $\hat{a}_k$.

F functions near the line vortices

Similarly, we expand the $F(z,t)$ near the line vortex at z_k, to give a Taylor expansion

$$F(z,t) = \sum_{j=0}^{\infty} F_j (z - z_k)^j. \tag{2.100}$$

It will transpire we only require the first term of this sum and this quantity is given by

$$\begin{aligned} \hat{F}_k^{(lv)} \quad = \quad & -\frac{1}{2\pi i} \oint_{|\zeta|=1} \frac{(\zeta^{-1}) z_{0\zeta}(\zeta)}{z_0(\zeta) - z_{k0}} \bar{\hat{z}} \mathrm{d}\zeta \\ & -\frac{1}{2\pi i} \oint_{|\zeta|=1} \frac{\bar{z}_0(\zeta^{-1})}{z_0(\zeta) - z_{k0}} \hat{z}_\zeta(\zeta) \mathrm{d}\zeta \\ & -\frac{1}{2\pi i} \oint_{|\zeta|=1} \frac{\bar{z}_0(\zeta^{-1}) z_{0\zeta}(\zeta)}{(z_0(\zeta) - z_{k0})^2} (\hat{z}_k - \hat{z}(\zeta)) \mathrm{d}\zeta. \end{aligned} \tag{2.101}$$

This holds for all point vortices, the central line vortex expansion being given by the $k = 0$ quantity.

2.5.6 Kinematic boundary condition

Recall that the boundary of the patch of vorticity must move with the local velocity. Now that the dependence of $F(\zeta)$ on the $\hat{a}_k$ is known, this can be evaluated. Firstly, examining the $\mathcal{O}(\epsilon)$ terms in the linearised kinematic boundary condition gives the equation:

$$\begin{aligned}\sigma\mathbf{Re}\left[\frac{\bar{z}_{0\zeta}(\zeta^{-1})\hat{z}(\zeta)}{\zeta}\right] &= \mathbf{Re}\left[\frac{i\omega}{2}\zeta_{0\zeta}\left(\sum_{k=1}^{N}\frac{\gamma_s\hat{z}_k}{(z_0(\zeta)-z_{k0})^2}\right.\right. \\ &\qquad \left.\left. +\frac{\gamma_0\hat{z}_0}{[z_0(\zeta)]^2}-\sum_{k=0}^{\infty}\hat{F}_k z_0(\zeta)^k\right)\right].\end{aligned} \tag{2.102}$$

Using equations (2.99), (2.84) and (2.85), the dependence of equation (2.102) on the unknown perturbation coefficients is established. After truncating the infinite sum, coefficients of ζ are equated, to provide $\mathcal{N}-3$ equations.

2.5.7 Line vortex equations

The final requirement is that the line vortices must move with the non-self-induced local velocity. This requires a similar expression to equation (2.99) for z near the line vortices. Notating this as $\hat{F}^{(lv)}$, then

$$\begin{aligned}\sigma\bar{\hat{z}}_k &= -\frac{i\omega}{2}\left(\bar{\hat{z}}_k-\sum_{j\neq k}\frac{\gamma_s(\hat{z}_j-\hat{z}_k)}{(z_{k0}-z_{j0})^2}\right. \\ &\qquad \left. -\frac{\gamma_0(\hat{z}_0-\hat{z}_k)}{(z_{k0})^2}+\hat{F}_k^{(lv)}\right) \qquad k=1,...,N, \qquad (2.103) \\ \sigma\bar{\hat{z}}_0 &= -\frac{i\omega}{2}\left(\bar{\hat{z}}_0-\sum_{k=1}^{N}\frac{\gamma_s(\hat{z}_k-\hat{z}_c)}{(z_{k0})^2}+\hat{F}_0^{lv}\right),\end{aligned}$$

where

2.5.8 Eigenvalue problem

Through the kinematic boundary condition, the equations of motion of the line vortices and their complex conjugates, a total of $\mathcal{N}+2N-1$ equations are provided. As this is the same as the number of unknown perturbation coefficients, we may now form a well-posed matrix equation for this problem. We hence form a vector $\mathbf{x}$ of unknowns from equation (2.86). An eigenvalue problem is hence formed,

$$\mathbf{A}\mathbf{x} = \sigma\mathbf{B}\mathbf{x} \tag{2.104}$$

where $\mathbf{A}$ and $\mathbf{B}$ depend on the base state map. To find the entries of these matrices, the functions which depend on the base-state conformal map are Laurent or Taylor expanded using fast Fourier transforms. $\mathcal{N}$ and $\mathcal{M}$ are increased until the results are constant as $\mathcal{N}$ and $\mathcal{M}$ increase.

2.6 Checks on linear stability analysis

There are a number of checks which can be carried out on these linear stability results.

Firstly, both patch vortex and point vortex systems are Hamiltonian. This implies eigenvalues will occur as either pure real pairs, pure imaginary pairs or complex conjugate quartets. Hence Hamiltonian systems can be at best neutrally stable linearly. The results indeed satisfy this.

Secondly, recalling the presence of zero eigenvalue modes in the shielded Rankine vortex case, a number of zero eigenvalues are also expected in the multipolar case. These will correspond again to bifurcations to neighbouring steady states. Neighbouring states are present with altered patch area, and vortex centroid shifted in either of the two coordinate directions. The alteration of the patch area corresponds to altering R. These three modes are indeed found, and discarded from consideration. As for the shielded Rankine vortex, only perturbations which preserve the area and centroid of the patch are considered. Also, angular momentum is known to be preserved by the linearised Euler equations. As the initial angular momentum is zero, it is to be expected that the angular momentum after perturbation must also be zero.

As a consequence of this restriction, nonzero eigenvalues must also be checked to ensure the patch area and centroid are unchanged to order ϵ. The angular momentum of these nonzero eigenvalues is also shown to be zero to order ϵ.

As $a \to \infty$, the patch boundary tends to a circle, and the point vortices appear to the boundary to coalesced into a single point vortex. Hence as $a \to 0$, we expect the boundary modes to approach the spectrum of a shielded Rankine vortex, while the point vortex behaviour should echo that of a corotating point vortex array. This is because the patch boundary should be at sufficient distance for the effects of the patch to be viewed as providing a bulk rotation effect, countering any rotation the point vortex distribution would otherwise possess. We may take the limit $a \to \infty$ in (2.34), giving

$$b \sim \frac{2Na^N}{N-1}. \tag{2.105}$$

Then using (2.36), allows the ratio of the circulations of the point vortices to be calculated as

$$\frac{\Gamma_c}{\Gamma_s} \sim -\frac{N-1}{2} \tag{2.106}$$

in this limit, see Fig. 2.10. Comparing this ratio with the results of Morikawa and Swenson [19], we see that this ratio falls with in the stability range only for the case $N = 3$. Hence we expect that in the $a \to \infty$ limit, the $n = 3$ case but no others will be stable. As a decreases, this comparison with [19] may still prove of value, provided the patch and point vortices are not too close.

Also, for $N = 0$, the shielded Rankine vortex spectrum is retrieved, as expected.

As $a \to a_{crit}$, however, the Taylor expansion of $F(z, t)$ must be evaluated near the radius of convergence, as the line vortices tend towards the boundary. The values of $\mathcal{N}$ and $\mathcal{M}$ which must be taken for computational stability of the method to be

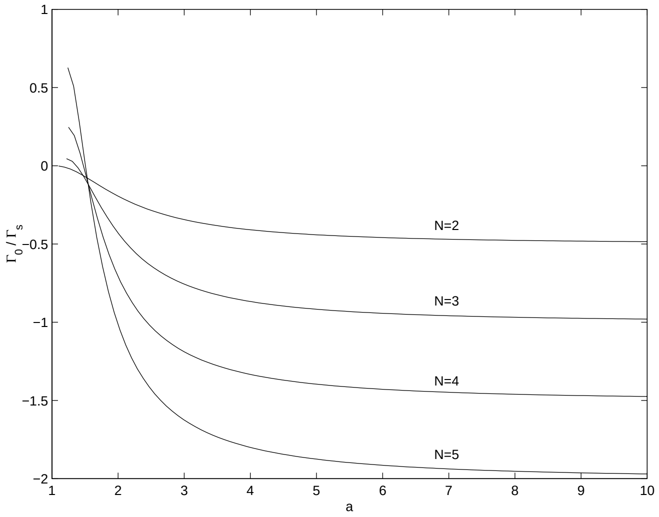

Fig. 2.10: Graph of $\frac{\Gamma_0}{\Gamma_s}$ for $N = 2, 3, 4$ and 5. As $a \to \infty$, ratio approaches asymptotic value given by (2.106).

achieved increases to a degree such that it becomes infeasible to calculate the linear stability. Hence as $a \to a_{crit}$, the linear stability becomes uncomputable using this method.

2.7 Linear stability results

The solutions presented here for $\omega = 1$. The eigenvalues are linear with ω, so obtaining growth rates for different ω is straightforward. The growth of any instabilities will be dominated by the largest positive real part of any eigenvalue. This will give the maximum growth rate for various parameters. The maximum growth rate is presented for varying N, the order of the multipole, over a range of a. As noted above, as $a \to a_{crit}$, $\mathcal{N}$ must increase dramatically to account for numerical errors introduced.

The linear stability results display different qualitative behaviour for various N values.

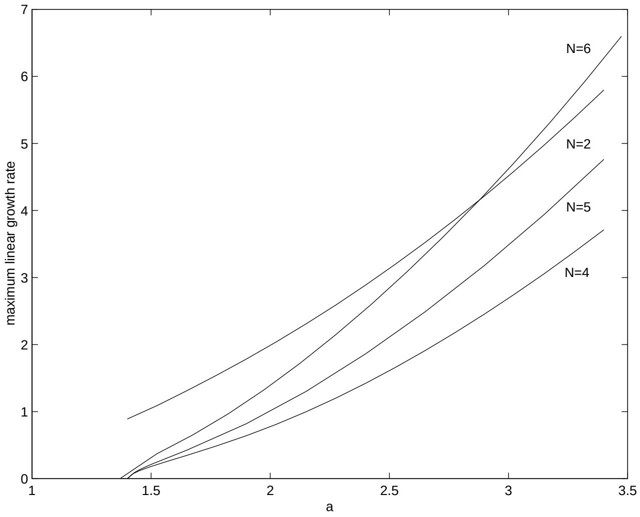

Fig. 2.11: Maximum linear growth rate against a for $N = 2, 4, 5$ and 6. The configurations for $N = 4, 5$ and 6 are found to become neutrally stable at $a^{(4)}_{stab} = 1.40$, $a^{(5)}_{stab} = 1.41$ and $a^{(6)}_{stab} = 1.37$.

2.7.1 N = 2 results

The tripolar, $N = 2$, solutions are found to be linearly unstable for all a. Figure 2.11 shows that the maximum linear growth rate decreases as $a \to a_{crit}$, but does not reach zero. For large a, the stability might be expected to decouple into terms corresponding to shielded Rankine vortex behaviour from the boundary, and behaviour corresponding to the Morikawa and Swenson point vortex model (see [19]), for the clustered line vortices.

The spectrum indeed separates in this manner. The most unstable eigenmode as $a \to \infty$ is that associated with the central line vortex. This is also consistent with the results of Morikawa and Swenson, as they find that for $N = 2$, perturbations of the central line vortex are responsible for instabilities.

2.7.2 N=3 results

The quadrupole is the only case which is found to neutrally stable for all a tested using this method.

2.7.3 N = 4, 5, 6 results

For $N = 4, 5, 6$ qualitatively different behaviour is found. For these N values, as a tends to infinity, the structure is unstable. However, as a falls below some critical value, a_{stab}, say, the configurations become neutrally stable. Any real eigenvalues pass through the origin, and become purely imaginary. For $N = 4$, a_{stab} is $a^{(4)}_{stab} = 1.40$, $a^{(5)}_{stab} = 1.41$ and $a^{(6)}_{stab} = 1.37$. Graphs are shown in Fig. (2.11). It is conjectured that this is true for N greater than 6, and this is confirmed for $N = 7$ and 8. For these higher order multipoles, the most unstable eigenmode for high a is associated purely with the satellite line vortex. Again, this is consistent with Morikawa and Swenson, who find that the satellite vortices are the cause of instability for $N > 4$.

2.8 Nonlinear Evolution - Contour Surgery

The nonlinear evolution of these structures may also be computed. It must be remembered, however, that linear stability does not imply nonlinear stability, and hence the correspondence of stability regions cannot be guaranteed. The solutions of Crowdy are a composite of two common vorticity models - the point vortex model and the patch vortex model. The contour dynamics method developed by Deem and Zabusky [25] to model the evolution of patch vortex configurations can easily be adapted to include the O.D.E.s necessary for time evolving the superposed line vortices. In these results, the more advanced routines of Dritschel's contour surgery code are used, adapted again to include the O.D.E.s corresponding to the line vortices.

These additional equations are checked by considering the unperturbed Thompson configuration of N line vortices placed in a ring. The angular velocity is given by

$$\Omega = \frac{\bar{\Gamma}(N-1)}{4\pi r_0^2} \tag{2.107}$$

where r_0 is the radial distance of each line vortex from the origin and $\bar{\Gamma}$ is the circulation of each vortex (see [32]). The angular velocity obtained through contour dynamics is indeed found to take the value Ω.

2.8.1 Shielded Rankine vortex

The stability of the shielded Rankine vortex is examined first. The main purpose of this is to examine whether a shielded Rankine vortex can destabilise into multipolar vortex structure. This is motivated by experimental data. Carton[9], found that perturbations of this form with sufficient magnitude cause the two-contour Rankine vortex to evolve into a multipolar structure, although these structures formed are not steady states. In a similar experiment, Morel and Carton[18] show that a three-contour Rankine vortex can also evolve after perturbation in to a multipole. As the shielded Rankine vortex can be considered as a limit of the two-contour Rankine vortex, it is feasible that the same qualitative results apply. Indeed, the following results confirm this.

The shielded Rankine vortex is shown earlier to be linearly neutrally stable. This does not necessarily mean that it will be non-linearly stable. The unperturbed structure is taken with patch radius $r = 1$. Perturbations of the form

$$r = 1 + A \cos m\theta, \tag{2.108}$$

are taken, where θ is the polar angular variable and A represents the amplitude of the perturbation. A need not be small, as the perturbations are non-linear. Under this class of perturbations, an $m = 3$ perturbation has the following behaviour. Firstly, the patch boundary folds in on itself, to form an approximately triangular central core, surrounded by semi-circular regions of vorticity on the outer boundaries which form the satellite regions with three-fold symmetry. These satellite regions have identical circulation, which is opposite in sign to that of the central patch. Such a formation can be seen in Fig. 2.12, at time $t = 3$, evolved from a shielded Rankine vortex perturbed with form (2.108), with magnitude $A = 0.4$. The shielded Rankine vortex is also perturbed under a $m = 5$ perturbation, and again form a clear penta-polar vortex, which can be seen in Fig. (2.13).

In contrast, a standard Rankine vortex is also examined, under the same perturbations Fig. 2.12. There are no clearly defined multipoles formed in this case, although thin filaments are expelled by the vortex patch. This contrast in results highlights the role that the central line vortices play in forming multipolar vortices.

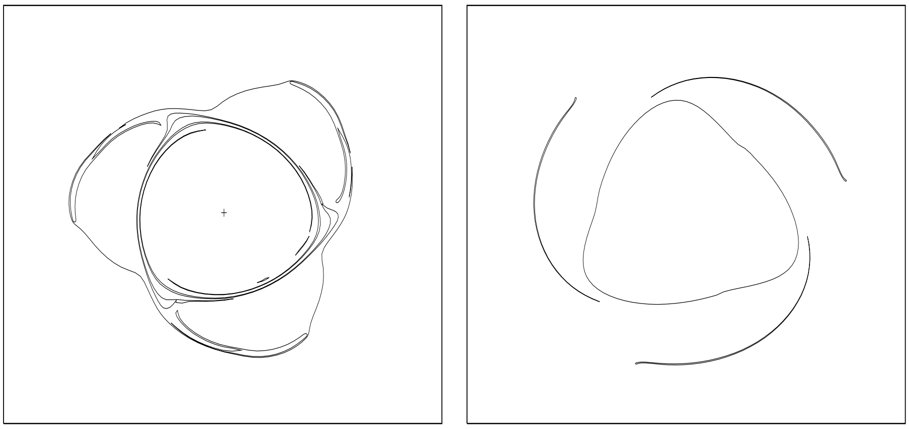

Fig. 2.12: Vortical configuration at $t = 3$ of shielded Rankine vortex (left diagram) and regular Rankine vortex (right diagram) perturbed by azimuthal mode-3 perturbation of the form (2.108) with amplitude $A = 0.4$. In contrast to the regular Rankine vortex, the shielded vortex forms a distinctly quadrupolar configuration.

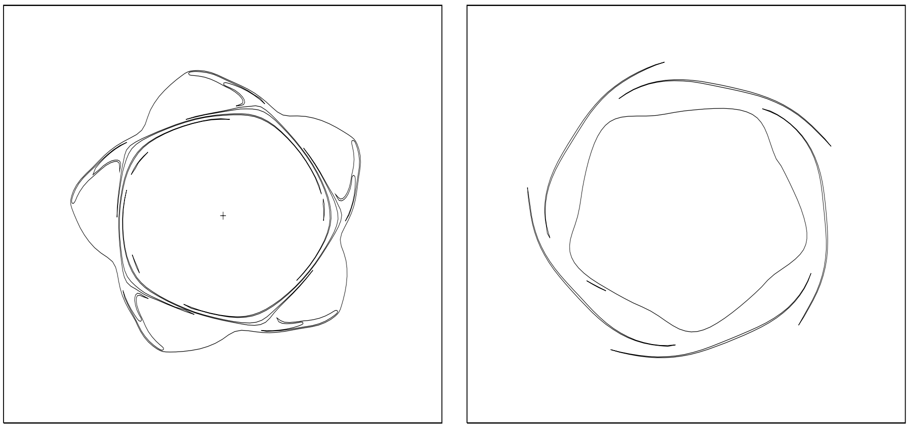

Fig. 2.13: Vortical configuration at $t = 3$ of shielded Rankine vortex (left diagram) and regular Rankine vortex (right diagram) perturbed by azimuthal mode-5 perturbation of the form (2.108) with amplitude $A = 0.3$. In contrast to the regular Rankine vortex, the shielded vortex forms a distinctly sexta-polar configuration.

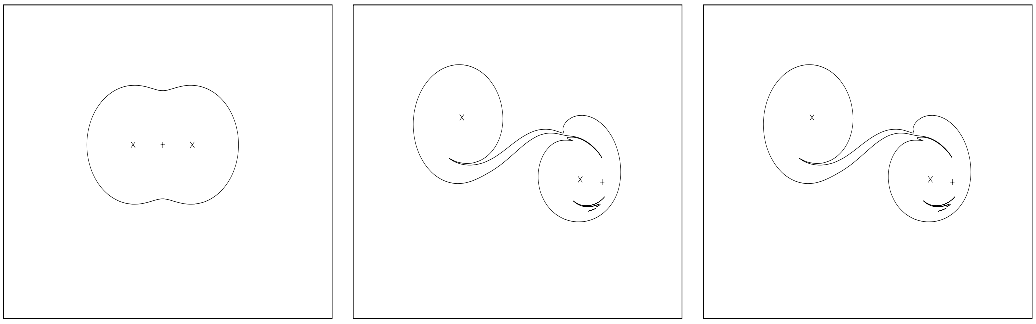

Fig. 2.14: Evolution of an unperturbed $N = 2$, $a = 2$ vortex at times $t = 0, 3.25$ and 5. The tripole splits into a monopole and a dipole by growth of an instability in which the central line vortex becomes displaced.

2.8.2 Non-linear multipolar stability and robustness

In this section, the unperturbed multipolar equilibria of [3] are time evolved using contour surgery with no perturbation. This is to provide a check on the equilibria found, and also investigate any numerical instabilities generated. There are some numerical issues involved with the contour dynamics evolution which must be addressed. Firstly, as $a \to a_{crit}$, the patch boundary becomes more cusped, and the number of points on the boundary must be increased. Also, as $a \to \infty$, the line vortices become close on the scale of the patch boundary, and the system of O.D.E.s suffers from stiffness problems. To counteract this, the time step is decreased.

The evolution of these unperturbed equilibria has one of two outcomes. Structures which are linearly stable remain in the equilibrium form. In structures which are linearly unstable, over long time scales, the small numerical errors which occur seed the instabilities and the structures breakdown after some period of time.

The tripole, ($N = 2$) is found to be linearly unstable for all a. As might be expected, for all a, the tripolar solutions breakdown after some (relatively large) period of time. All long time simulations of this unperturbed equilibria break down to form a monopole and dipole embedded in regions of patch vorticity. The initial instability is caused by movement of the central line vortex. This is consistent with the behaviour of the linear stability code, which for the largest eigenvalue, consists largely of a central line vortex perturbation, with small satellite vortex perturbations. This is shown in Fig. 2.14.

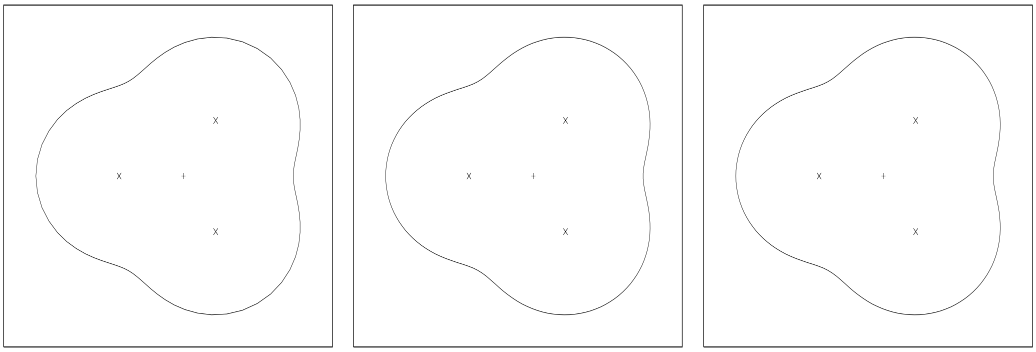

Fig. 2.15: Evolution of an unperturbed $N = 3$, $a = 2$ vortex at times $t = 0, 3.25$ and 5. No detectable change in the vortex is observed (even after much longer times).

The quadrupole has been shown to be linearly stable for all a. As expected, the equilibrium distribution is hence stable for all time. This provides a check that both the equilibria are correct and that the adaption to the code to include line vortices is correct. This is demonstrated in Fig. 2.15.

The pentapole and higher structures have the property that they are linearly unstable above some a value, a_{stab}, and neutrally stable below this. As expected, these structures are robust for the linearly neutral a values, and disintegrate after some significant time period for the linearly unstable a values. However, for these N values, the mechanism of the disintegration is the instability of satellite vortices. This corresponds with the linear stability results, in which the unstable eigenmodes of the largest eigenvalues are associated with the satellite point vortices. The breakdown of these structures forms a dipole, and $N - 1$ monopoles. For the regions of a above a_{stab}, a is larger than a_{asym}. For $a > a_{asym}$, Γ_c is of different sign from Γ_s. For $a < a_{asym}$, they are of the same sign. Hence the formation of this dipole is a foreseeable consequence of breakdown. An example of this for the pentapole is shown in Fig. 2.16.

An interesting phenomenon is observed for certain values of a for $N > 4$. The linear instability of the satellite vortices, seeded by numerical errors seems to be balanced by some non-linear effects. This causes a "dance" to take place, involving the satellite vortices moving from their positions around the central vortex, before swapping positions with other satellite vortices. This movement perturbs the patch temporarily, but the original shape is restored as the point vortices regain an equi-

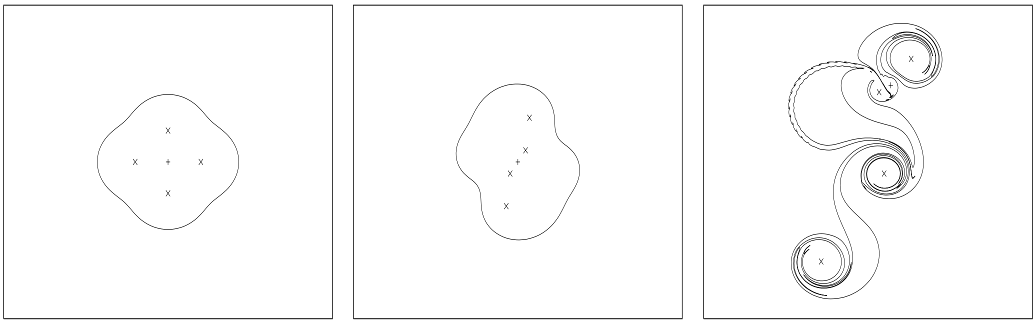

Fig. 2.16: Evolution of an unperturbed $N = 4$, $a = 2$ vortex at times $t = 0, 3.25$ and 5. The vortex is seen to decompose into three monopoles and a dipole by growth in the displacements of the satellite line vortices.

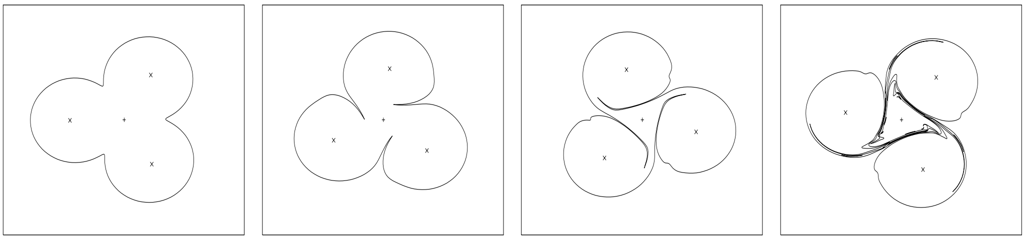

Fig. 2.17: Nonlinear response of a quadrupolar vortex ($a = 1.37$) to a perturbation in which all satellite line vortices (each of strength $\Gamma_s = 2.563$) are moved outwards by 0.1. The strength of the central line vortex is negligible. A slight rearrangement of the patch vorticity occurs and the structure rotates anti-clockwise but retains its overall quadrupolar form. Times shown are $t = 0, 1, 2$ and 5.

librium position. This interesting phenomenon is similar to observations made by Morikawa and Swenson. They found similar behaviour with even numbered groups of line vortices, providing the perturbation is small enough.

2.8.3 Non-linear evolution of perturbed equilibria

The result of perturbing this class of solutions is now examined. The class of perturbations is restricted to perturbations of the radial position of the satellite vortices.

The quadrupole is examined first. Figure 2.17 shows the evolution of the $a = 1.37$ quadrupole, perturbed so the satellite line vortices are initially a distance 1.1 from the origin. The structure rotates slowly anticlockwise, with a small alteration of the patch boundary. Figure 2.18 shows the same base state, with the satellite vortices moved inwards to the position 0.9 from the central line vortex. This causes a more pronounced alteration of the patch boundary, with the boundary folding over

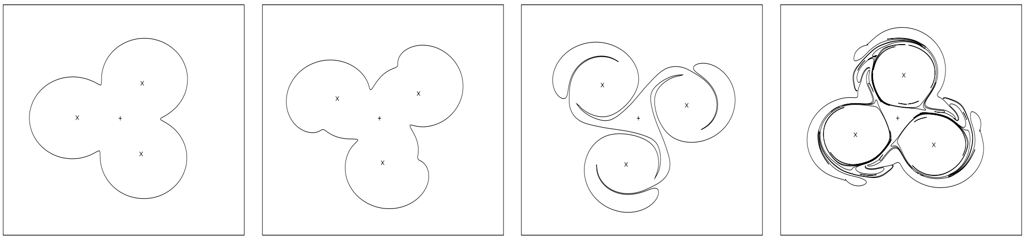

Fig. 2.18: Nonlinear response of a quadrupolar vortex ($a = 1.37$) to a perturbation in which all satellite line vortices (each of strength $\Gamma_s = 2.563$) are moved inwards by 0.1. The strength of the central line vortex is negligible. There is a more dramatic rearrangement of the patch vorticity than in Figure 2.17 but the structure retains its overall quadrupolar form and rotates steadily in a clockwise direction. Times shown are $t = 0, 1, 2$ and 5.

onto itself, and a rotation clockwise. The process of folding causes some contour surgery to be performed, and filamentation also takes place. Some circulation is lost through these processes. Note that the self reorganisation to a rotating form is highly suggestive of a bifurcation to a neighbouring steady state.

The pentapole and higher structures provide an interesting demonstration. For $a > a_{stab}$, perturbations of the satellite line vortices cause a disintegration of the multipole structure in roughly e-fold time. This is demonstrated by Fig. 2.19, with $a = 1.65$ and the satellite vortices perturbed by 0.1 outwards. Figure 2.20 shows the evolution of a pentapolar structure with $a < a_{stab}$, in fact $a = 1.4$. As with the quadrupole, this linearly stable structure undergoes a rearrangement of patch boundary and rotates anticlockwise, in a robust fashion for long time periods (this simulation was run up to $t = 10$). By $t = 7.5$, however, the $a = 1.65$ structure has disintegrated.

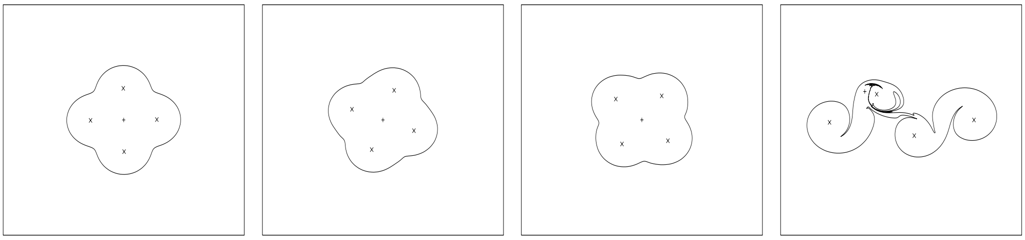

Fig. 2.19: Nonlinear response of a pentapolar vortex ($a = 1.65$) to a perturbation in which all satellite line vortices are moved outwards by 0.1. This structure is linearly unstable with a linear growth rate of approximately 0.1. The structure rotates steadily for a while but by $t = 7.5$ (roughly the e-fold time according to linear theory) it has eventually disintegrated. Times shown are $t = 0, 2.5, 5$ and 7.5.

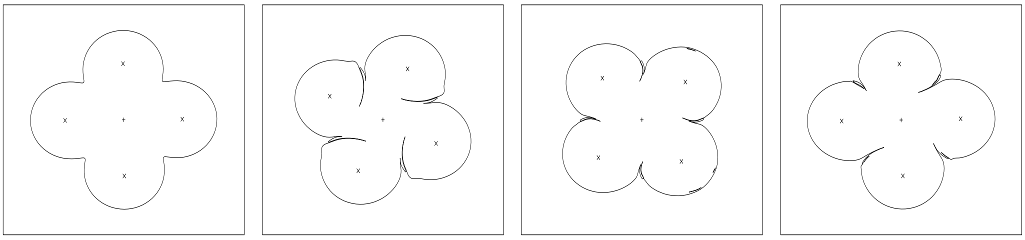

Fig. 2.20: Nonlinear response of a pentapolar vortex ($a = 1.4$) to a perturbation in which all satellite line vortices are moved outwards by 0.1. This structure sits on the linear stability boundary. The structure is slowly rotating anti-clockwise and retains its pentapolar form. Times shown are $t = 0, 2.5, 5$ and 10.

From a large number of numerical runs, two types of behaviour are observed for the perturbed multipoles, one stable and one unstable. These behaviour patterns are found to behave as might be expected from the linear stability results. In a regions which are linearly stable, perturbations are found to steadily rotate for long periods of time. This follows reorganisation of the patch vorticity. Linearly unstable structures however, disintegrate within roughly e-fold time.

Further illustration of this can be seen in the following figures. Figures (2.20) and (2.21) show configurations with $N = 8$ and $a = 1.4$ and $a = 1.3$. The base states are perturbed by the satellite vortices moving outwards by 0.1. The $a = 1.4$ is linearly unstable, with maximum growth rate of 0.31, and indeed breaks down by $t = 7.5$. The $a = 1.3$ configuration, which is linearly stable, rotates steadily up until $t = 15$.

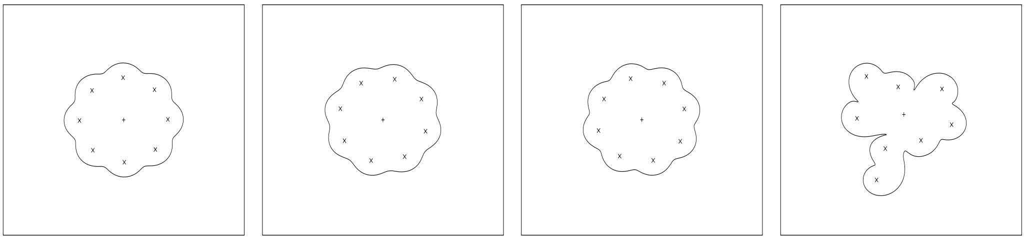

Fig. 2.21: Nonlinear response of an 8-polar vortex with $a = 1.4$ to a perturbation in which all satellite line vortices are moved outwards by 0.1. This configuration has a maximum linear growth rate of 0.31. Times shown are $t = 0, 2.5, 5$ and 7.5. The configuration rotates steadily for a while, but by $t = 7.5$ (roughly the e-fold time according to linear theory) the structure has disintegrated.

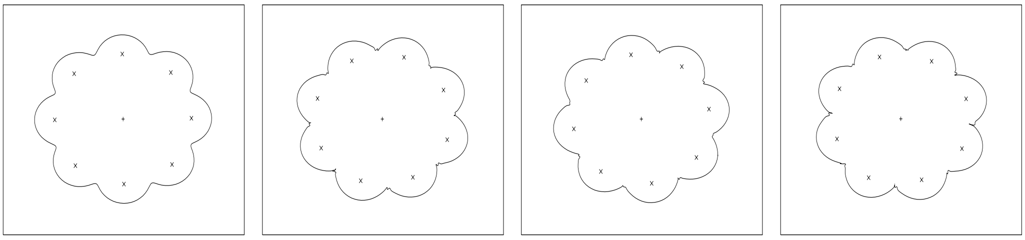

Fig. 2.22: Nonlinear response of an 8-polar vortex with $a = 1.3$ to a perturbation in which all satellite line vortices are moved outwards by 0.1. Times shown are $t = 0, 2.5, 5$ and 10. This structure is neutrally stable according to linear theory. The configuration rotates steadily and maintains its structural form under evolution. Note that small ripples in the boundary occur at the points of highest curvature.

This suggests that the perturbation being considered indeed counts as a linear one.

2.8.4 Discussion

It has been shown that, with the exception of the tripolar solution, this class of multipolar solutions has the same stability properties as found in laboratory and numerical experiments. The tripole is found in this formulation to be linearly and nonlinearly unstable, which is in contradiction to the findings of [18], who find it to be stable. Quadrupoles are found to be linearly neutrally stable for all a values, and the structure is robust under nonlinear evolution. While it is generally accepted that tripole and quadrupole structures are the only stable formulations, for some parameter values, it seems the formulation of [3] admits linearly stable and non-linearly robust multipoles of higher order. The stable region is for small a, which corresponds to a deformed patch and satellite vortices some distance from the central line vortex. At this scale, it is possible that replacing the point vortices with patch vorticity, as in purely patch based models, or traditional fluid dynamical experiments may introduce some shape related effects to the perturbation, which cause instabilities. A laboratory experiment of these particular configurations, using the Malmberg-Penning trap would be of some interest.

With the case of the tripole, it is conjectured that the combined constraints that the total structure has zero circulation *and* be non-rotating force the respective strengths of the central and satellite line vortices to be such that linear stability of the configuration is not possible. It is possible that a generalisation of this form to equilibria involving line vortices superposed on a patch in a steadily rotating configuration might produce stable tripoles. However, it seems unlikely that these equilibria would be exact. It is possible, however, that they could be obtained as perturbations of these stationary exact solutions.

Owing to the method used, which depends upon convergence of power series, it has not been possible to study the linear stability of the limiting configurations of these structures.

The preceding stability analysis is based on work of Crowdy and Cloke [4].

CHAPTER 3

Analytical solutions for distributed multipolar vortex equilibria on a sphere

The phenomena motivating the work of Chapter 2 are commonly observed in either the atmosphere, or in laboratory or numeric work based on atmospheric conditions [41, 8, 7]. Hence it is natural to enquire if the class of exact multipolar solutions can be extended to include curvature effects which would occur if they were placed in the atmosphere. To this end, we show it is possible to extend these solutions to the surface of a sphere. On the sphere, an extra length scale will be introduced, as the vorticity patch can occupy at most an area of $4\pi r^2$, taking r as the radius of the sphere, whereas on the plane, any change in patch size can be viewed merely as a rescaling of a different solution. Consequently, the one parameter family obtained on the plane becomes a two parameter family on the sphere.

This chapter will present a generalisation of the exact planar solutions of Crowdy [3] to the surface of a non-rotating sphere. Note that this surface is still inherently two dimensional, but has been embedded in three dimensional space. Firstly we will detail the representation of inviscid 2-D fluids on the surface of the sphere using complex variables. The stereographic projection from the complex plane to the sphere will be introduced, and the form of patch and point vorticity will then be presented for the now complex equations of motion. It will become apparent that in this geometry the shielded Rankine vortex is the simplest possible form of point vorticity, which provides a further retrospective justification for the shielded Rankine vortex model used on the plane. From now on, all references to fluid motion on a sphere are taken to refer to motion on the surface of a sphere.

The exact solutions below are presented in Crowdy and Cloke [5].

3.1 Overview

Models of behaviour of vorticity on the sphere are inevitably primarily associated with modelling planetary scale geophysical systems. On the scale of these systems, curvature effects of the Earth's surface can play a major role in the dynamics. A case in point is the behaviour of the polar vortices. Interestingly, multiple vortex equilibria are physically related to major warming events in the stratosphere when the polar vortex is broken into many pieces [28]. Previous models have largely been based on point vortex models, although some attention has also been paid to purely patch based models, for example Polvani and Dritschel in [28]. The stereographic projection will be presented, which maps the surface of the sphere to the complex plane, and hence allows techniques of complex analysis to be utilized. The stereographic projection is mentioned in [26], but seems to be largely neglected by most authors. As it is such a powerful tool, it is surprising that it is not more widely used. The use of this map allows a much simplified form when calculating vortex patch and line vortex behaviour, compared to the calculation in Cartesian or polar coordinates.

This section demonstrates that using the Schwarz function methods of Crowdy [3], it is possible to combine patch and point vortex models on the sphere as well as on the plane. In this chapter, the planar techniques of Chapter 2 will be modified to create a class of coherent structures which are exact and stationary on the sphere.

While the full curvature effects of the sphere are taken into account, the sphere will remain non-rotating. In the following chapter, the stability to small amplitude perturbations of these structures will be examined.

3.2 Mathematics

The topology of the surface of a sphere, as opposed to the unbounded plane, will produce different dynamics in two fundamental aspects. These both derive from the surface of a sphere being closed and compact, and affect the class of admissible solutions. Firstly, the surface of the sphere has a non zero curvature. This enforces a characteristic length-scale not present on the unbounded plane. Secondly, as a consequence of Gauss' Theorem, the integral of the scalar vorticity field over the spherical surface must be zero. This constraint does not exist on the plane.

In light of these differences, we pose the following question: Is it possible to generalise the Schwarz function based method of Crowdy [3] onto the sphere?

3.2.1 Stereographic projection and Laplace operator

A fundamental requirement for the planar solutions of Chapter 2 is that the equations of motion must be in complex variables. The stereographic projection is a mapping which maps between the extended complex plane and the surface of a sphere. Hence this is utilised to map the equations of motion on the sphere onto the complex plane. The projection is constructed as follows.

Take the Cartesian coordinate system (x, y, z). Then if $\zeta = x + iy$, the $(x, y, 0)$ plane can now be considered as the complex plane, with ζ a complex variable lying on this plane (Fig. 3.1). Additionally, define a sphere, S, of radius ρ_s, centred on the origin. Suppose then that $\mathbf{s}$ is a point on the surface of the sphere. Then a line $\mathbf{l}$ is constructed which passes through the north pole of the sphere (the point $(0, 0, \rho_s)$) and through the point $\mathbf{s}$. Then at some point, ζ_s say, $\mathbf{l}$ passes through the plane $(x, y, 0)$, on which the complex variable ζ is defined. This point ζ_s is the unique map of the point $\mathbf{s}$ onto the complex plane using the stereographic projection. Note that the south pole of the sphere $(0, 0, -\rho_s)$, maps to $\zeta = 0$, while the north pole $(0, 0, \rho_s)$ is taken as mapping to infinity, in the sense of the extended complex plane. The equator of the sphere will map to the circle $\zeta\bar{\zeta} = r_s^2$. This ζ-plane will be mapped to using some conformal map from a new complex η-plane (see Fig. 3.1)

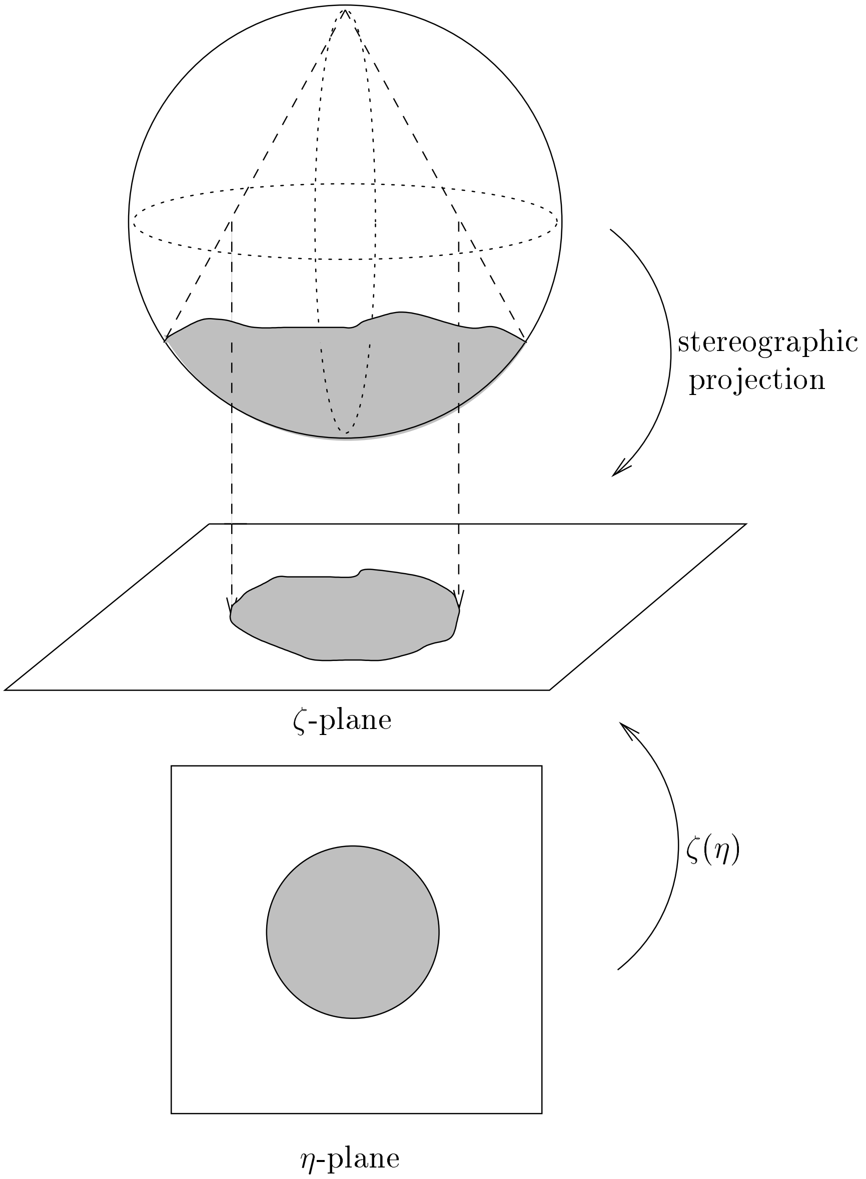

Fig. 3.1: Schematic illustrating the stereographic projection from the physical sphere to a complex ζ-plane and conformal mapping to the ζ-plane from the unit-disc in a complex η-plane.

Express the point **s** on the surface of the sphere in terms of spherical polar coordinates, (r, θ, ϕ), where r is the distance from the origin, θ is the latitude measured from the north pole, and ϕ is the longitude. Without loss of generality, the sphere is taken to have unit radius, so $\rho = 1$ for all points on the surface. Then it is straight forward to demonstrate that the projection of the point **s** from the surface of the sphere to the ζ-plane can be written as

$$\zeta = re^{i\phi}, \tag{3.1}$$

where

$$r = \cot\left(\frac{\theta}{2}\right), \tag{3.2}$$

where (r, ϕ) are the polar coordinates of the ζ-plane.

After some algebra, the relations

$$\begin{aligned} \cos\theta &= \frac{\zeta\bar{\zeta} - 1}{\zeta\bar{\zeta} + 1} \\ \sin\theta &= \frac{2\sqrt{\zeta\bar{\zeta}}}{\zeta\bar{\zeta} + 1} \end{aligned} \tag{3.3}$$

may also be derived.

3.2.2 Equations of motion on the sphere

The velocity vector on the surface of the sphere has the form

$$\mathbf{u} = (0, v, u) = (0, \mathbf{u}_\theta, \mathbf{u}_\phi),$$

where v and u are velocity field components in the θ (zonal) and ϕ (meridional) directions, respectively. $\mathbf{u}_\theta$ and $\mathbf{u}_\phi$ represent the components of $\mathbf{u}$ in the θ and ϕ directions.

The flow is assumed to be incompressible, hence a scalar stream-function ψ can be introduced using the relation

$$\mathbf{u} = \nabla_\Sigma \psi \times \mathbf{e}_r, \tag{3.4}$$

where $\mathbf{e}_r$ is the radial unit vector, and

$$\nabla_\Sigma = \mathbf{e}_\theta \frac{\partial}{\partial\theta} + \frac{\mathbf{e}_\phi}{\sin\theta}\frac{\partial}{\partial\phi} \tag{3.5}$$

is grad in spherical polar co-ordinates.

Hence

$$u = \quad -\frac{\partial\psi}{\partial\theta} \tag{3.6}$$

$$v = \frac{1}{\sin\theta}\frac{\partial\psi}{\partial\phi}. \tag{3.7}$$

From vector calculus, it is possible to introduce a scalar vorticity field, $\omega(\theta, \phi)$ such that

$$\omega\mathbf{e_r} = \nabla_\Sigma \times \mathbf{u}. \tag{3.8}$$

Then

$$\omega = -\nabla^2_\Sigma \psi, \tag{3.9}$$

where

$$\nabla_\Sigma f = \frac{\partial f}{\partial\theta}\mathbf{e}_\theta + \frac{1}{\sin\theta}\frac{\partial f}{\partial\psi}\mathbf{e}_\psi, \tag{3.10}$$

and ∇^2_Σ is the spherical Laplace operator, known as the *Laplace-Beltrami* operator,

$$\nabla^2_\Sigma = \frac{1}{\sin^2\theta}\frac{\partial^2}{\partial\phi^2} + \frac{1}{\sin\theta}\frac{\partial}{\partial\theta}\left(\sin\theta\frac{\partial}{\partial\theta}\right). \tag{3.11}$$

Then u and v are given as

$$\begin{aligned} u &= -\frac{\partial \psi}{\partial \theta}, && (3.12) \\ v &= \frac{1}{\sin\theta}\frac{\partial \psi}{\partial \phi}. && (3.13) \end{aligned}$$

Applying the chain rule, it is apparent that

$$\begin{aligned} \left.\frac{\partial}{\partial \theta}\right|_{\phi} &= -\frac{\zeta}{\sin\theta}\left.\frac{\partial}{\partial \zeta}\right|_{\bar{\zeta}} - \frac{\bar{\zeta}}{\sin\theta}\left.\frac{\partial}{\partial \bar{\zeta}}\right|_{\zeta}, \\ \left.\frac{\partial}{\partial \phi}\right|_{\theta} &= i\zeta\left.\frac{\partial}{\partial \zeta}\right|_{\bar{\zeta}} - i\bar{\zeta}\left.\frac{\partial}{\partial \bar{\zeta}}\right|_{\zeta}. \end{aligned} \tag{3.14}$$

Using (3.14), the following form of (3.11) is obtained:

$$\nabla^2_{\Sigma}\psi = (1+\zeta\bar{\zeta})^2\psi_{\zeta\bar{\zeta}}. \tag{3.15}$$

Eqn. (3.6) is manipulated to provide the expression for the velocity field in spherical polars on the surface of sphere,

$$u_{\phi} - iu_{\theta} = \frac{2\zeta}{\sin\theta}\psi_{\zeta}. \tag{3.16}$$

Cartesian components of the velocity on the ζ-plane is given by

$$u - iv = -\frac{i}{2}(1+\zeta\bar{\zeta})^2\psi_{\zeta}. \tag{3.17}$$

3.3 Fundamental solutions

To proceed, it is necessary to determine the forms of patch vorticity and point vortices on the surface of the sphere. On the plane, this is achieved by solving the equations

$$\nabla^2\psi = \omega_0, \tag{3.18}$$

for patch vorticity, and

$$\nabla^2\psi = \alpha\delta(z,\bar{z}) \tag{3.19}$$

for a point vortex. The forms on the sphere will be determined in an analogous manner, although with some modification to the point vortex expression to ensure the Gauss condition is satisfied.

3.3.1 Patch Vorticity

Firstly, for patch vorticity, we solve

$$\nabla^2_\Sigma \psi = -\omega_0 \tag{3.20}$$

Applying (3.15) this becomes

$$(1+\zeta\bar{\zeta})^2 \psi_{\zeta\bar{\zeta}} = -\omega_0, \tag{3.21}$$

which can be directly integrated to give

$$\begin{aligned} \psi_\zeta &= -\int \frac{\omega_0}{(1+\zeta\bar{\zeta})^2} \mathrm{d}\bar{\zeta} \\ &= \frac{\omega_0 \bar{\zeta}}{1+\zeta\bar{\zeta}}. \end{aligned} \tag{3.22}$$

The last step follows by choosing the arbitrary function of integration such that ψ_ζ is regular at $\zeta = 0$. Integrating again, the expression for patch vorticity on a sphere is derived to be

$$\psi = \omega_0 \int^\zeta \frac{\bar{\zeta}'}{1+\zeta'\bar{\zeta}'} \mathrm{d}\zeta' = \omega_0 \log(1+\zeta\bar{\zeta}). \tag{3.23}$$

3.3.2 Line Vortices on the surface of a sphere

The naive streamfunction for a point vortex on the sphere would be ϕ such that

$$\nabla^2_\Sigma \psi = \delta(\theta, \phi; \theta', \phi').$$

The precise definition of δ is perhaps no longer immediately clear, as the surface of integration is no longer a plane. Merely taking $\delta(\theta, \psi; \theta', \phi')$ such that

$$\int_D f(\theta,\phi)\delta(\theta,\phi;\theta',\phi')\mathrm{d}\theta\mathrm{d}\phi = \begin{cases} f(\theta',\phi'), & (\theta',\phi') \in D \\ 0, & (\theta',\phi') \notin D \end{cases} \tag{3.24}$$

is inappropriate. To see this, consider the integral of the vorticity over the whole sphere. Recalling that $\mathrm{d}\sigma = \sin\theta \mathrm{d}\theta \mathrm{d}\phi$, then

$$\int \omega \mathrm{d}\sigma = \int \delta(\theta, \phi, \theta', \phi') \sin\theta \mathrm{d}\theta \mathrm{d}\phi = \sin\theta'.$$

Clearly, as the sphere is not rotating and hence all spherical symmetry is present, the integral of vorticity should have no relation to the latitude θ' at which the vortex is placed. We then define the delta-function on the surface of the sphere to satisfy

$$\int_D f(\theta, \phi)\delta(\theta, \phi, \theta', \phi')\mathrm{d}\sigma = \begin{cases} f(\theta', \phi'), & (\theta', \phi') \in D \\ 0, & (\theta', \phi') \notin D \end{cases}, \tag{3.25}$$

where σ is the surface of the sphere, $\mathrm{d}\sigma$ is an area element on the sphere, and D is some domain on the surface of the sphere.

However, consider again the integral of vorticity over the surface of the sphere. We integrate over the infinitesimally thin volume, giving

$$\begin{aligned} \textstyle\int_V \omega \mathrm{d}V &= -\int_V \nabla^2_\Sigma \psi \mathrm{d}V \\ &= -\int_V \nabla_\Sigma . (\nabla\psi) \mathrm{d}V \\ &= -\int_{\partial V} \nabla\psi . \mathbf{n} \mathrm{d}S \\ &= -\int_{\partial V} \nabla\psi . \mathbf{e}_r \mathrm{d}S \\ &= 0, \end{aligned} \tag{3.26}$$

after using Gauss' theorem and noting that $\mathbf{e}_r$ and $\nabla\psi$ are perpendicular. Hence, the integral of vorticity must be equal to zero. Subtract, then, some function from the expression (3.3.2), the most obvious being the constant $1/4\pi$. A point vortex on the surface of a sphere is therefore taken to be the solution of

$$\nabla^2_\Sigma \psi = \delta(\theta, \phi, \theta', \phi') - \frac{1}{4\pi}. \tag{3.27}$$

Using Green's functions,

$$\psi = \frac{1}{4\pi}\log(1-\cos\gamma), \tag{3.28}$$

where

$$\cos\gamma = \cos\theta\cos\theta' + \sin\theta\sin\theta'\cos(\phi-\phi'). \tag{3.29}$$

Using (3.3) it can be shown that

$$1-\cos\gamma = \frac{2(\zeta-\zeta')(\bar{\zeta}-\bar{\zeta}')}{(1+\zeta\bar{\zeta})(1+\zeta'\bar{\zeta}')}. \tag{3.30}$$

Then a line vortex of circulation Γ at the point ζ_s has streamfunction

$$\psi(\zeta,\bar{\zeta}) = -\frac{\Gamma}{4\pi}\log\left(\frac{2(\zeta-\zeta_s)(\bar{\zeta}-\bar{\zeta}_s)}{(1+\zeta\bar{\zeta})(1+\zeta_s\bar{\zeta}_s)}\right). \tag{3.31}$$

We can also use the strength of the line vortex, defined as $\kappa = \Gamma/2\pi$. Note that (3.27) and (3.31) include some constant vorticity over the whole surface of the sphere. Hence it is now apparent that the simplest example of point vorticity on the sphere is a point vortex embedded in some region of patch vorticity. The form of the point vortex on the sphere retrospectively justifies the use on the plane of the shielded Rankine vortex. The fact that isolated point vortices on the sphere must be combined with patch vorticity shows that the combination is not merely an artificial construct, but is a fundamental and natural form.

3.4 Schwarz function method on the sphere

3.4.1 Adapting the Schwarz function to the surface of a sphere

Recall that the planar Schwarz function solutions take the form

$$\psi(z,\bar{z}) = \begin{cases} -\frac{\omega}{4}\left(z\bar{z} - \int^{z} S'(z')dz' - \int^{\bar{z}} S'(z')dz'\right), & z \in D \\ 0, & z \notin D, \end{cases} \tag{3.32}$$

so

Note that the region D is chosen such that $S(z)$, the Schwarz function, is meromorphic and has only simple poles with real residues.

The property which is of interest in forming these models, then is that the Schwarz function cancels the patch vorticity on the boundary of the patch. An extension of the Schwarz function is sought for vorticity distributions on the sphere.

Heuristically, this extension must cancel the expression for a patch of vorticity on ∂D, and it is expected that it will then contain point vortex terms for suitable domains. Additionally, we require $\mathrm{d}\psi = \psi_\zeta \mathrm{d}\zeta + \bar{\psi}_{\bar{\zeta}} \mathrm{d}\bar{\zeta} = 0$ on ∂D, so ∂D is a streamline.

Postulate a streamfunction

$$\psi(\zeta, \bar{\zeta}) = \begin{cases} -\omega_0 \left(\log(1+\zeta\bar{\zeta}) - \int^{\zeta} S_{sph}(\zeta')\mathrm{d}\zeta' - \int^{\bar{\zeta}} \bar{S}_{sph}(\zeta')\mathrm{d}\zeta' \right), & z \in D \\ 0, & z \notin D. \end{cases} \tag{3.33}$$

From (3.22), the patch vorticity on a sphere is

$$\psi_\zeta = \frac{\bar{\zeta}}{1+\zeta\bar{\zeta}}.$$

If $S_{sph}(\zeta)$ is defined as

$$S_{sph}(\zeta) = \frac{S(\zeta)}{1+\zeta S(\zeta)}, \tag{3.34}$$

then $S_{sph}(\zeta)$ cancels the patch vorticity on ∂D and satisfies $\mathrm{d}\psi = \psi_\zeta \mathrm{d}\zeta + \psi_{\bar{\zeta}} \mathrm{d}\bar{\zeta} = 0$ on the boundary. Hence S_{sph} can be considered the analogue of the Schwarz function for distributions on the surface of a sphere.

3.5 Exact Multipolar Vortices on a Sphere

It is shown in this section that the Schwarz function method as adapted for the surface of the sphere can now be used to create Multipole solutions on the sphere, with an appropriate conformal map. This choice of conformal map will depend, as in the planar case on some parameters which will be determined by the equations which are derived to ensure stationarity.

As on the plane, singularities in S_{sph} are required to only have simple poles with real residues, for physicality. The conformal map must consequently be chosen to satisfy this, and also ensure that the stationarity condition on the line vortices is satisfiable.

3.5.1 Choice of conformal map

It may at first appear that the Schwarz function method of Crowdy allows us to create vortical equilibria at will. However, in practice, there is still considerable difficulty in choosing the conformal maps such that the stationarity condition may be satisfied - this is the only condition left to satisfy, assuming the map chosen is a physical one.

An initial approach might be to postulate that the conformal map used in the planar case would also satisfy the stationarity condition on the sphere. It will be shown that this is indeed the case, i.e.

$$\zeta(\eta) = R\left(\eta + \frac{b\eta}{\eta^N - a^N}\right) \tag{3.35}$$

is a suitable conformal map, where the unit η-circle is mapped onto the complex ζ-plane, and then into the z-sphere, by the stereographic projections. The parameters R, a, b and N, will be chosen to satisfy the stationarity condition.

It is obviously a condition of physicality that the vortex patch boundary on the sphere should not cross itself. Due to the stereographic projection being univalent, this implies that the projected boundary on the complex ζ-plane must also be univalent. This can be enforced when performing numerical calculations by ensuring the singularities outside the η unit circle do not come into contact with the unit circle. Noting that on ∂D_p, $\bar{\eta} = \eta^{-1}$,

$$\psi_\zeta = \begin{cases} -\omega_0 \left(\dfrac{\bar{\zeta}(\bar{\eta})}{1+\zeta(\eta)\bar{\zeta}(\bar{\eta})} - \dfrac{S(\eta)}{1+\zeta(\eta)S(\eta)} \right), & |\eta| \leq 1 \\ 0, & |\eta| > 1 \end{cases} \tag{3.36}$$

becomes

$$\psi_\zeta = \begin{cases} -\omega_0 \left(\dfrac{\bar{\zeta}(\bar{\eta})}{1+\zeta(\eta)\bar{\zeta}(\bar{\eta})} - \dfrac{\zeta(1/\eta)}{1+\zeta(\eta)\zeta(1/\eta)} \right), & |\eta| \leq 1 \\ 0, & |\eta| > 1. \end{cases} \tag{3.37}$$

ψ_ζ has singularities within the $|\eta| = 1$ disc associated with the terms from the function $S_{sph}(\eta)$. Firstly consider the points where $S_{sph}(\eta)$ is singular. These can occur where $S(\eta)$ is singular or where

$$1 + \zeta(\eta)S(\eta) = 0. \tag{3.38}$$

Given that

$$\begin{aligned} S(\eta) &= R\left(\frac{1}{\eta} + \frac{b\eta^{-1}}{\eta^{-N} - a^N}\right) \\ &= R\left(\frac{1}{\eta} + \frac{b\eta^{N-1}}{1 - \eta^N a^N}\right), \end{aligned} \tag{3.39}$$

the singularities in $S(\eta)$ occur at $\eta = 0$ and $\eta = 1/a$. However, $S_{sph}(\eta)$ is not singular at $\eta = 1/a$, as the denominator has the same singularity. The pole at $\eta = 0$ corresponds to the central line vortex, which maps to $\zeta = 0$, corresponding to the south pole of the sphere, and those in $1 + \zeta(\eta)S(\eta)$ correspond to satellite vortices. The equation (3.38) is equivalent to the quadratic equation for η^N:

$$c_2(a,b,R,N)\eta^{2N} + c_1(a,b,R,N)\eta^N + c_0(a,b,R,N) = 0, \tag{3.40}$$

where

$$\begin{aligned} c_2(a,b,R,N) &= R^2(b - a^N) - a^N \\ c_1(a,b,R,N) &= 1 + a^{2N} + R^2 + R^2(b - a^N)^2 \\ c_0(a,b,R,N) &= R^2(b - a^N) - a^N. \end{aligned} \tag{3.41}$$

The equation is quadratic in η^N, so solutions will be evenly spread around the origin.

Note that as $R \to 0$, the planar solutions are retrieved, $\eta_n = w^n \eta_c$, where $\eta_c = 1/a$ and $w = e^{2\pi i/N}$. This is to be expected, as $R \to 0$ corresponds to the patch area approaching zero, hence the local curvature also tends to zero, and the surface is locally planar. Note that this implies R now has some dimensional significance. On the plane, the area of the patch is effectively irrelevant, as it could be factored out by altering ω, as no length scale was enforced on the distribution. Altering the patch area, then, was indistinguishable after a rescaling of the vorticity. On the sphere, however, the surface area is finite, due to the curvature of the sphere, and so a length scale is enforced. Hence the patch area takes on a physical significance, so R must also.

3.5.2 Stationarity of central line vortex

Suppose η to be near 0. Then

$$\zeta(\eta) \sim \eta R \left(1 - \frac{b}{a^N}\right) + O(\eta^2) \tag{3.42}$$

and

$$\zeta(\frac{1}{\eta}) \sim \frac{R}{\eta} + O(\eta^2). \tag{3.43}$$

Hence it can be seen that

$$\zeta(\eta)\zeta(\eta^{-1}) \sim R^2 \left(1 - \frac{b}{a^N}\right) + O(\eta^2). \tag{3.44}$$

Expanding $\dfrac{S(\eta)}{1+\zeta(\eta)S(\eta)}$ we obtain

$$S_{sph}(\eta) \sim \frac{R}{\eta}\left\{\frac{1}{1+R^2(1-b/a^N)}\right\} + O(\eta^2), \tag{3.45}$$

while

$$\frac{\bar{\zeta}(\bar{\eta})}{1+\zeta(\eta)\bar{\zeta}(\bar{\eta})} = 0 \tag{3.46}$$

as $\eta \to 0$. Hence the central line vortex is stationary.

3.5.3 Stationarity of satellite vortices

The local velocity field must be expanded in Cartesian components on the stereographically projected ζ-plane. Near ζ_s, a satellite point vortex, it is to be expected that

$$\frac{\zeta(\eta^{-1})}{1+\zeta(\eta)\zeta(\eta^{-1})} = \frac{\Gamma}{\zeta-\zeta_s} + \gamma_s + \dots \tag{3.47}$$

for some real coefficients Γ_s and γ_s (u, v) in Cartesian co-ordinates on the ζ-plane is given by,

$$u - iv = \frac{2\omega_0\zeta}{\sin\theta}\left(\frac{\bar{\zeta}}{1+\zeta\bar{\zeta}} - \frac{\Gamma_s}{\zeta-\zeta_s} - \gamma_s + \dots\right) \tag{3.48}$$

$\dfrac{\zeta(\eta^{-1})}{1+\zeta(\eta)\zeta(\eta^{-1})}$ must be expanded and compared with the form in equation (3.47). Set $G(\zeta) = 1+\zeta(\eta)\zeta(\eta^{-1})$. Firstly, note that

$$G(\eta) \sim G'(\zeta_s)(\eta-\eta_s) + \frac{G''(\zeta_s)(\eta-\eta_s)^2}{2} + \dots \tag{3.49}$$

Then

$$\frac{1}{G(\eta)} \sim \frac{1}{G_\eta(\eta_c)(\eta-\eta_c)} - \frac{G_{\eta\eta}(\eta_c)}{2G_\eta^2(\eta_c)} + \dots \tag{3.50}$$

Expanding $\zeta(\eta^{-1})$ using a Taylor series,

$$\zeta(\eta^{-1}) = \zeta(1/\eta_c) - \frac{1}{\eta_c^2}\zeta'(1/\eta_c)(\eta-\eta_c) + \dots \tag{3.51}$$

Combining equation (3.51) and equation (3.50) then

$$\frac{\zeta(1/\eta)}{G(\eta)} = \frac{\zeta(1/\eta_c)}{G_\eta(\eta_c)(\eta-\eta_c)} - \frac{G_{\eta\eta}(\eta_c)\zeta(1/\eta_c)}{2G_\eta^2(\eta_c)} - \frac{\zeta'(1/\eta_c)}{G_\eta(\eta_c)\eta_c^2} + \mathrm{O}(\eta) \tag{3.52}$$

However, an expansion in terms of $\dfrac{1}{\zeta-\zeta_c}$ is required. This is given using the Taylor expansion for ζ near ζ_c:

$$\zeta = \zeta_c + (\eta-\eta_c)\zeta_c' + (\eta-\eta_c)^2\frac{\zeta_c''}{2} + \mathrm{O}((\eta-\eta_c)^3). \tag{3.53}$$

Hence

$$\frac{1}{\eta-\eta_c} = \frac{\zeta_c'}{\zeta-\zeta_c} + \frac{\zeta_c''}{2\zeta'} + \mathrm{O}(\zeta-\zeta_c). \tag{3.54}$$

Therefore the values of Γ_s and γ_s can now be calculated to be

$$\Gamma_s = \frac{\zeta(1/\eta_c)\zeta_c'}{G_\eta(\eta_c)} \tag{3.55}$$

$$\gamma_s = \frac{\zeta(1/\eta_s)}{G_\eta(\eta_s)}\left(\frac{\zeta_{\eta\eta}(\eta_s)}{2\zeta_\eta(\eta_s)} - \frac{G_{\eta\eta}(\eta_s)}{2G_\eta(\eta_s)} - \frac{\zeta_\eta(1/\eta_s)}{\eta_s^2\zeta(1/\eta_s)}\right). \tag{3.56}$$

The stationarity condition requires that the non-self-induced terms of the Cartesian velocity $u - iv$ are zero. Hence the point vortex strengths must be found and subtracted from the total expression. It has been shown in equation (3.28) that the expression for a point vortex on the sphere of strength κ is

$$\psi_p = -\frac{\kappa}{2}\log\left(\frac{(\zeta-\zeta_s)(\bar{\zeta}-\bar{\zeta}_s)}{(1+\zeta\bar{\zeta})(1+\zeta_s\bar{\zeta}_s)}\right). \tag{3.57}$$

This implies that

$$u_p - iv_p = \frac{2\zeta}{\sin\theta}\psi_{p\zeta} = -\frac{2\zeta}{\sin\theta}\frac{\kappa}{2}\left(\frac{1}{\zeta-\zeta_s} - \frac{\bar{\zeta}}{1+\zeta\bar{\zeta}}\right). \tag{3.58}$$

Comparing this with equation (3.48), the point vortex at ζ_s has strength

$$\kappa_s = -2\omega_0\Gamma_s. \tag{3.59}$$

The stationarity condition is thus $[(u-iv)-(u_p-iv_p)]_{\zeta_s,\bar{\zeta}_s} = 0$, which is equivalent to the equation

$$\frac{(1-\Gamma_s)\bar{\zeta}_s}{1+\zeta_s\bar{\zeta}_s} - \gamma_s = 0, \tag{3.60}$$

where Γ_s, γ_s and ζ_s are functions of a, b, R and N.

3.6 Properties of the solutions

Properties of the solutions are investigated for each N by varying the point vortex latitude, θ_0 and patch area $\mathcal{A}$. These parameters are chosen because they have a physical meaning, as opposed to a and R, which are not easily interpreted physically. Note that the solutions have become a two parameter family of solutions, compared with the one parameter family on the plane. This is a result of the extra length scale introduced by the finite area of the sphere. These two quantities specify the solution exactly and are related to the parameters a, b and R by a set of equations. Firstly, the solutions must indeed have point vortices at the required latitude, i.e. $\zeta_s(\eta_s) = \cot(\theta_0/2)$, where η_s is the value obtained by solving (3.40). The solution must also be stationary, which is enforced by (3.60). The third equation requires the area to be fixed, and is derived in Appendix A.

$$\begin{aligned} \zeta_s(\eta_s) &= \cot(\theta_0/2) \\ \frac{(1-\Gamma_s)\bar{\zeta}_s}{1+\zeta_s\bar{\zeta}_s} - \gamma_s &= 0 \\ N\Gamma_S + \Gamma_0 &= 4\pi\mathcal{A} \end{aligned} \tag{3.61}$$

where, as before,

$$\Gamma_s = \frac{\zeta(1/\eta_s)\zeta_\eta(\eta_s)}{G_\eta(\eta_s)}$$

$$\Gamma_c = \frac{R^2(1-ba^{-N})}{1+R^2(1-ba^{-N})}.$$

Solutions to these equations may then be plotted on the sphere, using the equations

$$\begin{aligned} \theta_0 &= 2\cot^{-1}(|\zeta(\eta)|) \\ \phi &= \arg(\zeta(\eta)) \end{aligned} \tag{3.62}$$

for $|\eta| = 1$. This produces boundary points in spherical polar coordinates, and then the equations

$$\begin{aligned} x &= \sin\theta\cos\phi \\ y &= \sin\theta\sin\phi \\ z &= \cos\theta \end{aligned} \tag{3.63}$$

are used to convert to Cartesian coordinates. This is also performed with satellite vortex positions, and then plotted on a sphere using MATLAB.

3.7 Solution Regions

Exact solutions of this form are found for $N \geq 2$. The parameter N fixes the number of satellite line vortices. Hence solutions are found for tripolar and greater multipole distributions. For fixed θ_0 and N, increasing a corresponds to increasing area. We thus plot area rather than a as a has no physical significance.

The total strength of the patch vortex is also defined, as $\Gamma_p = \omega_0\mathcal{A}$, where $\mathcal{A}$ is area.

For the following calculations, we use $\omega_0 = 1$ and renormalise the point vortex strength with respect to Γ_p. For each N, solutions exist as $\mathcal{A} \to 4\pi$, corresponding to $a \to \infty$. This corresponds to the sphere being completely covered by patch vorticity, with a superposed configuration of line vortices. In [19] Morikawa and Swenson consider the stability of a ring of point vortices equally spaced around a central line vortex on the plane. Recalling that on the sphere, patch vorticity is integral to point vortices, it becomes apparent that the limiting case $\mathcal{A} \to 4\pi$ is the equivalent of the planar Morikawa and Swenson distribution. The problem then has no patch boundary, and hence reduces to a point vortex problem. In [5], this point vortex problem is considered. The configuration rotates in general. Values of $\Gamma_0 = \Gamma_0^*(\theta)$ and $\Gamma_s = \Gamma_s^*(\theta)$, can be chosen such that the configuration is stationary however. This must correspond to the limit of the spherical multipolar case. This provides a useful check on the numerics of the multipolar case.

On the plane, for high a the patch boundary is essentially circular. As $a \to 1$, the patch becomes more lobed and eventually cusps, hence the solutions break down. This provides some intuition abut the behaviour of the patch on the sphere. For fixed θ_0, the area $\mathcal{A}$ varies monotonically with a. For large a, the patch covers the entire sphere, occupying an area of 4π. We might expect that as a decreases, and hence the patch area decreases from 4π, a small circular region of irrotational flow will appear at the north pole of the sphere. As $\mathcal{A}$ decreases further, this region will become more distorted until the boundary becomes cusped, and the solutions are no longer admissible. Also, as $\theta_0 \to \pi$ and $\mathcal{A} \to 0$, $R \to 0$ the vortex structure will occupy only a small region around the south pole of the sphere, and be locally planar. The distribution will therefore be qualitatively identical to the planar solution. It can be seen from Fig. 3.2 that in the point vortex problem for high θ_0, the central line vortex and the satellite vortices are of the same, positive strength as the uniform background vorticity. As the satellites move further up the sphere, the strength of the central point vortex becomes negative, passing through zero as it does so. The zero of Γ_c occurs when the satellite point vortices are distributed around the equator.

For high $\mathcal{A}$, the multipolar solutions must be expected to behave similarly. Figures (3.3) and (3.4) show $\dfrac{\Gamma_c}{\Gamma_p}$ and $\dfrac{\Gamma_s}{\Gamma_p}$ against $\mathcal{A}$, the patch area for various choices of θ_0. These quantities are important in the dynamics of the problem because they measure the point vortex strength relative to the background vorticity.

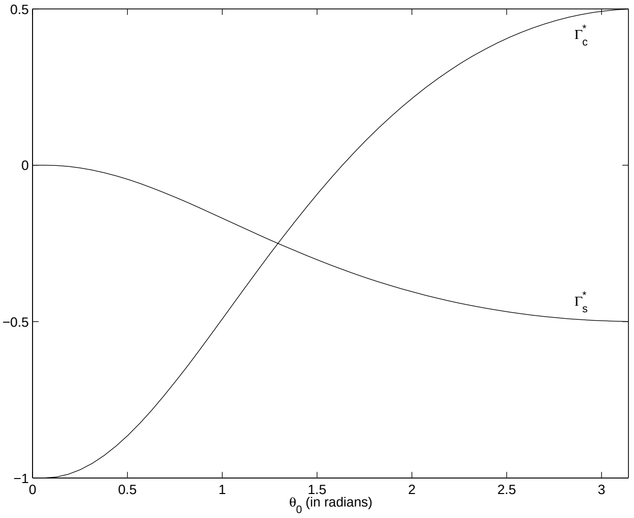

Fig. 3.2: Point vortex arrays - Γ_c^* and Γ_s^* against latitudinal angle θ (in radians) for stationary point vortex arrays on the sphere, with $N = 3$. The graphs intersect at $\theta_0 = \theta_0^{crit} = 70.5^o$ (to 3 significant figures).

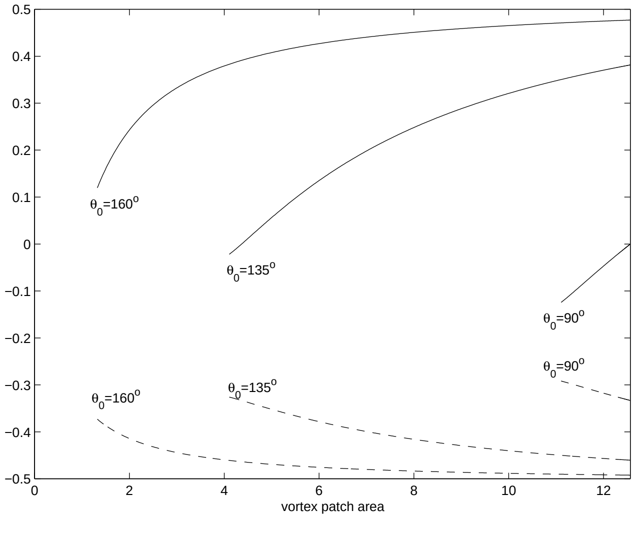

Fig. 3.3: Full multipolar solutions - Renormalized point vortex strengths $\frac{\Gamma_c}{\Gamma_p}$ (solid lines) and $\frac{\Gamma_s}{\Gamma_p}$ (dashed lines) against vortex patch area for $N = 3$ and $\theta_0 = 160^o,\ 135^o$ and 90^o. The values at patch area equal to 4π correspond to those given in Figure 3.2 for the point vortex arrays.

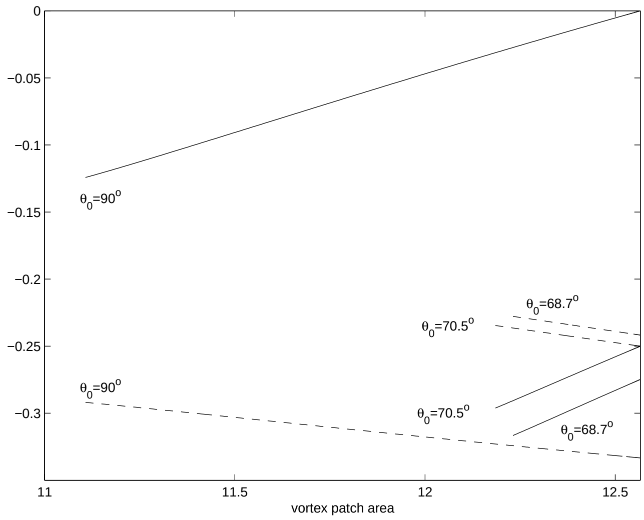

Fig. 3.4: Full multipolar solutions - Renormalized point vortex strengths $\frac{\Gamma_c}{\Gamma_p}$ (solid lines) and $\frac{\Gamma_s}{\Gamma_p}$ (dashed lines) against vortex patch area for $N = 3$ and $\theta_0 = 90^o, 70.5^o (= \theta_0^{crit})$ and 68.7^o. The values at patch area equal to 4π correspond to those given in Figure 2.

3.7.1 Critical a

For any given θ_0, there exists some a_{crit} and hence $\mathcal{A}_{crit}$ below which it is not possible to find solutions. Tending to this value, the patch boundary becomes cusped, as in the planar case. The neighbourhood of the cuspidal points is of course locally planar, so this is in agreement with the analysis of [16], who showed that in limiting V-states on the plane, any points of non-analyticity must be either right-angled corners or cusps.

Near these a_{crit}, with $\theta_0 \approx \pi$ the graphs (3.3) and (3.4) are qualitatively similar to the planar case. This is to be expected, as the structure is extremely close to the south pole, and hence nearly planar. However, as θ_0 increases and the satellite point vortices move towards the north pole, there is a point at which the quantity $\dfrac{\Gamma_c}{\Gamma_p}$ changes from positive to negative. At $\theta_0 = \theta_{crit} = 70.5^o$, the value of $\dfrac{\Gamma_c}{\Gamma_p}$ equals $\dfrac{\Gamma_s}{\Gamma_p}$ when the patch area is close to 4π, so all the point vortices have the same strength. This latitude represents the point where the central point vortex matches the satellite point vortices in cancelling the patch vorticity. Fig. 3.5 shows a set of solutions, in both orthographic and stereographic projections, with $\theta = 160^o$ and varying patch area. The areas range from $\mathcal{A} = 0.868$, which is close to the

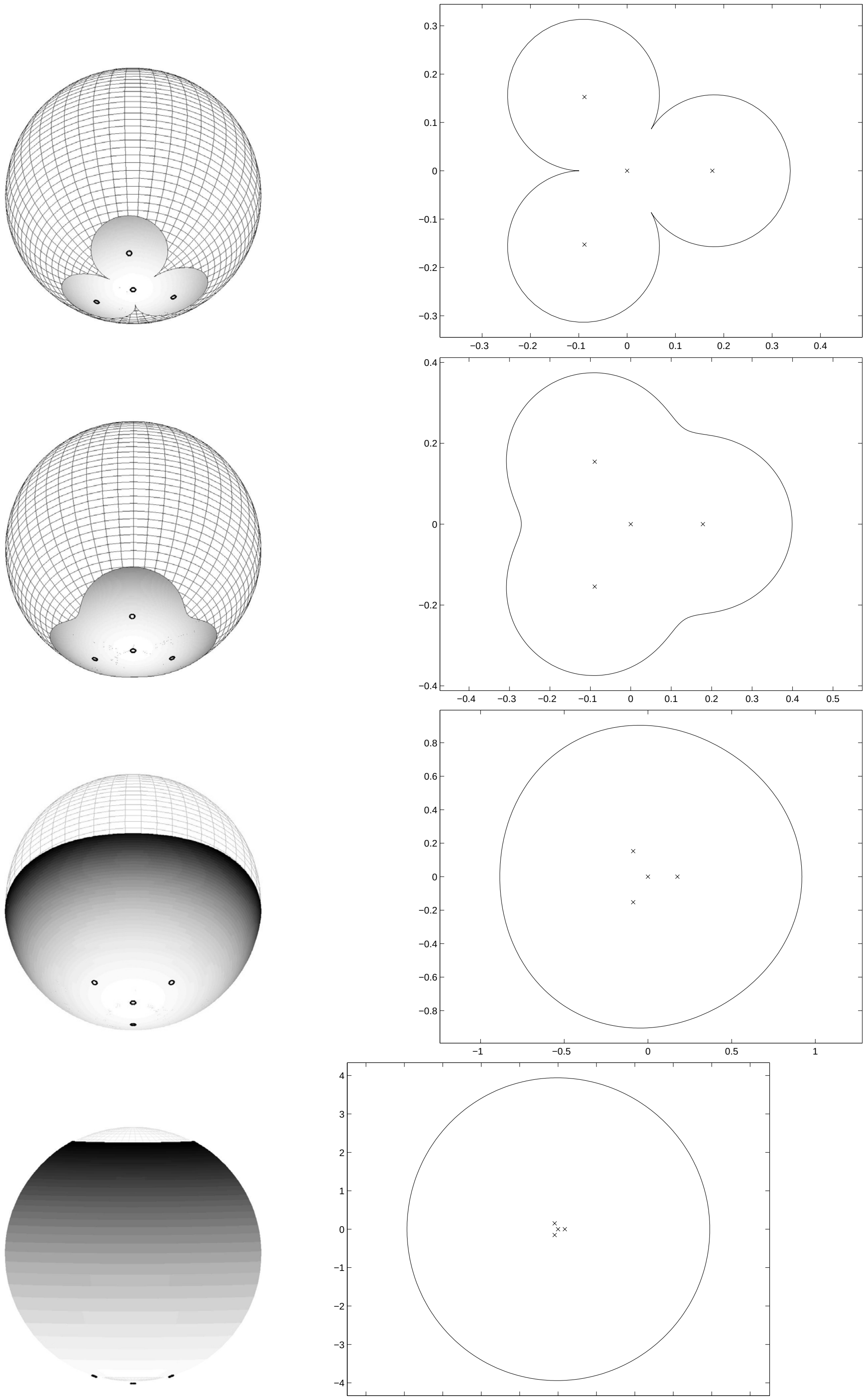

Fig. 3.5: Multipolar vortices with $N = 3$ satellites at latitude $\theta_0 = 160^o$ for different vortex patch areas $\mathcal{A} = 0.868$ (close to cusped configuration), 1.322, 5.640 and 11.805 (close to point-vortex case). Each solution is shown in orthographic projection on the left and in stereographic projection on the right. The corresponding point vortex strengths (Γ_c, Γ_s) are given respectively by $(0.001, 0.022)$, $(-0.013, 0.039)$, $(-0.189, 0.213)$ and $(-0.445, 0.462)$.

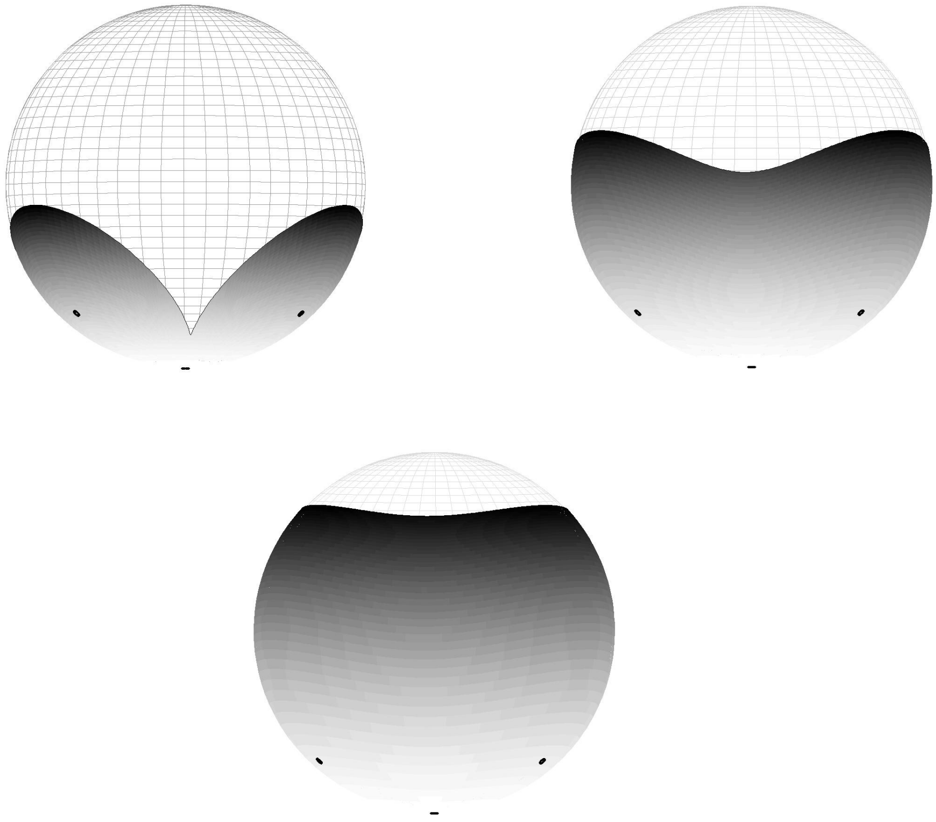

Fig. 3.6: Orthographic projection of multipolar vortices with $N = 3$ satellites at latitude $\theta_0 = 135^o$ for different vortex patch areas $\mathcal{A} = 4.106$, 7.476 and 10.544 (correct to 3 decimal places). The corresponding point vortex strengths (Γ_c, Γ_s) are given respectively by $(0.007, 0.107)$, $(-0.133, 0.243)$ and $(-0.281, 0.373)$.

limiting area, to $\mathcal{A} = 11.805$, where the patch covers almost the entire sphere, which corresponds to the point vortex case.

Fig. 3.6 shows $N = 3$, $\theta_0 = 135^o$ and Fig.3.7 shows $N = 3$, $\theta_0 = 90^o$. Figure 3.8 shows the tripolar $N = 2$ solutions, with $\theta_0 = 160^o$, while Fig. 3.9 shows the quadrupolar $N = 4$ solutions.

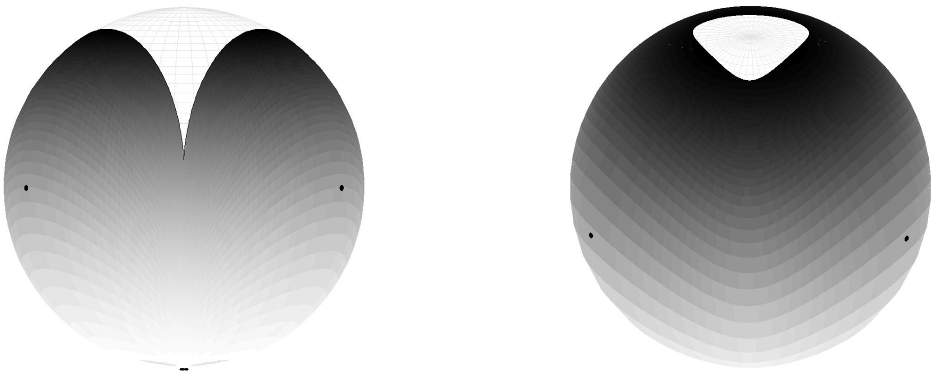

Fig. 3.7: Orthographic projection of multipolar vortices with $N = 3$ satellites at latitude $\theta_0 = 90^o$ for different vortex patch areas $\mathcal{A} = 11.107$ and 12.271. The corresponding point vortex strengths (Γ_c, Γ_s) are given respectively by $(0.110, 0.258)$ and $(0.024, 0.318)$.

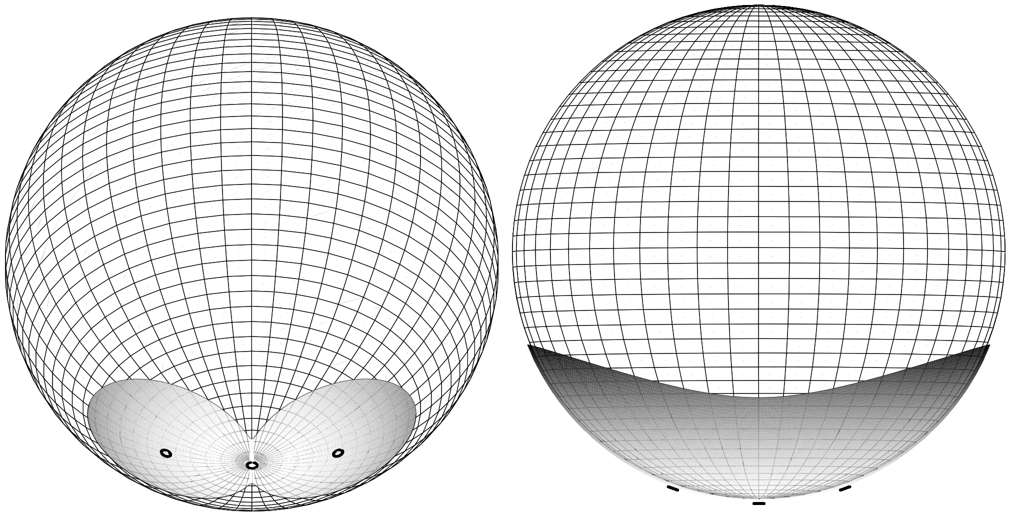

Fig. 3.8: Orthographic projection of multipolar vortices with $N = 2$ satellites at latitude $\theta_0 = 160^o$ for vortex patch areas $\mathcal{A} = 0.846, 3.272$ and 11.007. The corresponding point vortex strengths (Γ_c, Γ_s) are given respectively by $(-0.001, 0.034)$, $(-0.056, 0.159)$ and $(-0.275, 0.575)$.

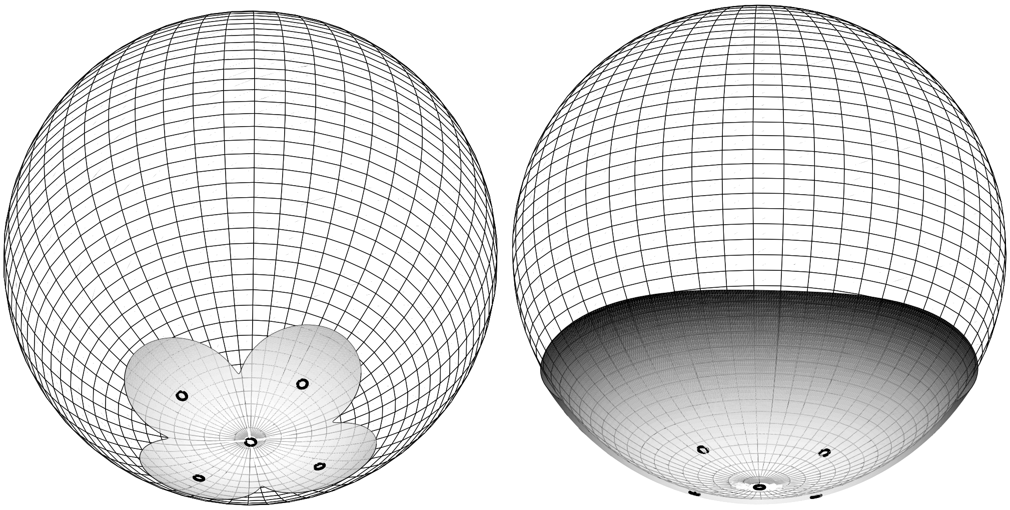

Fig. 3.9: Orthographic projection of multipolar vortices with $N = 4$ satellites at latitude $\theta_0 = 160^o$ for vortex patch areas $\mathcal{A} = 0.838$ and 3.239. The corresponding point vortex strengths (Γ_c, Γ_s) are given respectively by $(0.003, 0.016)$ and $(-0.111, 0.092)$.

CHAPTER 4

Linear stability analysis on the surface of a sphere

We wish to examine the linear stability of the multipolar solutions from Chapter 3. Before doing so, the stability of limits of these solutions will be examined, with the aim of providing checks for the stability of the full multipolar solutions. There are two limits which are of interest, namely the limit in which the multipole behaves as an array of point vortices and the limit in which the multipole behaves as a shielded Rankine vortex. The point vortex limit is expected to be reached as the area of the sphere which is covered by the patch tends to 4π. Here, the patch boundary is sufficiently distant, and the region in which $\omega = 0$ is sufficiently small that we can assume constant background vorticity on the sphere. In this case, we are examining the spherical analogue of the Morikawa and Swenson model on the plane, with angular velocity $\Omega = 0$ (see Fig. 4.1). As θ_0, the colatitude of the ring of vortices, decreases from $\theta_0 = \pi$, curvature effects play a part in the stability behaviour. Similarly, in the case where the patch boundary is sufficiently far from the point vortices and the point vortices are close enough together, we can assume the Multipolar solutions approximate the shielded Rankine vortex. This assumes the point vortices appear to the boundary as one single point vortex, shielded by the southern vortex patch. The stability of this distribution will also be examined.

We may also expect some parameter regimes where multipolar solutions have the boundary behaving as the boundary of a shielded Rankine vortex, and the point vortices behaving like vortices in constant background vorticity, as in the Morikawa and Swenson solutions.

The stability of the full multipolar equilibria will then be examined. The methodology of §2.5 will be adopted, although the actual equations of motion will contain

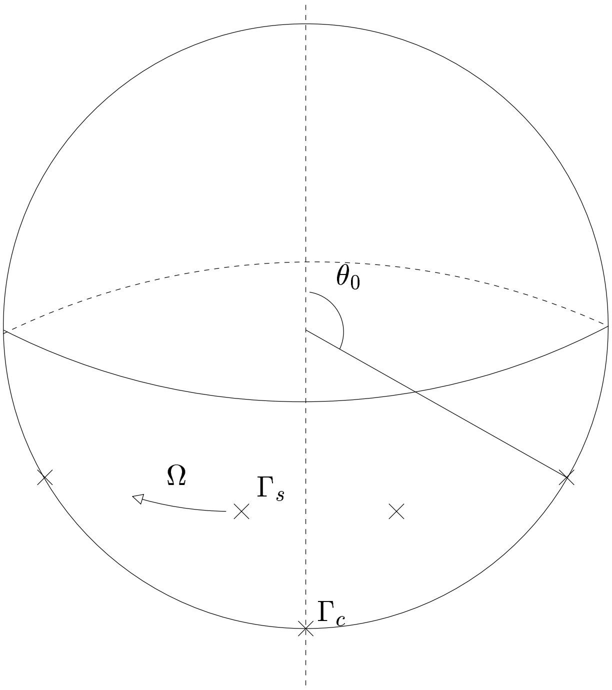

Fig. 4.1: Diagram of Morikawa and Swenson distribution on the surface of a sphere. The crosses mark vortex positions

curvature terms in the spherical case. Results of the stability analysis will be expected to match the limits detailed above. In addition, the eigenmodes obtained will be expected to display similar general properties to those in §2.6, namely a limited number of modes with non-zero area perturbation, and no modes of non-zero angular momentum perturbation.

4.1 Generalisation of the results of Morikawa and Swenson to a sphere

4.1.1 Background

The motion of point vortices has long been used as a model of geophysical and oceanographical phenomena. In 1883, J. J. Thompson presented his work on the stability of a ring of N point vortices of strength Γ, corotating with angular velocity Ω [32]. Thompson showed that, independent of Γ this configuration is linearly stable

Table 4.1: Range of linear stability, with $\Gamma_s = 1$, from [19]

N	Lower stability limit (Γ_0)	Upper stability limit(Γ_0)
2	$-\infty$	-1.25
3	$-\infty$	1
4	-0.5	2.25
5	-0.5	4
6	-0.25	6.25
7	0	9
8	0.5	12.25
9	1	16

for $N < 7$, neutrally stable for $N = 7$ and unstable for $N > 7$.

Almost a hundred years later, in 1970, Morikawa and Swenson considered the linear stability of the case with an added central line vortex [19]. They showed that the linear stability is dependant on the ratio of the central line vortex strength to the satellite vortex strength. Fixing (without loss of generality) the circulation of the satellite line vortices to unity, Table 4.1 of stability regions is obtained. Note the case $\Gamma_0 = 0$ corresponds to the Thompson case, and falls in the stable regions for $n = 2, 3, 4, 5, 6$, on the stability boundary for $n = 7$ and outside for $n = 8$.

D. G. Dritschel has examined the stability of similarly distributed configurations of finite area patches of vorticity [33]. The results of this were compared with the results of [32] and [19], and it was shown that provided the patches are sufficiently separated, the results corroborate. If the patches are closer together, however, they prove less stable than the point vortex model, the mechanism of instability being derived from boundary deformation.

By applying the results of chapter 3, it is relatively straight forward to generalise the results of Morikawa and Swenson to the sphere. Indeed, Thompson's work has already been generalised to the sphere by Polvani and Dritschel [28]. Table 4.2 summarizes their results. The non-linear stability of this case has been investigated by Boatto and Cabral [34]. It was found in [34] that the region of non-linear stability for this problem coincides with the region of linear stability, except on the equator, where their method breaks down.

The linear stability of the generalisation of the Morikawa and Swenson case on the

Table 4.2: Stability ranges, between which a vortex ring on a non-rotating sphere becomes linearly unstable, from [28]

N	Unstable θ_0 range, in degrees	Unstable θ_0 range, in radians
2		Always stable
3		Always stable
4	$(54.736, 125.2640)$	$(0.9553, 2.1863)$
5	$(45, 135)$	$(\pi/4, 3\pi/4)$
6	$(26.506, 153.4340)$	$(0.4637, 2.6779)$
7	$(0, 180)$	$(0, pi)$
> 7		Always unstable

sphere has not previously been considered however. The equations of linear stability are derived below, and solved numerically to give the stability regions in terms of the ratio Γ_s/Γ_c, the circulations of the satellite vortices and central vortex, and angle of colatitude θ_0 of the satellite vortices.

As $\theta_0 \to 0$, the ring of vortices will become closer together. This will then appear to the central line vortex as a single line vortex, with strength $\sum_{j=1}^{N} \Gamma_j$. Clearly on a non-rotating sphere, any pair of vortices for which a joining line must pass through the centre of the sphere induce no velocity in each other. To see this, consider point vortices on the equator at $\zeta = \pm 1$. This configuration gives a velocity field in polar coordinates of

$$u - iv = -\frac{\zeta\Gamma_+}{2\pi\sin\theta_0}\left(\frac{1}{\zeta-1} - \frac{\bar{\zeta}}{1+\zeta\bar{\zeta}}\right) - \frac{\zeta\Gamma_-}{2\pi\sin\theta_0}\left(\frac{1}{\zeta+1} - \frac{\bar{\zeta}}{1+\zeta\bar{\zeta}}\right). \tag{4.1}$$

Evaluating at the two line vortices , we find that the non-self-induced velocity is zero. The sphere is non-rotating, so this result holds for any pair placed diametrically opposite each other. Hence the point vortex problem decouples into the stability of an isolated vortex at the south pole and an isolated ring of N corotating vortices at the north pole. As an isolated vortex is trivially stable, the stability in this limit will be identical to that of the Thompson ring on the plane.

As $\theta_0 \to 0$, it is to be expected that the stability region of this distribution will be identical to those of Thompson. Also, for $\Gamma_0 = 0$, the results of Polvani and Dritschel [28] must be retrieved. Similarly, as $\theta_0 \to \pi$, the stability results should become the same as those of Morikawa and Swenson.

4.2 Formulation of the problem

4.2.1 Base state

From §3.3, the stream function for a ring of N point vortices with colatitude θ_0 with circulation Γ_s arranged around a point vortex at the south pole of circulation Γ_c is given by

$$\psi = -\frac{\Gamma_s}{4\pi}\sum_{j=1}^{N}\log\left(\frac{2(\zeta-\zeta_j(t))(\bar{\zeta}-\bar{\zeta}_j(t))}{(1+\zeta\bar{\zeta})(1+\zeta_j\bar{\zeta}_j)}\right)-\frac{\Gamma_c}{4\pi}\log\left(\frac{2(\zeta-\zeta_c(t))(\bar{\zeta}-\bar{\zeta}_c(t))}{(1+\zeta\bar{\zeta})(1+\zeta_c\bar{\zeta}_c)}\right). \tag{4.2}$$

The positions of the pre-images of vortices on the complex plane shall be denoted $\zeta_k(t)$ for the vortices arranged in a ring. These will be referred to as the satellite vortices, and will co-rotate at constant colatitude with a constant angular velocity Ω. The position of the central line vortex in the complex plane will be denoted $\zeta_c(t)$.

Hence the derivative is given by

$$\psi_\zeta = -\frac{\Gamma_s}{4\pi}\sum_{j=1}^{N}\left(\frac{1}{\zeta-\zeta_j(t)}-\frac{\bar{\zeta}}{1+\zeta\bar{\zeta}}\right)-\frac{\Gamma_c}{4\pi}\left(\frac{1}{\zeta}-\frac{\bar{\zeta}}{1+\zeta\bar{\zeta}}\right), \tag{4.3}$$

where $\zeta_j = r\lambda^j$, $r=\cot(\theta_0/2)$ and $\lambda = e^{2\pi i/N}$. We wish to move to the co-rotating frame, and hence must find the angular velocity of the structure. From (3.16)

$$u_\phi - iu_\theta = \frac{2\zeta}{\sin\theta}\psi_\zeta, \tag{4.4}$$

then

$$u_\phi - iu_\theta = -\frac{\zeta\Gamma_s}{2\pi\sin\theta}\sum_{j=1}^{N}\left(\frac{1}{\zeta-\zeta_j}-\frac{\bar{\zeta}}{1+\zeta\bar{\zeta}}\right)-\frac{\zeta\Gamma_c}{2\pi\sin\theta}\left(\frac{1}{\zeta}-\frac{\bar{\zeta}}{1+\zeta\bar{\zeta}}\right). \tag{4.5}$$

Consider the angular velocity of the satellite point vortex on the real axis. Hence evaluating the non-self induced part of (4.5) at $\zeta = r$ yields

$$u_\phi - iu_\theta = -\frac{r\Gamma_s}{2\pi\sin\theta_0}\sum_{j=1}^{N-1}\left(\frac{1}{r-r\omega^j}-\frac{r}{1+r^2}\right)-\frac{r\Gamma_c}{2\pi\sin\theta_0}\left(\frac{1}{r}-\frac{r}{1+r^2}\right). \tag{4.6}$$

Since $\sum_{j=1}^{N-1} \dfrac{1}{1-\lambda^j} = (N-1)/2$, it can be seen that

$$
\begin{aligned}
u_\phi - iu_\theta &= \frac{\Gamma_s (N-1)\cos\theta_0}{4\pi\sin\theta_0} - \frac{\Gamma_c}{2\pi\sin\theta_0}\frac{1}{1+r^2} && (4.7)\\
&= \frac{\Gamma_s (N-1)\cos\theta_0}{4\pi\sin\theta_0} - \frac{\Gamma_c}{2\pi\sin\theta_0}\sin^2(\theta_0/2). && (4.8)
\end{aligned}
$$

The RHS is purely real, and hence $u_\theta = 0$. The angular velocity is given by $\Omega = u_\phi/\sin\theta_0$, hence

$$
\Omega = \frac{\Gamma_s (N-1)\cos\theta_0}{4\pi\sin^2\theta_0} - \frac{\Gamma_c}{4\pi\sin^2\theta_0}(1-\cos\theta_0). \tag{4.9}
$$

We now need to find an expression for solid body rotation with angular velocity Ω on the sphere. If the whole sphere is solid body rotation with angular velocity Ω, the component of velocity u_θ will be equal to zero.

$$
\frac{u_\phi}{\sin\theta} = \Omega. \tag{4.10}
$$

Aplying to (3.16), we obtain

$$
\frac{u_\phi}{\sin\theta} = \frac{2\zeta\psi_\zeta}{\sin^2\theta} = \Omega. \tag{4.11}
$$

Hence,

$$
\begin{aligned}
\psi_\zeta &= \frac{\Omega}{2\zeta}\sin^2\theta\\
&= \Omega\frac{2\bar{\zeta}}{(1+\zeta\bar{\zeta})^2}
\end{aligned} \tag{4.12}
$$

is the required expression for solid body rotation on a sphere.

Then considering again the vortex array (4.3) and transforming to the frame corotating with the ring of vortices, ψ_ζ in Cartesian coordinates on the projected ζ-plane is given by

$$
\psi_\zeta = -\frac{\Gamma_s}{4\pi}\sum_{j=1}^{N}\left(\frac{1}{\zeta-\zeta_j(t)} - \frac{\bar{\zeta}}{1+\zeta\bar{\zeta}}\right) - \frac{\Gamma_c}{4\pi}\left(\frac{1}{\zeta} - \frac{\bar{\zeta}}{1+\zeta\bar{\zeta}}\right) - \frac{2\Omega\bar{\zeta}}{(1+\zeta\bar{\zeta})^2}. \tag{4.13}
$$

The velocity field is then given by

$$
\begin{aligned}
u - iv = \frac{i\Gamma_s}{8\pi}(1+\zeta\bar{\zeta})^2\sum_{j=1}^{N}\left(\frac{1}{\zeta-\zeta_j(t)} - \frac{\bar{\zeta}}{1+\zeta\bar{\zeta}}\right) + \frac{i\Gamma_c}{8\pi}(1+\zeta\bar{\zeta})^2\left(\frac{1}{\zeta} - \frac{\bar{\zeta}}{1+\zeta\bar{\zeta}}\right) +\\
(1+\zeta\bar{\zeta})^2\frac{i\Omega\bar{\zeta}}{(1+\zeta\bar{\zeta})^2}.
\end{aligned} \tag{4.14}
$$

4.2.2 Linear Stability

We proceed to analyse the linear stability on the sphere, following broadly the methods used in §2.5. The base state distribution of the line vortices ζ_k in the co-rotating frame is perturbed with form $\zeta_k = \zeta_{0k} + \epsilon f(t)$, where ζ_{0k} is the unperturbed position on the k-th line vortex, and $\epsilon f(t)$ is some (infinitesimal) perturbation to this position. $f(t)$ is taken to be in the form $f(t) = \hat{\zeta}_k e^{\sigma t}$. Applying the non-self-induction hypothesis, the differential equation

$$\frac{d\bar{\zeta}_k}{dt} = U - iV|_{\zeta_k} \tag{4.15}$$

is obtained. Here, $U - iV|_{\zeta_k}$ is the non-self-induced velocity field at the location of the point vortex ζ_k, while $\dfrac{d\bar{\zeta}_k}{dt}$ is the velocity of the point vortex ζ_k. The non-self-induced velocity for a vortex with pre-image ζ_l on the ζ-plane is given by

$$U - iV = (u - iv) - \frac{i\Gamma_l}{8\pi}(1 + \zeta\bar{\zeta})^2 \left(\frac{1}{\zeta - \zeta_l} - \frac{\bar{\zeta}_l}{1 + \zeta_l \bar{\zeta}_l} \right), \tag{4.16}$$

where Γ_l is the strength of the point vortex.

Substituting equation (4.14) into (4.15), and then expanding to order ϵ provides the following equation for motion of the satellite vortices:

$$\begin{aligned}
\sigma\hat{\bar{\zeta}}_k =& \frac{i\kappa_s}{4} \sum_{j=1, j\neq k}^{N} \left\{ \hat{\zeta}_j \left[\frac{(1 + \zeta_{k0}\bar{\zeta}_{k0})^2}{(\zeta_{k0} - \zeta_{j0})^2} \right] + \hat{\zeta}_k \left[\bar{\zeta}_{k0}^2 - \frac{(1 + \zeta_{k0}\bar{\zeta}_{k0})^2}{(\zeta_{k0} - \zeta_{j0})^2} + \right.\right. \\
& \left. 2\bar{\zeta}_{k0}(1 + \zeta_{k0}\bar{\zeta}_{k0})(\frac{1}{\zeta_{k0} - \zeta_{j0}} - \frac{\bar{\zeta}_{0k}(\zeta_{0j} - \zeta_{k0})}{(\zeta_{0j} - \zeta_{0k})(1 + \zeta_{k0}\bar{\zeta}_{k0})}) \right] \\
& + \hat{\bar{\zeta}}_k \left[\zeta_{k0}\bar{\zeta}_{k0} - (1 + \zeta_{k0}\bar{\zeta}_{k0}) + 2\zeta_{k0}(1 + \zeta_{k0}\bar{\zeta}_{k0})(\frac{1}{\zeta_{k0} - \zeta_{j0}} - \right. \\
& \left.\left. \frac{\bar{\zeta}_{0k}(\zeta_{0j} - \zeta_{k0})}{(\zeta_{0j} - \zeta_{0k})(1 + \zeta_{k0}\bar{\zeta}_{k0})}) \right] \right\} + \frac{i\kappa_c}{4} \left[\hat{\zeta}_0 \left(\frac{(1 + \zeta_{k0}\bar{\zeta}_{k0})^2}{\zeta_{k0}^2} \right) + \right. \\
& \hat{\zeta}_k \left(\bar{\zeta}_{k0}^2 - \frac{(1 + \zeta_{k0}\bar{\zeta}_{k0})^2}{\zeta_{k0}^2} + 2(1 + \zeta_{k0}\bar{\zeta}_{k0})\frac{\bar{\zeta}_{k0}}{\zeta_{k0}} - 2\bar{\zeta}_{k0}^2 \right) \\
& \left. + \hat{\bar{\zeta}}_k \left(-\zeta_{k0}\bar{\zeta}_{k0} + (1 + \zeta_{k0}\bar{\zeta}_{k0}) \right) \right] - i\Omega\hat{\bar{\zeta}}_k.
\end{aligned} \tag{4.17}$$

Similarly, the central line vortex motion must satisfy the equation:

$$\sigma\hat{\hat{\zeta}}_c = -\frac{i}{2}\left(-2\Omega\hat{\zeta}_c + \frac{\kappa_s}{2}\sum_{j=1}^{N}(\hat{\hat{\zeta}}_c + \frac{\hat{\zeta}_c - \hat{\zeta}_j}{\zeta_{j0}^2})\right). \tag{4.18}$$

4.2.3 Numerical Method and Results

This linear stability problem is solved numerically by considering the set of unknowns

$$\left\{\hat{\zeta}_k | k = 0...N\right\}, \left\{\hat{\hat{\zeta}}_k | k = 0...N\right\}.$$

Putting

$$\mathbf{x} = \left\{ \begin{array}{cccccccccc} \hat{\zeta}_0 & \hat{\zeta}_1 & ... & \hat{\zeta}_{N-1} & \hat{\zeta}_N & \hat{\hat{\zeta}}_0 & \hat{\hat{\zeta}}_1 & ... & \hat{\hat{\zeta}}_{N-1} & \hat{\hat{\zeta}}_N \end{array} \right\}' \tag{4.19}$$

We hence have an eigenvalue problem,

$$\sigma\mathbf{x} = \mathbf{A}\mathbf{x}.$$

Suppose the eigenvalues are $\{\sigma_k; k = 1\ldots 2N+2\}$. Then the vortex array is linearly stable if $\max(\Re[\sigma_k]) < 0$. However, as for the planar case, our system is Hamiltonian, so the eigenvalues occur in quartets symmetric about the real and complex axis. Hence we require that all the real parts are identically zero for stability. A MATLAB code was written to numerically calculate the matrix **A**, and determine the stability of these structures.

4.2.4 Results

Results are presented for $n = 2, 3, \ldots, 8$. Before commenting on specific results, the following general observations should be noted. Firstly, as $\theta_0 \to \pi$, and hence the vortex distribution becomes locally planar, the stability regions are identical to the planar Morikawa and Swenson results (see Table 4.1 and [19]). Whether the most unstable line vortex is the central line vortex or satellite line vortices is found to correspond with the Morikawa and Swenson results, for all n and Γ_c/Γ_s. Morikawa and Swenson found that for regions of instability in the Γ_c/Γ_s plane above the stable region, the central line vortex is the mechanism of instability. For unstable regions below the region of stability, satellite vortices (called circle vortices in [19]) are the instability mechanism. Secondly, as $\theta_0 \to 0$, the structure is stable for $n = 2...6$, $n = 7$ is on the border of stability and all $n > 7$ are unstable. Hence the planar results of Thompson are recovered, again as expected. Thirdly, the distributions for which $\Gamma_0 = 0$ are equivalent to a ring of vortices with no central vortex, the same as Thompson's distribution on the sphere, as examined by Polvani and Dritschel in [28]. The case Γ_0 is clearly dynamically identical to the Polvani and Dritschel case. However, there is a "tracer" present at the position of the central point vortex. As the behaviour of this tracer is included in the stability code, there is no *a priori* basis for assuming that the stability for Γ_0 should be the same as Polvani and Dritschel, or indeed for the stability obtained to be symmetric about the equator. Any break in symmetry would of course be expected to be associated with the central line vortex tracer, as there will be no dynamical effect on the satellite vortices. In practice, the only case with stability results differing from [28] is $n = 2$, which is found to be stable by Polvani and Dritschel, but unstable for various θ_0 here. The instability is indeed in the central line vortex mode. As the degree of symmetry increases, $n > 3$, the $\Gamma_c = 0$ results exactly correspond to that of Polvani and Dritschel.

For each n, a contour plot of the maximum real part of λ_k, with Γ_c/Γ_s against the angle θ_0. The dashed line indicates the values in the $\{\theta_0, \Gamma_c/\Gamma_s\}$ plane for which $\Omega = 0$, i.e. the vortex ring is not rotating. This is shown for comparison with the stability of the multipolar vortices on a sphere, which will be examined in §4.4. These structures are non-rotating, and in the limit where the patch area tends to 4π, the multipole will approach the Morikawa and Swenson distribution. In addition, the stability for $\Gamma_0 = 0$ is shown, which corresponds to no central line vortex in the distribution.

We consider the stability behaviour for three distinct cases: $n = 2, 3$, $n = 4, 5, 6$, $n = 7, 8$.

Fig. 4.2: Contour plot of maximum real part of eigenvalues for $n = 2$. Shaded region is unstable.

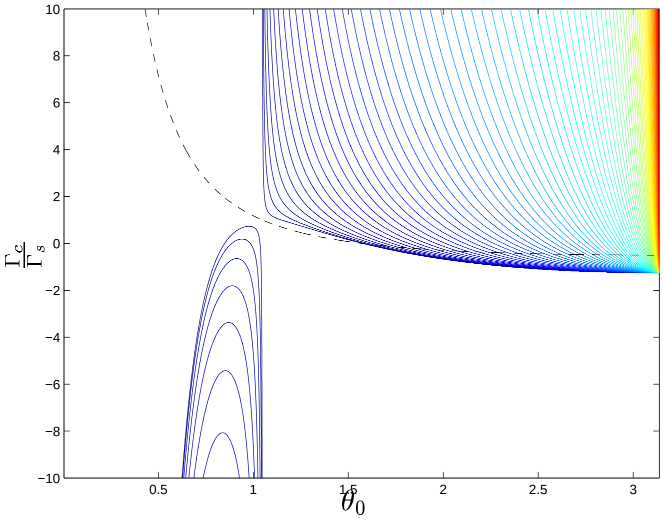

Stability of $n = 2$ and $n = 3$

Figures 4.2 and 4.4 show contour plots of the largest real part of the eigenvalues of the $n = 2$ and $n = 3$ equilibria. The $(\Gamma_c/\Gamma_s, \theta_0)$-plane contains two regions of instability. One exists with $\Gamma_c/\Gamma_s > 0$ and θ_0 above $\theta_0 \approx 2$, for $n = 3$, $\theta_0 > 1.2$ for $n = 2$. For $n = 2$, plots are shown of along the solutions with $\Gamma_c = 0$ and $\Omega = 0$ (Fig. 4.3). These plots are not shown for $n = 3$ as they are identically zero. For θ_0 above $\theta_0 \approx 2$ the central line vortex is unstable and this region maintains approximately the same upper and lower stability boundaries as the planar point vortex model. The other region is in $\Gamma_c/\Gamma_s < 0$. This is also unstable due to central line vortex effects. Note that for $n = 3$, $\Gamma_c = 0$, the case with no central line vortex, the results correspond exactly to the findings of [28]. Specifically, the distribution is stable.

Stability of $n = 4$, $n = 5$ and $n = 6$

The cases $n = 4, 5, 6$ have qualitatively different stability behaviour from the lower n. The contour plots are presented in Figs. 4.5, 4.7 and 4.9. Plots along $\Gamma_c = 0$ and $\Omega = 0$ are shown in Figs. 4.6, 4.8 and 4.10. There is also a progressive alteration of stability behaviour as n increases through this set. There is an area of satellite vortex instability which for $n = 4$ occupies mainly the area with $\Gamma_c/\Gamma_s < 0$, crossing

Fig. 4.3: Maximum unstable eigenvalues along the $\Omega = 0$ curve (left hand plot) and the $\Gamma_c = 0$ curve (right hand plot), for $n = 2$.

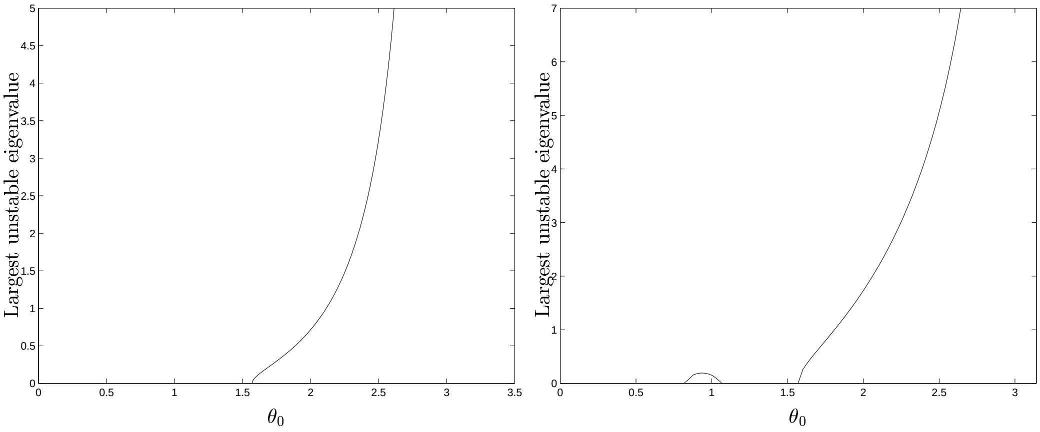

Fig. 4.4: Contour plots of maximum real part of eigenvalues for $n = 3$. Shaded region is unstable.

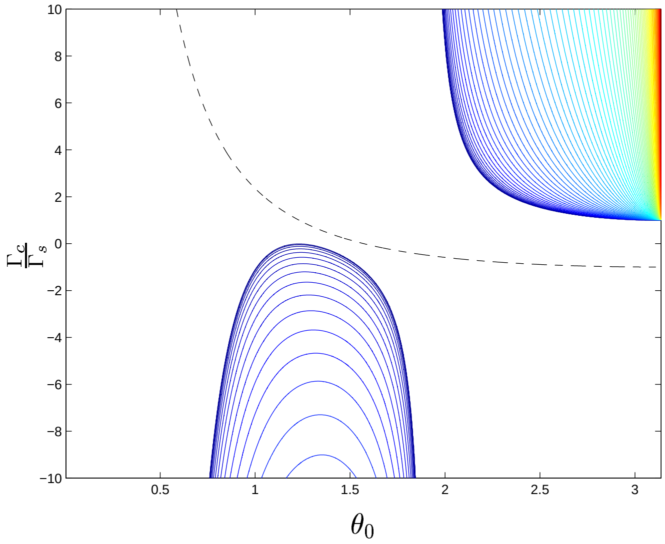

Fig. 4.5: Contour plots of maximum real part of eigenvalues for $n = 4$. Shaded region is unstable.

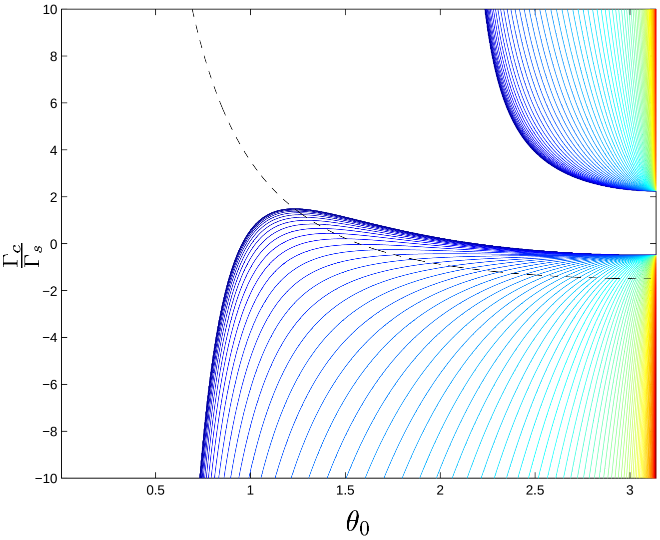

into the region $\Gamma_c/\Gamma_s > 0$ for some θ_0 values. For $n = 5$, $n = 6$, this region extends, superposing further over $\Gamma_c/\Gamma_s > 0$. In addition, for $\Gamma_c/\Gamma_s > 0$, θ_0 above $\theta_0 \approx 2$, of central line vortex instability. Note that for $\theta_0 \to \pi$, for all values of n, in the θ_c/θ_s plane there is a lower region of instability caused by satellite vortex instability and a higher region of central line vortex instability, as observed in [19]. It is instructive to compare the stability with that of the distribution with no central line vortex, $\Gamma_c = 0$. As $\theta_0 \to 0$, the distribution mimics the stability of the planar Thompson distribution, due the equations decoupling. For $\Gamma_c/\Gamma_s < 0$, i.e. different sign circulations of satellite and central point vortices, the vortex distribution is largely unstable for θ_0 greater than some value dependant on n. For $\Gamma_c/\Gamma_s > 0$, the distribution is generally stable, except for the high θ_0 central line vortex instabilities, and possibly some satellite vortex instabilities. Uniformly, though, if the central line vortex is of opposite sign to the ring of vortices, it is a destabilising influence, whereas for $\Gamma_c/\Gamma_s > 0$, it is a stabilising influence. However, as n increases. the magnitude of Γ_c needed to enforce this stability increases. For example, with $n = 6$, as θ_0 decreases from $\theta_0 = \pi$ to $\theta_0 = 0.5$, an increasingly positive Γ_c/Γ_s is required to enforce this stability, due to the effect of the central line vortex being shielded by the curvature of the sphere.

Fig. 4.6: Maximum unstable eigenvalues along the $\Omega = 0$ curve (left hand plot) and the $\Gamma_c = 0$ curve (right hand plot), for $n = 4$.

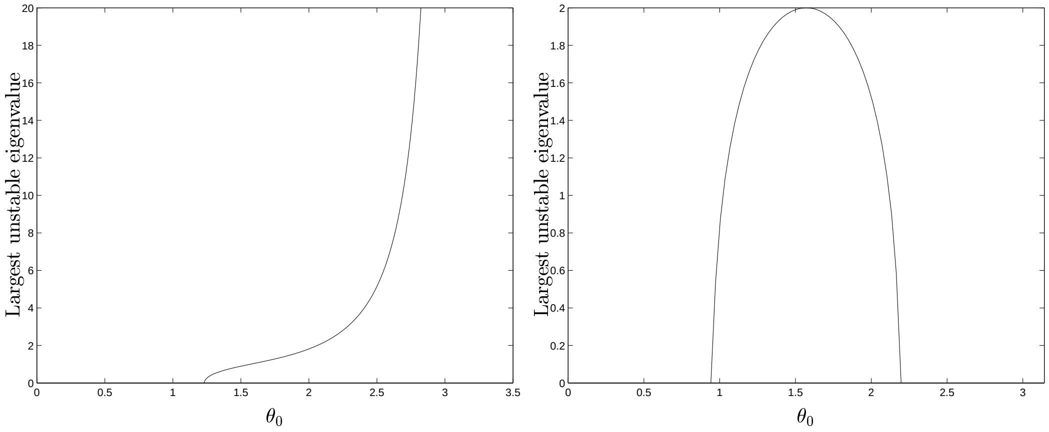

Fig. 4.7: Contour plots of maximum real part of eigenvalues for $n = 5$. Shaded region is unstable.

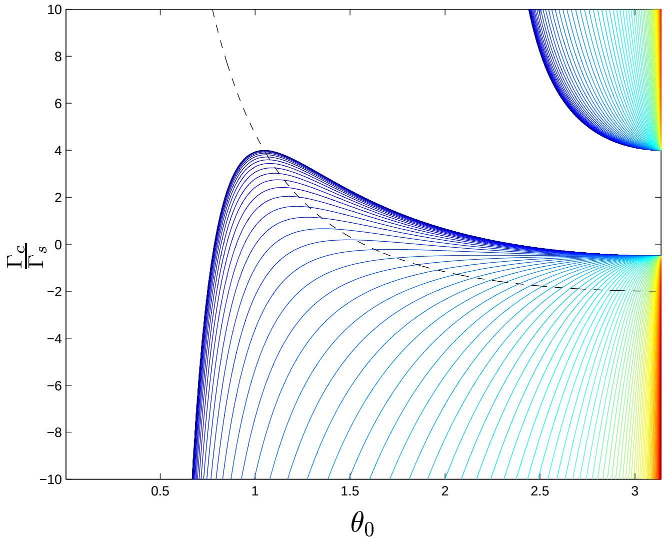

Fig. 4.8: Maximum eigenvalues along the $\Omega = 0$ curve (left hand plot) and the $\Gamma_c = 0$ curve (right hand plot), for $n = 5$.

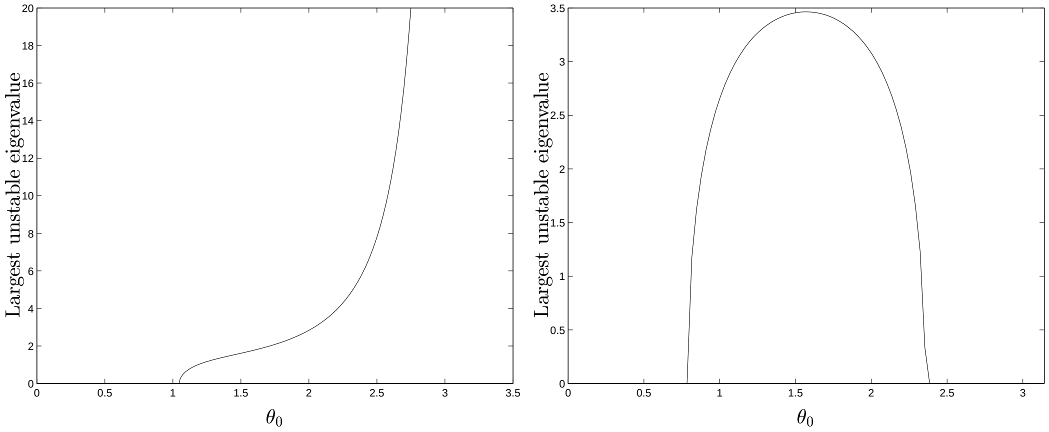

Fig. 4.9: Contour plots of maximum real part of eigenvalues for $n = 6$. Shaded region is unstable.

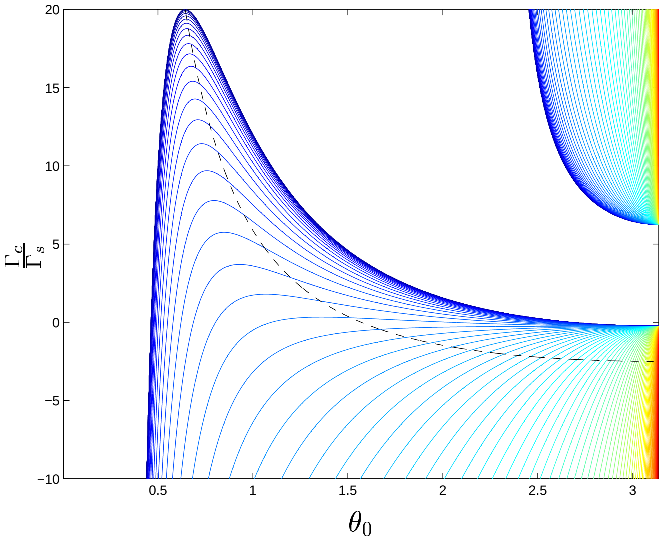

Fig. 4.10: Maximum eigenvalues along the $\Omega = 0$ curve (left hand plot) and the $\Gamma_c = 0$ curve (right hand plot), for $n = 6$.

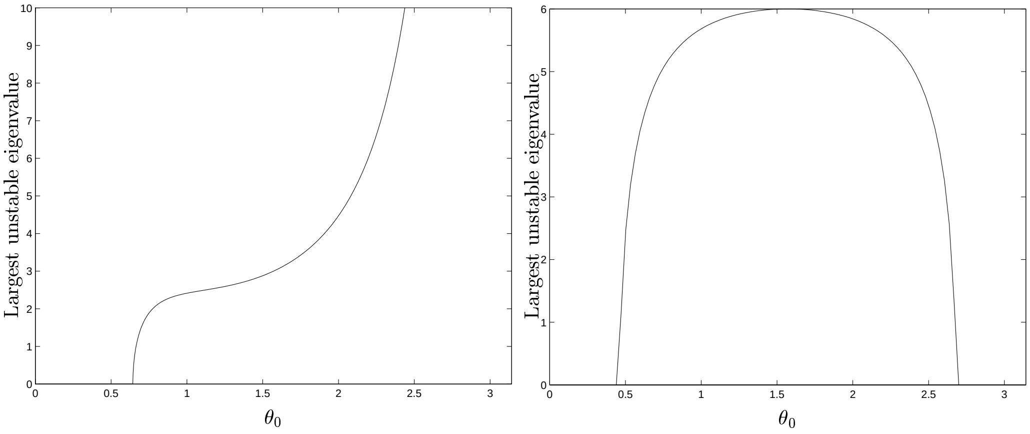

Fig. 4.11: Contour plots of maximum real part of eigenvalues for $n = 7$

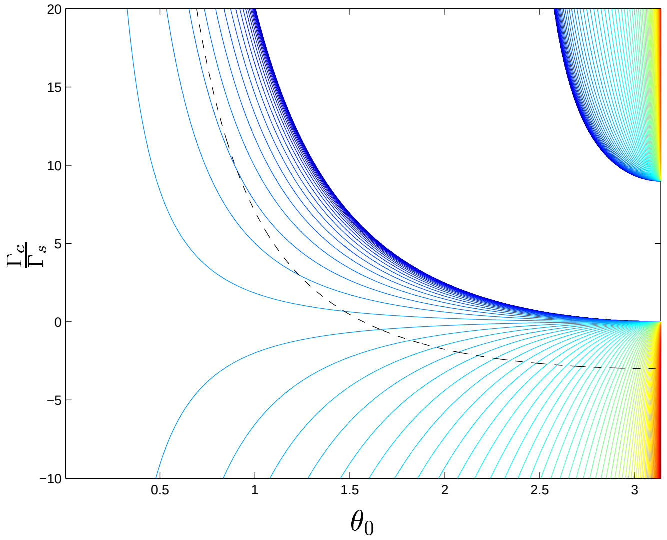

Stability of $n \geq 7$

Contour plot are shown for $n = 7$ and $n = 8$ in Fig. 4.11 and Fig. 4.14, and are indicative of results with higher n. For these n values, the stability behaviour is dominated by the satellite line vortex instability, which, as $\theta_0 \to 0$ covers all values of Γ_c/Γ_s. This is to be expected, as in the region $\theta_0 \to 0$, the equations decouple to a isolated point vortex and a ring of point vortices near the north pole of the sphere. As, for $n \geq 7$, this is unstable the stabilising effect of the central line vortex only affects the stability of the vortex ring for high Γ_c/Γ_s. For $\Gamma_c/\Gamma_s > 0$, as $\theta_0 \to \pi$, there is still a region of central line vortex instability. As with the other n values, as $\theta_0 \to \pi$, the unstable values of Γ_c/Γ_s above the stable region manifest central line vortex instabilities while Γ_c/Γ_s below the stable region exhibit satellite vortex instabilities. The Γ_c case is unstable, but for all colatitudes except $\theta_0 = 0$, can be stabilised for sufficiently positive Γ_c/Γ_s. As $\theta_0 \to 0$, Γ_c/Γ_s must become extremely large for stability to be achieved.

General remarks

The most interesting region of this stability analysis occurs for non-extreme values of θ_0. The $\theta_0 \to 0$ and $\theta_0 \to \pi$ values correspond to planar results, whereas non-extreme values show the effect of curvature on the stability. For example, for $n \geq 7$,

Fig. 4.12: Maximum eigenvalues along the $\Omega = 0$ curve (left hand plot), for $n = 7$.

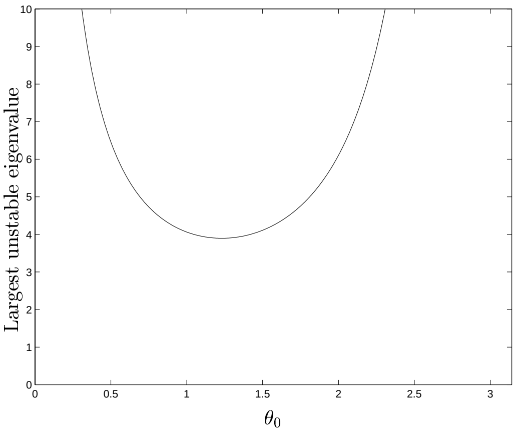

Fig. 4.13: Contour plots of maximum real part of eigenvalues for $n = 8$

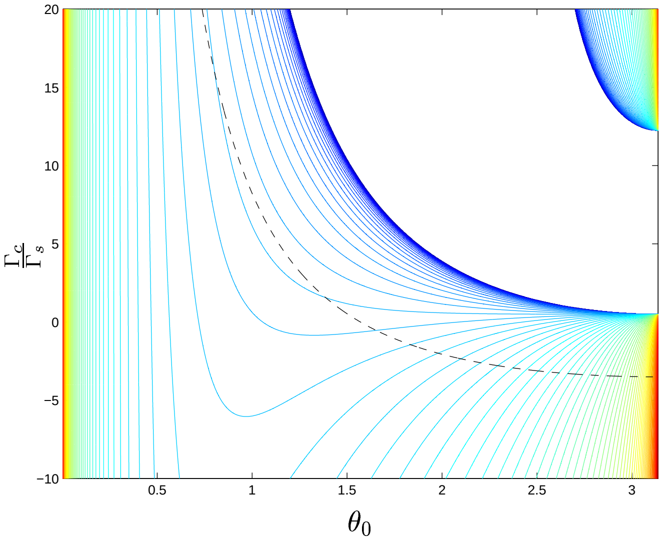

Fig. 4.14: Maximum eigenvalues along the $\Omega = 0$ curve (left hand plot) and the $\Gamma_c = 0$ curve (right hand plot), for $n = 8$.

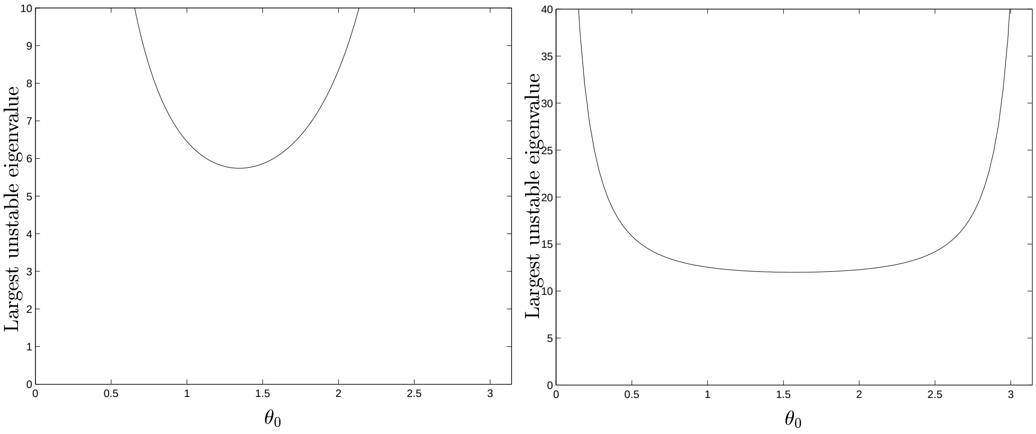

the satellite ring with no central line vortex is unstable for all θ_0. For stability of the Morikawa and Swenson type case, the central line vortex must stabilise the satellite ring, without being unstable itself. It can be seen from Fig. 4.11 and Fig. 4.14 that as θ_0 decreases from π, the strength of the central line vortex which enforces stationarity increases. This is explicable physically, as the curvature of the sphere is "shielding" the satellite vortices from the stabilising effect of the central line vortex. Hence, for stability to be enforced as the curvature effects increase, the circulation of the central line vortex must increase,

Compared to the planar Morikawa and Swenson distribution, the spherical $n = 4, 5, 6$ cases show that the central line vortex is more stable as the ring of satellite vortices moves up the sphere. In this case, the curvature of the surface is a stabilising effect. The satellite ring is found to be unstable for Γ_c/Γ_s less than some value $\chi(\theta_0)$, a function of θ_0. This value $\chi(\theta_0)$ is equal or greater than the planar value $\chi(\pi)$, until some value $\theta^*(n)$. For $\theta_0 < \theta^*(n)$ $\chi(\theta_0)$ decreases rapidly. $\theta^*(n)$ is found to be close to the value at which the Thompson ring becomes stable. Hence as the satellite ring tends towards the north pole, the stabilising effects of the central line vortex become shielded. So the central line vortex must be increasingly powerful to stabilise a ring which is intrinsically unstable. If the ring is intrinsically stable, however, the stabilising effect of the central line vortex is irrelevant, and all values of $\frac{\Gamma_c}{\Gamma_s}$ are stable.

With the lower symmetry of $n = 2$, $n = 3$, it is found that when near the equator, the satellite ring causes an instability in the central line vortex.

4.3 Linear stability of a shielded Rankine vortex on the sphere

4.3.1 Introduction

Considering again the full multipolar results, we are interested in the limit in which the patch boundary is far from the point vortices, which are themselves close to-

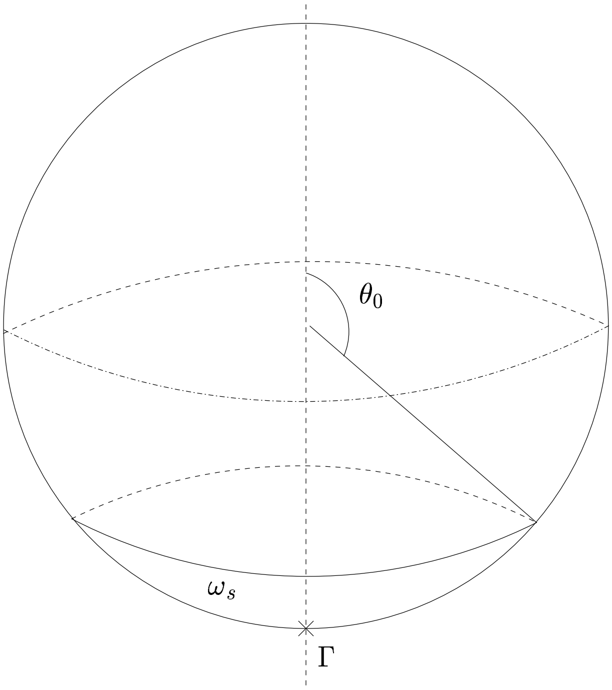

Fig. 4.15: Diagram of shielded Rankine vortex on the surface of a sphere. The region beneath the angle θ_0 is a patch of vorticity with strength ω_s, around a line vortex with circulation Γ at the south pole.

gether. If the patch boundary is close to circular, then the boundary and point vortices might be expected to interact as if the array of point vortices were replaced with a single point vortex of strength $\sum_{j=1}^{N} \Gamma_j$. In this case, we expect that modelling a single point vortex embedded in a patch of uniform vorticity will be instructive.

This is limit is clearly the spherical equivalent of a shielded Rankine vortex. We shall model a patch of constant vorticity ω_s on the sphere in which a line vortex of strength Γ is embedded at the south pole. This patch shall extend to a colatitude θ_0, above which the fluid shall be irrotational (see Fig. 4.3.1). The stability of this structure has not previously been investigated, and hence the next section will present its linear stability.

4.3.2 Formulation

Consider the vortex distribution given by

$$\psi_\zeta = \begin{cases} \dfrac{\gamma}{\zeta} + \dfrac{\omega_s \bar{\zeta}}{1+\zeta\bar{\zeta}}, & \zeta \in D \\ \\ \dfrac{A}{\zeta}, & \zeta \notin D, \end{cases} \tag{4.20}$$

on the complex plane, where $D = \{\zeta(\eta); |\eta| < 1\}$, $\zeta(\eta) = R\eta$ and $R = \cot(\theta_0/2)$. We are here introducing a map which takes a unit circle in the η-plane to some circular domain in the ζ-plane. The ζ-plane is then itself mapped on to the surface of the sphere using a stereographic projection. A is to be chosen so the velocity field is continuous, and hence pressure is continuous. From (3.17),

$$u - iv = -\frac{i}{2}(1+\zeta\bar{\zeta})^2 \psi_\zeta \tag{4.21}$$

provides the velocity field, so for this distribution,

$$u - iv = \begin{cases} -\dfrac{i}{2}(1+\zeta\bar{\zeta})^2 \left\{ \dfrac{\gamma}{\zeta} + \dfrac{\omega_s \bar{\zeta}}{1+\zeta\bar{\zeta}} \right\}, & \zeta \in D, \\ \\ -\dfrac{i}{2}(1+\zeta\bar{\zeta})^2 \left\{ \dfrac{A}{\zeta} \right\}, & \zeta \notin D. \end{cases} \tag{4.22}$$

Equivalent to (4.20) is the expression for vorticity

$$\omega = \begin{cases} \gamma\delta(\theta - \pi, \psi) + \omega_S, & \theta < \theta_0, \\ 0, & \theta > \theta_0. \end{cases} \tag{4.23}$$

Recalling that the integral of vorticity over the surface of the sphere must equal zero, then

$$\int_{\phi=0}^{2\pi} \int_{\theta=\pi}^{\theta_0} (\gamma\delta(\theta, \phi, \theta', \phi') + \omega_S) \sin\theta \mathrm{d}\theta \mathrm{d}\phi = 0. \tag{4.24}$$

Hence

$$\gamma = -\omega_S(\cos\theta_0 + 1). \tag{4.25}$$

This can be expressed in terms of the quantity $R = \cot(\theta_0/2)$ as

$$\gamma = -\frac{\omega_S R^2}{1+R^2}. \tag{4.26}$$

Applying continuity of (4.22),

$$\begin{aligned} A &= \frac{\omega_S R^2}{1+R^2}+\gamma \\ &= \frac{\omega_S R^2}{1+R^2}-\frac{\omega_S R^2}{1+R^2} \\ &= 0. \end{aligned} \tag{4.27}$$

Hence the flow on the northern region of the sphere is identically zero, and the base velocity field is given by

$$u-iv=\begin{cases} -\frac{i}{2}(1+\zeta\bar{\zeta})^2\left\{\frac{\gamma}{\zeta}+\frac{\omega_s\bar{\zeta}}{1+\zeta\bar{\zeta}}\right\}, & \zeta\in D \\ \\ 0, & \zeta\notin D, \end{cases} \tag{4.28}$$

We wish to examine the behaviour of this distribution under infinitesimal perturbations.

4.3.3 Linear stability

The equilibrium (4.28) is more complex than the Morikawa and Swenson type point vortex model (4.14), as it consists of a patch of constant vorticity as well as a point vortex. While the equations for motion of point vortices can be written as a finite system of O.D.E.s, the motion of the patch is specified by its boundary [13]. This requires am infinite dimensional system of equations and possibly the solution of a Riemann-Hilbert problem. However, as with the planar shielded Rankine vortex, the Plemelj equations will not be required to solve the Riemann-Hilbert problem, as the geometry is quite straightforward. Hence we follow the methodology of §2.5, with respect to point vortex to patch boundary interactions. We aim again to obtain a eigenvalue problem, $\mathbf{Ax}=\sigma\mathbf{x}$. Specifically we perturb the central point vortex position on the complex plane from its base state value of ζ_{c0} to the point $\zeta_c=\zeta_{c0}+\epsilon\hat{\zeta}_c(t)$. The base state conformal map from the η-plane to the ζ-plane will be perturbed from $\zeta_0(\eta)=R\eta$ to $\zeta(\eta)=\zeta_0(\eta)+\epsilon\hat{\zeta}(\eta,t)$, where $\hat{\zeta}(\eta,t)=\sum_{n=1}^{\infty}\hat{a}_n e^{\sigma_n t}\eta^n$. The patch boundary, $\partial D=\{\zeta(\eta);|\eta|<1\}$ is hence also perturbed. Note that due to the simple geometry of this case, we expect the modes of $\hat{\zeta}(\eta,t)$ to decouple, as in the planar case §2.4.1. Hence we try the ansatz $\hat{\zeta}(\eta,t) = a_n e^{\sigma_n t}\eta^n$, for $n \in \mathcal{N}$. Continuity of pressure must be enforced across the boundary, which will be achieved by enforcing continuity of velocity. Also both the patch boundary and the central line vortex must move with the local flow. Continuity of velocity will yield a Riemann-Hilbert problem, while the movement of the patch boundary and point vortices will result in a matrix problem, the eigenvalues of which will provide the linear stability.

Riemann-Hilbert problem

We now substitute $\zeta(\eta) = \zeta_0(\eta) + \epsilon\hat{\zeta}(\eta,t)$ into (4.28). As in §2.4.1, Helmholtz's law requires that the circulation of the vortex at ζ_c must remain constant. Then considering ψ_ζ, we obtain

$$\psi_\zeta = \begin{cases} \omega_s \dfrac{\bar{\zeta}_0(1/\eta) + \epsilon\hat{\bar{\zeta}}(\eta,t)}{1 + \zeta_0(\eta)\bar{\zeta}_0(1/\eta) + \zeta_0(\eta)\hat{\bar{\zeta}}(1/\eta,t) + \hat{\zeta}(\eta,t)\bar{\zeta}_0(1/\eta)} + & |\eta| < 1 \\ \qquad \dfrac{\gamma}{\zeta_0(\eta) + \epsilon\hat{\zeta}_c} + \hat{F}(\eta,t), & \\ \hat{G}(\eta,t), & |\eta| > 1. \end{cases} \tag{4.29}$$

Here, $\hat{F}(\zeta(\eta),t)$ and $\hat{G}(\zeta(\eta),t)$ are functions analytic inside and outside the patch respectively. As they are introduced by the perturbation, there are no $\mathcal{O}(1)$ terms.

Equating on the boundary, $\zeta \in \partial D$, to ensure continuity of velocity,

$$\begin{aligned} \hat{F}(\zeta(\eta),t) - \hat{G}(\zeta(\eta),t) = -\omega_s & \frac{\bar{\zeta}_0(1/\eta) + \epsilon\bar{\hat{\zeta}}(1/\eta,t)}{1 + \zeta_0(\eta)\bar{\zeta}_0(1/\eta) + \zeta_0(\eta)\hat{\bar{\zeta}}(1/\eta,t) + \hat{\zeta}(\eta,t)\bar{\zeta}_0(1/\eta)} \\ & - \frac{\gamma}{\zeta_0(\eta) + \epsilon\hat{\zeta}_c(t)}. \end{aligned} \tag{4.30}$$

This is then a Riemann-Hilbert problem. Substituting for ω_s from (4.26) and expanding to $\mathcal{O}(\epsilon)$,

$$\hat{F}(\zeta(\eta),t) - \hat{G}(\zeta(\eta),t) = \frac{\epsilon\gamma e^{t\sigma}\eta^{-n}\hat{\bar{a}}_n}{R^2(1+R^2)} + \frac{\epsilon\gamma e^{t\sigma}\eta^{n-2}\hat{a}_n}{R^2(1+R^2)} - \frac{\epsilon\gamma e^{t\sigma}\hat{\eta}_c}{R^2\eta^2} \tag{4.31}$$

for $|\eta| = 1$. Is it straight forwards in this case to split up the RHS. of (4.31) into parts analytic inside and outside $D = \{\zeta(\eta) : \eta < 1\}$. This gives

$$\hat{F}(\zeta(\eta),t) = \frac{\epsilon\gamma e^{t\sigma}\eta^{n-2}\hat{a}_n}{R^2(1+R^2)} = -\frac{\epsilon\omega_s e^{t\sigma}\eta^{n-2}\hat{a}_n}{(1+R^2)^2} \tag{4.32}$$

$$\hat{G}(\zeta(\eta),t) = \frac{\epsilon\gamma e^{t\sigma}\eta^{-n}\hat{\bar{a}}_n}{R^2(1+R^2)} - \frac{\epsilon\gamma e^{t\sigma}\hat{\eta}_c}{R^2\eta^2} \tag{4.33}$$

$$= -\frac{\epsilon\omega_s e^{t\sigma}\eta^{-n}\hat{\bar{a}}_n}{(1+R^2)^2} + \frac{\epsilon\omega_s e^{t\sigma}\hat{\eta}_c}{(1+R^2)\eta^2}. \tag{4.34}$$

4.3.4 Kinematic Conditions

We require that the boundary moves with the local flow. The kinematic boundary condition is therefore given by

$$\mathbf{Re}\left[\hat{\bar{\zeta}}_t\eta\zeta_\eta\right] = \mathbf{Re}\left[(u-iv)\zeta_\eta\eta\right], \tag{4.35}$$

on $\zeta \in \partial D$.

Then using (3.17),

$$\hat{u} - i\hat{v} = -\frac{i}{2}\left[2(1+R^2)(\zeta_0(\eta)\hat{\bar{\zeta}}(\eta,t) + \bar{\zeta}_0(\eta)\hat{\zeta}(\eta,t))\psi_{0\zeta} + (1+R^2)^2\hat{\psi}_\zeta\right], \tag{4.36}$$

for $\zeta(\eta) \in \partial D$. Either the inner or outer form of ψ_ζ can be used, as they are equal on the boundary. Using the outer form,

$$\psi_{0\zeta} = 0, \tag{4.37}$$

and

$$\begin{aligned}\hat{\psi}_\zeta &= \hat{G}(\zeta(\eta),t) \\ &= \frac{\epsilon\gamma e^{t\sigma}\eta^{-n}\hat{\bar{a}}_n}{R^2(1+R^2)} - \frac{\epsilon\gamma e^{t\sigma}\hat{\eta}_c}{R^2\eta^2}.\end{aligned} \tag{4.38}$$

Then

$$\hat{u} - i\hat{v} = \frac{-i\epsilon e^{t\sigma}(1+R^2)\gamma\eta^{-2-n}(-\eta^2\bar{a}_n + (1+R^2)\eta^n\hat{\eta}_c)}{2R^2} + \mathcal{O}(\epsilon^2) \tag{4.39}$$

on the boundary. Substituting into (4.35) and equating positive and negative powers of η,

$$\sigma\hat{\hat{c}}_n = \begin{cases} \dfrac{i\gamma(1+R^2)}{2R^2}(\hat{\hat{a}}_n - (1+R^2)\hat{\eta}_c), & n = 2, \\ \\ \dfrac{i\gamma(1+R^2)}{2R^2}\hat{\hat{a}}_n, & n > 2. \end{cases} \tag{4.40}$$

In terms of ω_s we can hence write this as

$$\sigma\hat{\hat{c}}_n = \begin{cases} -\dfrac{i\omega_s}{2}(\hat{\hat{a}}_n - (1+R^2)\hat{\eta}_c), & n = 2, \\ \\ -\dfrac{i\omega_s}{2}\hat{\hat{a}}_n, & n > 2. \end{cases} \tag{4.41}$$

4.3.5 Central line vortex motion

Applying the non-self-induction condition to the central line vortex, we obtain the equation

$$\frac{d\bar{\zeta}_c}{dt} = (U - iV)|_{\zeta=\zeta_c}, \tag{4.42}$$

where $U - iV$ in the non-self-induced local velocity. The form of a point vortex on the sphere at point $\zeta = \zeta_l$ with circulation Γ_l is given by

$$u - iv = -\frac{i\Gamma_l}{8\pi}(1+\zeta\bar{\zeta})^2\left(\frac{1}{\zeta-\zeta_l} - \frac{\bar{\zeta}_l}{1+\zeta_l\bar{\zeta}_l}\right). \tag{4.43}$$

Noting that (4.28) has a point vortex of circulation $4\pi\gamma$ at the origin, then

$$\begin{aligned} U - iV &= \left[(u-iv) + \frac{i\gamma}{2}(1+\zeta\bar{\zeta})^2\left(\frac{1}{\zeta-\zeta_c} - \frac{\bar{\zeta}}{1+\zeta\bar{\zeta}}\right)\right]_{\zeta=\hat{\zeta}_c} \\ &= \frac{i\gamma}{2R^2}\hat{\hat{a}}_c - \frac{i}{2}(1+\zeta\bar{\zeta})^2\hat{F}(\zeta(\eta),t)|_{\zeta=\hat{\zeta}_c}. \end{aligned} \tag{4.44}$$

Substituting from (4.32), the relation

$$\sigma\hat{\hat{a}}_c = \begin{cases} \dfrac{i\gamma}{2R^2}\hat{\hat{a}}_c - \dfrac{i}{2}\dfrac{\gamma\hat{a}_2}{R^2(1+R^2)}, & n = 2 \\ \\ \dfrac{i\gamma}{2R^2}\hat{\hat{a}}_c, & n > 2, \end{cases} \tag{4.45}$$

is obtained. In terms of ω_s this gives

$$\sigma\hat{\hat{a}}_c = \begin{cases} -\dfrac{i\omega_s}{2(1+R^2)}\hat{\hat{a}}_c + \dfrac{i}{2}\dfrac{\omega_s \hat{a}_2}{(1+R^2)^2}, & n = 2 \\ \\ -\dfrac{i\omega_s}{2(1+R^2)}\hat{\hat{a}}_c, & n > 2. \end{cases} \tag{4.46}$$

Note that both the equations (4.45) and (4.40) decouple for $n > 2$, so only the elliptic, $n = 2$, modes interact between the boundary and line vortex. This is analogous to the planar case (see (2.63) and (2.61).

Eigenvalue problem

An eigenvalue problem $\mathbf{Ax} = \sigma\mathbf{x}$ can hence be formed. Note that equations (4.40) and (4.45) are seemingly singular as $R \to 0$. However, equation (4.26) shows that $\gamma \to 0$ like R^2 as $R \to 0$, and hence (4.40) and (4.45) are regular for all R. For $n = 2$, the matrix equation is given by,

$$\sigma \begin{pmatrix} \hat{\hat{a}}_n \\ \hat{\zeta}_c \end{pmatrix} = \begin{pmatrix} -\dfrac{i\omega_s}{2} & \dfrac{i\omega_s(1+R^2)}{2} \\ \\ \dfrac{-i\omega_s}{2(1+R^2)^2} & \dfrac{i\omega_s}{2(1+R^2)} \end{pmatrix} \begin{pmatrix} \hat{\hat{a}}_n \\ \hat{\zeta}_c \end{pmatrix} \tag{4.47}$$

and for $n > 2$,

$$\sigma \begin{pmatrix} \hat{\hat{a}}_n \\ \hat{\zeta}_c \end{pmatrix} = \begin{pmatrix} -\dfrac{i\omega_s}{2} & 0 \\ 0 & \dfrac{i\omega_s}{2(1+R^2)} \end{pmatrix} \begin{pmatrix} \hat{\hat{a}}_n \\ \hat{\zeta}_c \end{pmatrix}. \tag{4.48}$$

Hence we obtain the eigenvalues

$$\sigma_n = \begin{cases} \left\{0, \dfrac{-i\omega_s R^2}{2(1+R^2)}\right\}, & n = 2 \\ \\ \left\{-\dfrac{i\omega_s}{2}, \dfrac{i\omega_s}{2(1+R^2)}\right\}, & n > 2. \end{cases} \tag{4.49}$$

The following observations can be made:

1. The eigenvalues have zero real part, and hence the structure is neutrally stable. This is in direct correspondence with the planar case.

2. The n=2 mode has a zero eigenvalue, corresponding to perturbation to a nearby solution with different area.

3. As $R \to 0$, corresponding to the patch of non-zero vorticity shrinking to the south pole, $\gamma \to 0$ for fixed ω_s. The eigenvalue tend to the planar values for the shielded Rankine vortex, as expected, namely, for $n = 2$, repeated eigenvalues are obtained, while for the eigenvalues tend to $\pm i\omega_s/2$.

4. As R increases, the non-zero elliptical mode tends to $-i/2$. One of the higher order modes simultaneously tends to zero, corresponding to a line vortex perturbation implying another bifurcation, in which the line vortex is perturbed. As $R \to \infty$, the patch completely covers the sphere and hence the bifurcation to an altered line vortex position become admissible

4.4 The linear stability of a multipolar vortex on the surface of a sphere

We now proceed to examine the linear stability of the full multipolar solutions on the sphere §3.36. As with the multipolar stability analysis on the plane §2.5, many steps performed analytically for the shielded Rankine vortex and Morikawa and Swenson distributions must now be evaluated numerically.

4.4.1 Base state

From §3.36, we have the base state for a multipolar vortex on the surface of a sphere:

$$\psi(\zeta,\bar{\zeta}) = \begin{cases} -\omega_0 \left(\log(1+\zeta\bar{\zeta}) - \int^{\bar{\zeta}} S_{sph}(\zeta')\mathrm{d}\zeta - \int^{\zeta} \bar{S}_{sph}(\zeta')\mathrm{d}\zeta\right), & \zeta \in D' \\ 0, & \zeta \notin \bar{D}', \end{cases} \tag{4.50}$$

where $D' = \{\zeta(\eta); \eta\bar{\eta} \le 1\}$ and S_{sph} is the spherical modification of the planar Schwarz function, as discussed in §3.4. Differentiating gives us the expression for ψ_ζ

$$\psi_\zeta = \begin{cases} -\omega_0 \left(\dfrac{\bar{\zeta}}{1+\zeta\bar{\zeta}} - S_{sph}(\zeta) \right), & \zeta \in D' \\ 0, & \zeta \notin \bar{D}', \end{cases} \tag{4.51}$$

4.4.2 Stability

We will proceed broadly in the same manner as the planar stability analysis in §2.5, performing the following steps:

1. Rewrite ψ_ζ as

$$\psi_\zeta = \begin{cases} \omega_0 \left(\dfrac{\bar{\zeta}}{(1+\zeta\bar{\zeta})} - \dfrac{\gamma_0}{\zeta-\zeta_0} - \sum_k \dfrac{\gamma_k}{\zeta-\zeta_k} + F(\zeta) \right), & \zeta \in D' \\ \\ 0, & \zeta \notin D', \end{cases} \tag{4.52}$$

   where γ_0 and γ_k are related to the strengths of the line vortices created by $S_{sph}(\zeta)$ by $\gamma_k = \Gamma_k/4\pi\omega_0$, and the Γ_k are given in Chapter 3. $F(\zeta)$ contains the irrotational flow part of $S_{sph}(\zeta)$.

2. Introduce a time dependant perturbation to the conformal map $\zeta(\eta)$, so that $\zeta(\eta) = \zeta_0(\eta) + \epsilon\hat{\zeta}(\eta)$, where $\zeta_0(\eta)$ is the base state conformal map, and $\epsilon\hat{\zeta}(\eta)$ is the perturbation to the conformal map. Write the perturbed line vortex positions as $\zeta_j = \zeta_{j0} + \epsilon\hat{\zeta}_j(t)$, where ζ_{k0} is the unperturbed line vortex position, and $\hat{\zeta}_j(t)$ is the perturbation to the line vortex position, and $\hat{\eta}_j$ to be the pre-image of this perturbation in the η-plane. This perturbation will be taken to preserve the line vortex strengths, and the area of the vortex. However, this will perturb the shape of the boundary and also induce some irrotational flow interior and exterior to the patch. Hence we now write ψ_ζ as

$$\psi_\zeta = \begin{cases} -\omega_0 \left(\dfrac{\bar{\zeta}}{(1+\zeta\bar{\zeta})} - \dfrac{\gamma_0}{\zeta-\zeta_0} - \sum_k \dfrac{\gamma_k}{\zeta-\zeta_k} + F_0(\zeta) + \epsilon\hat{F}(\zeta,t) \right), & \zeta \in D(t) \\ \\ -\omega_0\epsilon\hat{G}(\zeta,t), & \zeta \notin D(t), \end{cases} \tag{4.53}$$

   where $D(t)$ is the domain $D = \{\zeta(\eta); \eta\bar{\eta} \leq 1\}$

3. Apply continuity of velocity across the patch boundary. The Cartesian velocity field on the ζ-plane is given by $u - iv = -\frac{i}{2}(1+\zeta\bar{\zeta})^2\psi_\zeta$, hence continuity of velocity implies continuity of ψ_ζ. We hence form a Riemann-Hilbert problem for $F(\zeta)$ and $G(\zeta)$, which will allow $F(\zeta)$ and $G(\zeta)$ to be expressed in terms of the perturbation coefficients, by applying the Plemelj formulae. The dependence of the perturbed velocity field on the perturbation coefficients is hence known;

4. Substitute the $F(\zeta)$ and $G(\zeta)$ from above into the kinematic boundary condition, and the equations of motion for the line vortices to obtain a generalised eigenvalue problem for the perturbation coefficients and the pre-images of the line vortices.

4.4.3 Numerical method

The numerical method is identical to that employed in §2.5.3.

We express the unknown perturbations to the map as

$$\hat{\zeta}(\eta,t) = e^{\sigma t}\sum_{k=0}^{\infty}\hat{a}_k\eta^k, \qquad \hat{\bar{\zeta}}(1/\eta,t) = e^{\sigma^* t}\sum_{k=0}^{\infty}\hat{a}_k^*\eta^{-k}. \tag{4.54}$$

where $\{\hat{a}_n^*\}$ are assumed independent of $\{\hat{a}_n\}$, and truncate the infinite sum so that

$$\hat{\zeta}(\eta,t) \approx e^{\sigma t}\sum_{k=0}^{\mathcal{N}}\hat{a}_k\eta^k. \tag{4.55}$$

$\mathcal{N}$ will be picked as a power of 2. The Laurent series coefficients of functions will be obtained using a FFT of order $\mathcal{M}$, where $\mathcal{M}$ is at least two powers of 2 larger than $\mathcal{N}$ to prevent aliasing errors.

Define, as before the pre-images of the line vortex perturbations to be

$$\hat{z}_k = \hat{\zeta}_k z_{0\zeta}(\zeta_{k0}) + \hat{z}(\zeta_{k0}), \quad k = 0,...,N. \tag{4.56}$$

Then we obtain a set of $\mathcal{N} + 2N - 1$ unknowns,

$$\begin{aligned} &\left\{\hat{a}_k \middle| k = 1...\tfrac{\mathcal{N}}{2} - 1\right\}, \quad \left\{\hat{a}^*_k \middle| k = 2...\tfrac{\mathcal{N}}{2} - 1\right\}, \\ &\{\hat{\eta}_k | k = 0...N\}, \qquad\qquad \{\hat{\eta}^*_k | k = 0...N\}, \end{aligned} \tag{4.57}$$

4.4.4 Riemann-Hilbert problem

The perturbed velocity field is given by $u - iv = -\frac{i}{2}(1 + \zeta\bar{\zeta})^2\psi_\zeta$. ψ_ζ is given by (4.53), and hence applying continuity of ψ_ζ on the boundary guarantees continuity of velocity on the boundary. Hence

$$\left(\frac{\bar{\zeta}}{(1 + \zeta\bar{\zeta})} - \frac{\gamma_0}{\zeta - \zeta_0} - \sum_k \frac{\gamma_k}{\zeta - \zeta_k}\right) = G(\zeta) - F(\zeta), \qquad \zeta \in \partial D. \tag{4.58}$$

Since $G(\zeta)$ is analytic outside D and $F(\zeta)$ is analytic inside D, (4.58) is in the form of a Riemann-Hilbert problem, admitting a Plemelj solution. Writing

$$\left(\frac{\bar{\zeta}}{(1 + \zeta\bar{\zeta})} - \frac{\gamma_0}{\zeta - \zeta_0} - \sum_k \frac{\gamma_k}{\zeta - \zeta_k}\right) = P(\zeta), \tag{4.59}$$

then

$$F(\zeta, t) = \frac{-1}{2\pi i} \oint_{\partial D} \frac{P(\zeta')\mathrm{d}\zeta'}{(\zeta' - \zeta)} \qquad \zeta \in D \tag{4.60}$$

and

$$G(\zeta, t) = \frac{-1}{2\pi i} \oint_{\partial D} \frac{P(\zeta')\mathrm{d}\zeta'}{(\zeta' - \zeta)} \qquad \zeta \notin D. \tag{4.61}$$

However, noting that the line vortex terms lie within D, then we obtain the form

$$F(\zeta, t) = \frac{1}{2\pi i} \oint_{\partial D} \frac{-\bar{\zeta}'}{(1 + \zeta'\bar{\zeta}')} \frac{\mathrm{d}\zeta'}{(\zeta' - \zeta)} \qquad \zeta \in D \tag{4.62}$$

for F.

4.4.5 F expansions

F expansions near the patch boundary

As the $F(\zeta, t)$ is known to be analytic in ζ through-out the domain D, it can be expressed as a Taylor series,

$$F(\zeta, t) = \sum_{k=0}^{\infty} F_k \zeta^k, \tag{4.63}$$

where $F_k \in \mathbb{C}$ are the constant coefficients of the Taylor series.

Then expanding (4.62),

$$F_k(\zeta,t) = -\frac{1}{2\pi i}\oint_{\partial D}\frac{\bar{\zeta}'}{\zeta'^{k+1}(1+\zeta'\bar{\zeta}')}d\zeta'. \tag{4.64}$$

We now substitute $\zeta'(\eta) = \zeta_0(\eta) + \epsilon\hat{\zeta}(\eta)$. $F(\zeta,t)$ can now be expressed as the sum of $O(1)$ and $O(\epsilon)$ terms, so

$$F(\zeta,t) = F_0(\zeta,t) + \epsilon\hat{F}(\zeta,t). \tag{4.65}$$

and

Then expanding (4.64),

$$F_{k0} = -\frac{1}{2\pi i}\oint_{|\eta'|<1}\frac{\bar{\zeta_0}(1/\eta')\zeta_{0\eta}(\eta')}{\zeta_0(\eta')^{k+1}(1+\zeta_0(\eta')\bar{\zeta_0}(1/\eta')}d\eta'. \tag{4.66}$$

Additionally,

$$\begin{aligned}\hat{F}_k \quad = \quad & \frac{-1}{2\pi i}\oint_{|\eta|=1}\left(\frac{-(k+1)\zeta_0(\eta)^{-k-2}\bar{\zeta_0}(1/\eta)}{(1+\zeta_0(\eta)\bar{\zeta_0}(1/\eta))}\zeta_{0\eta}(\eta) - \right.\\ & \left.\frac{\zeta_0(\eta)^{-1-k}\bar{\zeta_0}(1/\eta)^2}{(1+\zeta_0(\eta)\bar{\zeta_0}(1/\eta))^2}\zeta_{0\eta}(\eta)\right)\hat{\zeta}\mathrm{d}\eta \\ & -\frac{1}{2\pi i}\oint_{|\eta|=1}\frac{\zeta(\eta)^{-1-k}\bar{\zeta_0}(1/\eta)}{(1+\zeta_0(\eta)\bar{\zeta_0}(1/\eta))}\hat{\zeta}_\eta\mathrm{d}\eta \\ & -\frac{1}{2\pi i}\oint_{|\eta|=1}\frac{\zeta(\eta)^{-1-k}}{(1+\zeta_0(\eta)\bar{\zeta_0}(1/\eta))^2}\zeta_{0\eta}(\eta)\bar{\hat{\zeta}}\mathrm{d}\eta. \end{aligned} \tag{4.67}$$

F expansions near satellite line vortices

The j-th line vortex is at the point ζ_j in the ζ-plane. We wish to expand $F(\zeta,t)$ for ζ near ζ_j in a Taylor series of form

$$F(\zeta,t) = \sum_k F_k^{(lv)}(\zeta-\zeta_j)^k. \tag{4.68}$$

for ζ near ζ_j. Expanding (4.62),

$$\begin{aligned}
F(\zeta,t) &= \frac{-1}{2\pi i}\oint_{\partial D}\frac{\bar{\zeta}'(1/\eta)\zeta'_\eta(\eta)}{(1+\zeta'(\eta)\bar{\zeta}'(1/\eta))(\zeta'(\eta)-\zeta_j)}\mathrm{d}\eta \\
&= \frac{-1}{2\pi i}\oint_{\partial D}\frac{\bar{\zeta}'(1/\eta)\zeta'_\eta(\eta)}{(1+\zeta'(\eta)\bar{\zeta}'(1/\eta))}\frac{\mathrm{d}\eta}{(\zeta'(\eta)-\zeta_j)-(\zeta(\eta)-\zeta_j)} \\
&= \frac{-1}{2\pi i}\oint_{\partial D}\frac{\bar{\zeta}'(1/\eta)\zeta'(\eta)_\eta}{(1+\zeta'(\eta)\bar{\zeta}'(1/\eta))}\frac{\mathrm{d}\eta}{(\zeta'(\eta)-\zeta_j)}\sum_{n=0}^{\infty}\left(\frac{\zeta(\eta)-\zeta_j}{\zeta'(\eta)-\zeta_j}\right)^n .
\end{aligned} \tag{4.69}$$

Again substituting the perturbed map into this expression we can expand in terms of ϵ. As with the planar stability analysis, we only require the first term of the expansion, which is given near the j-th vortex by

$$\begin{aligned}
\hat{F}_j^{lv} &= \frac{-1}{2\pi i}\oint_{|\eta|=1}\bar{\zeta}_0(1/\eta)\zeta_{0\eta}(\eta)\frac{(1+\bar{\zeta}_0(\eta)(2\zeta_0(\eta)-\zeta_{j0}))}{(1+\zeta_0(\eta)\bar{\zeta}_0(1/\eta))(\zeta_0(\eta)-\zeta_{j0})^2}\hat{\zeta}(\eta,t)\mathrm{d}\eta \\
&\frac{-1}{2\pi i}\oint_{|\eta|=1}\frac{\bar{\zeta}_0(1/\eta)\zeta_{0\eta}(\eta)}{(1+\zeta_0(\eta)\bar{\zeta}_0(1/\eta))(\zeta_0(\eta)-\zeta_{j0})^2}\hat{\zeta}_j(\eta,t)\mathrm{d}\eta \\
&\frac{-1}{2\pi i}\oint_{|\eta|=1}\frac{\bar{\zeta}_0(1/\eta)}{(1+\zeta_0(\eta)\bar{\zeta}_0(1/\eta))(\zeta_0(\eta)-\zeta_{j0})}\hat{\zeta}_\eta(\eta,t)\mathrm{d}\eta \\
&\frac{-1}{2\pi i}\oint_{|\eta|=1}\frac{1}{(1+\zeta_0(\eta)\bar{\zeta}_0(1/\eta))^2}\zeta_{0\eta}(\eta)\bar{\hat{\zeta}}(1/\eta,t)\mathrm{d}\eta.
\end{aligned} \tag{4.70}$$

4.4.6 F near central line vortex

Similarly, near the central line vortex, put we split $\hat{F}_c^{lv}$, the expansion coefficient of $F(\zeta,t)$ near the central line vortex, into

$$
\begin{aligned}
\hat{F}_c^{lv} =& \frac{1}{2\pi i}\oint_{|\eta|=1} \frac{\bar{\zeta}_0(1/\eta)}{\zeta_0(\eta)^2(1+\zeta_0(\eta)\bar{\zeta}_0(1/\eta))}\zeta_{0\eta}(\eta)\hat{\zeta}_j(\eta,t)\mathrm{d}\eta \\
&- \frac{1}{2\pi i}\oint_{|\eta|=1} \frac{\bar{\zeta}_0(1/\eta)}{\zeta_0(\eta)+\zeta_0(\eta)^2\bar{\zeta}_0(1/\eta)}\hat{\zeta}_\eta(\eta,t)\mathrm{d}\eta \\
&- \frac{1}{2\pi i}\oint_{|\eta|=1} \frac{1}{\zeta_0(\eta)(1+\zeta_0(\eta)\bar{\zeta}_0(1/\eta))^2}\zeta_{0\eta}(\eta)\bar{\hat{\zeta}}(\eta,t)\mathrm{d}\eta.
\end{aligned}
\tag{4.71}
$$

4.4.7 Kinematic boundary condition

The patch boundary is convected with the local flow. We express this through

$$
\begin{aligned}
\mathrm{Re}\left[\frac{\zeta_t(\eta,t)\bar{\zeta}_\eta(1/\eta,t)}{\eta}\right] =& \mathrm{Re}\left[\frac{(u+iv)\bar{\zeta}_\eta(1/\eta,t)}{\eta}\right] \\
=& \mathrm{Re}\Big[(u-iv)\zeta_\eta(\eta,t)\eta\Big]
\end{aligned}
\tag{4.72}
$$

Expanding, and recalling $O(\epsilon^0)$ term are identically zero, as the the base state is a steady solution, (4.72) consists only of order ϵ terms,

$$
\begin{aligned}
\mathrm{Re}\left[\sigma\frac{\zeta_{0\eta}(1/\eta)\hat{\zeta}(\eta,t)}{\eta}\right] \quad = \quad & \mathrm{Re}\Bigg[\frac{-i\omega_0\eta\zeta_{0\eta}(\eta)}{2}(1+\zeta_0(\eta)\bar{\zeta}_0(1/\eta))^2 \\
& \left(\sum_{k=1}^{N}\hat{\zeta}_k(\eta,t)\left(\frac{-\gamma_s}{(\zeta_0-\zeta_{j0})^2}\right)+\sum_{k=0}^{\infty}\hat{F}_k(t)\zeta_0(\eta)^k\right. \\
& \frac{\bar{\hat{\zeta}}(1/\eta,t)}{1+\zeta_0(\eta)\bar{\zeta}_0(1/\eta)} - \frac{\hat{\zeta}(\eta,t)\bar{\zeta}_0^2(1/\eta)}{(1+\zeta_0(\eta)\bar{\zeta}_0(1/\eta))^2} \\
& \left.-\frac{\zeta_0\bar{\zeta}(1/\eta)}{(1+\zeta_0(\eta)\bar{\zeta}_0(1/\eta))^2}\bar{\hat{\zeta}}(1/\eta,t)\right)\Bigg].
\end{aligned}
\tag{4.73}
$$

After taking the real part, coefficients of η can be equated on the left and right hand side to provide $\mathcal{N}-3$ equations in the perturbation coefficients and the pre-images of the line vortices.

4.4.8 Line Vortex Equations

We require

$$\frac{\mathrm{d}\bar{z}_c}{\mathrm{dt}} = (U - iV)|_{z=z_j}, \tag{4.74}$$

enforcing the requirement that the line vortices move with the local non-self-induced flow. $U - iV$, the non-self-induced velocity, is given by

$$U - iV = (u - iv) - \frac{i\kappa_j}{4}\left(\frac{1}{\zeta - \zeta_j} - \frac{\bar{\zeta}}{1 + \zeta\bar{\zeta}}\right) \tag{4.75}$$

at a line vortex with pre-image ζ_j in the ζ-plane, and strength κ_j

Hence we can derive the following equations.

Central Line Vortex

$$\sigma\hat{\bar{\zeta}}_0 = \frac{-i\omega}{2}\left[(1 - \gamma_0)\hat{\bar{\zeta}}_0 - \sum_k \frac{\gamma_k}{\zeta_{k0}^2}(\hat{\zeta}_k(t) - \hat{\zeta}_0(t)) + \hat{F}_0^{pv}\right] \tag{4.76}$$

Satellite Line Vortices

$$\begin{aligned}\sigma\bar{\hat{\zeta}}_j =& \frac{-i\omega}{2}(1 + \zeta_{j0}\bar{\zeta}_{j0})\left[\sum_{k\neq j}(\gamma_j\frac{(\hat{\zeta}_k(t) - \hat{\zeta}_j(t))}{(\zeta_{j0} - \zeta_{k0})^2}) - \frac{\gamma_0}{(\zeta_{j0} - \zeta_{00})^2}\left(\hat{\zeta}_0(t) - \hat{\zeta}_j(t)\right)\right.\\ &\left. - \frac{(1 - \gamma_j)\bar{\zeta}_{j0}}{(1 + \zeta_{j0}\bar{\zeta}_{j0})^2}\left(\hat{\zeta}_j\bar{\zeta}_{j0} + \bar{\hat{\zeta}}_j\zeta_{j0}\right) + \frac{(1 - \gamma_j)\hat{\bar{\zeta}}_j}{(1 + \zeta_{j0}\bar{\zeta}_{j0})} + \hat{F}_j^{(pv)}\right]\end{aligned} \tag{4.77}$$

The satellite and central line vortex equations, together with their complex conjugates, provide another $2N + 2$ equations in $\hat{a}_n$, $\hat{a}_n^*$, $\hat{\eta}_k$ and $\hat{\eta}_k^*$. Together with the equations from the kinematic boundary conditions (4.72), there is a total of $\mathcal{N} + 2 * N - 1$ equations in $\mathcal{N} + 2 * N - 1$ unknowns, in the form of a generalised eigenvalue problem,

$$\mathbf{Ax} = \sigma\mathbf{Bx}. \tag{4.78}$$

MATLAB was used to produce **A** and **B**, and hence to find the associated eigenvalues $\{\sigma\}$ and eigenvectors $\{\mathbf{x}\}$.

4.4.9 Numerical results

The code written to find the stability of these results was checked in a variety of manners. For extremely cusped configurations, the method breaks down. Hence numerical runs were repeated with different $\mathcal{N}$ and $\mathcal{M}$ until stability results had stabilised over increasing $\mathcal{N}$ and $\mathcal{M}$. Results which did not stabilise were near cusped patches, and are not shown. Typically the minimum $\mathcal{N}$ was required to be $\mathcal{N} = 256$, with $\mathcal{M} = 1024$, although specific examples were found with lower and higher requirements. As on the plane, the presence of a number of zero eigenvalue modes are expected in the spherical stability analysis. These will correspond again to bifurcations to neighbouring steady states. Neighbouring states are present with altered patch area, and vortex centroid shifted in either of the local Cartesian coordinates. The alteration of the patch area corresponds to altering R, and is not allowed under the formulation as it corresponds to a change in total vorticity. Modes which are found to possess a nonzero change in area, angular momentum or or vortex centroid are not considered.

4.4.10 Checks

As discussed in section §4, the stability of these distributions is expected to follow certain behaviour in the following limit.

Firstly, as the patch area tends to 4π, the boundary modes and point vortex modes should decouple. As a result, the eigenvalues are expected to behave as $\pm 0.5i$ in boundary modes, following the example of the shielded rankine vortex on the sphere and separate point vortex modes, the stability of which mirror that of the Morikawa and Swenson distribution on a sphere.

Also, it is feasible to expect, as with the planar results, the eigenmodes to represent zero perturbation to the patch area, except for seven exhibiting non-zero perturbations.

4.4.11 Results

Results are presented here for the linear stability of the multipolar structures on a sphere. For various values of n, the order of the multipoles, and colatitude θ_0, the angle of the satellite vortices, the largest real part of eigenmodes is plotted.

Recall that for fixed n, as the angle of the ring of vortices, $\theta_0 \to 0$, i.e. the vortices tend to the north pole, the lowest values of the area A for which solutions exist increases. This is due to the patch becoming cusped “around” the line vortices. As $\theta_0 \to \pi$, however, this lowest A decreases. The limit $A \to 4\pi$ is always admissible however.

There are two general points to be noted. Firstly, the stability of the structures for $A \to 4\pi$ is found in each case to be the same as the corresponding point of the $\omega = 0$ curve in the Morikawa and Swenson type point vortex model. As noted previously, this is to be expected, as the patch of vorticity is now close to covering the whole sphere. Hence it is seen by the (non-rotating) vortex patch as a uniform patch of vorticity covering the whole sphere. The problem therefore decouples into the point vortex problem, and a patch boundary, which will, for θ_0 sufficiently close to π, be approximated by the shielded Rankine vortex problem. Indeed, as predicted by this, as the patch area tends to 4π, the eigenvalues associated purely with the patch boundary tend to $\pm i/2$. This is seen in Fig. 4.16. Note firstly that the eigenvalues occur in complex conjugate quartets, as expected as the system is Hamiltonian. As the patch area increases from 4.4718 to 4π, it can be seen that multiple eigenvalues begin to cluster around $\pm i/2$. In the final picture, the eigenvalues have separated into clusters at $\sigma_k = \pm i/1$, a cluster at $\sigma_k = 0$, with isolated other points. These isolated values include the unstable eigenvalues at approximately ± 3. The mode of instability also corresponds to that observed in the point vortex model, i.e. the instability is purely satellite vortex modes.

We now examine specific stability behaviour.

Fig. 4.16: Plot of eigenvalues for $n = 5$, $\theta = 135$. Top left: area = 4.4718, top right: area = 5.1503, middle left: area = 5.9393, middle right: area = 6.7073, bottom left: area = 7.7628, bottom right: area = 12.4441.

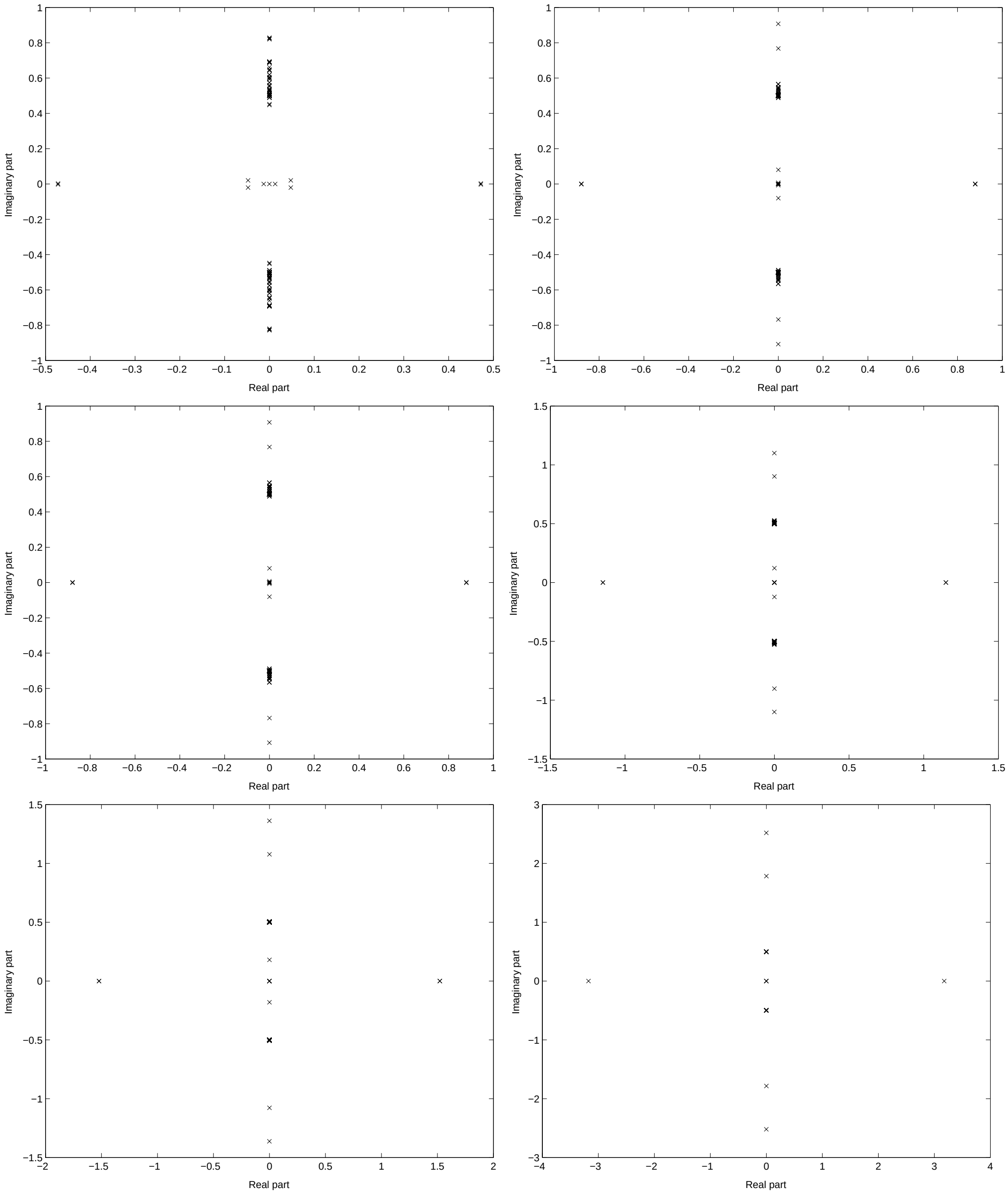

Fig. 4.17: Plot of maximum real part of eigenvalues against patch area for $n = 2$, $\theta = 135$

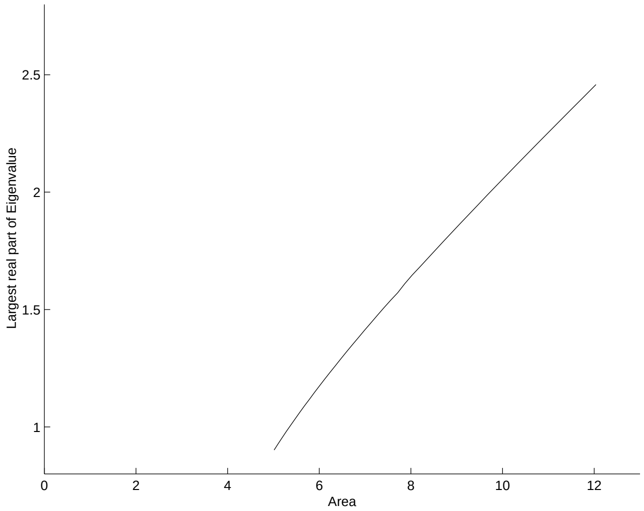

Stability of $n = 2$ solutions

The case $n = 2$ is, for all θ_0 in our multipolar solutions, unstable. As with the planar results, this is at odds with other observations. However, we comment that the class of solutions considered here is a small sub-class of possible multipolar solutions, with strong constraints placed to allow them to be represented in a mathematically exact form. Hence it is not entirely infeasible that stability behaviour be different from physical cases. Figures 4.17, 4.18 and 4.19 show the largest unstable eigenvalue for $\theta_0 = 135$, $\theta_0 = 160$ and $\theta_0 = 177$ respectively. The instability is universally at a maximum when $A \to 4\pi$, corresponding to the purely point vortex case, which is unstable, and is unstable in the central point vortex, as expected. As A decreases, and hence the boundary approaches the point vortices, the instability becomes smaller in magnitude. Note that as θ_0 decreases the direction of inflection of the graph changes. This reflects some change in the balance between the effects of the point vortex interactions and the point vortex to patch interactions. As the patch is neutrally stable, the increasing proximity of the patch boundary appears to lessen the unstable point vortex to point vortex interactions.

Fig. 4.18: Plot of maximum real part of eigenvalues against patch area for $n = 2$, $\theta = 160$

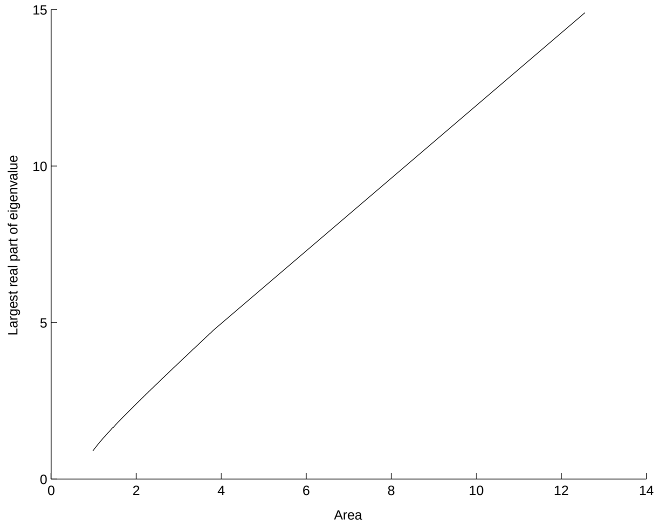

Fig. 4.19: Plot of maximum real part of eigenvalues against patch area for $n = 2$, $\theta = 177$

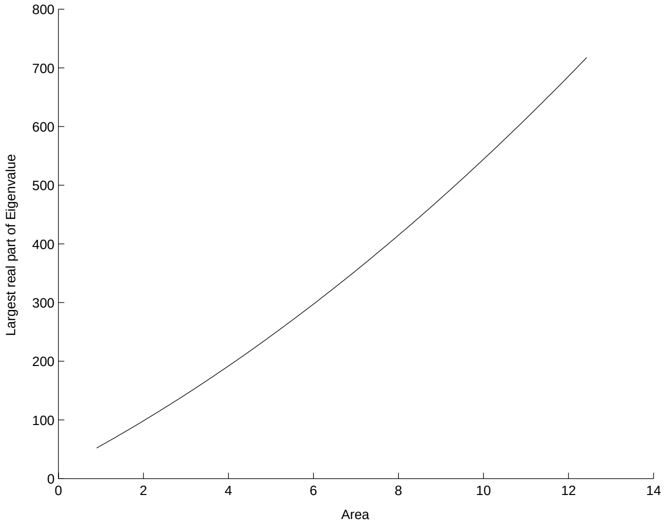

Stability of $n = 3$ solutions

The $n = 3$ case is instructive, as it differs radically from the planar stability behaviour. Figures 4.20, 4.22 and 4.23 show the largest unstable eigenvalue for $\theta_0 = 90$, $\theta_0 = 135$ and $\theta_0 = 160$. Figure 4.21 shows the limit $A \to 4\pi$ with $\theta_0 = 90$. Recall that in that in Chapter 2, it was found that the planar quadrupole is uniformly stable, in agreement with experimental and numerical results on patch vortex models, which are generally robust for most parameter values. On the sphere, however, exact multipolar behaviour is different from that on the plane. For the θ_0 which admit multipolar solutions, while the distribution is stable for the $A \to 4\pi$ limit (again in agreement with the point vortex model), as A decreases the point vortices become unstable as the patch draws closer to the vortex distribution. As the patch distortion increases, the multipole becomes unstable in the patch vortex modes. It is important to separate the instability due to curvature effects from instability which is an artifact of the numerical method. This is achieved by ensuring the results are steady with $\mathcal{N}$. There is a change in largest eigenmode can be seen clearly in Fig. 4.24. At around $A = 1.322$, the boundary mode (dashed line) becomes dominant over the satellite vortex mode (dotted line). The base solution at $A = 1.322$ can be seen in Fig. 4.25, and is seen to be distorted from circular but not cusped. In general, the patch itself is unstable only in configurations distorted from circular. As this mechanism does not exhibit itself in the tripolar case or shielded Rankine vortex on the sphere, or at all on the plane, it is suggested that the degree of symmetry combined with the curvature are crucial to the instability.

There are θ_0 values at which the stabilising effects of the patch balance the growing instability of central line vortex before the patch boundary itself becomes unstable. This is shown in figure 4.23.

Fig. 4.20: Plot of maximum real part of eigenvalues against patch area for $n = 3$, $\theta = 90$

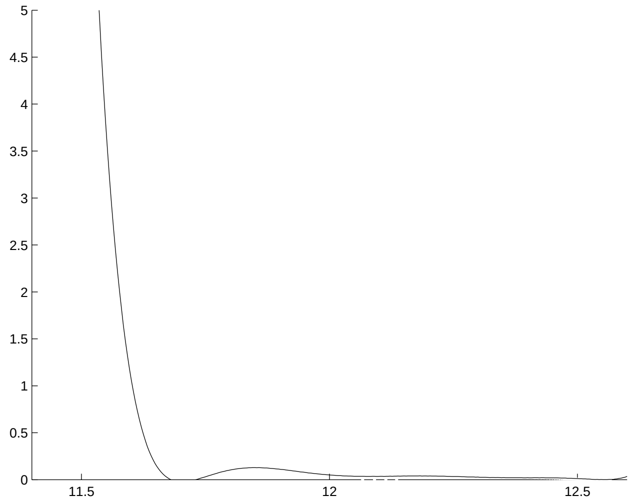

Fig. 4.21: Large area plot of maximum real part of eigenvalues against patch area for $n = 3$, $\theta = 90$

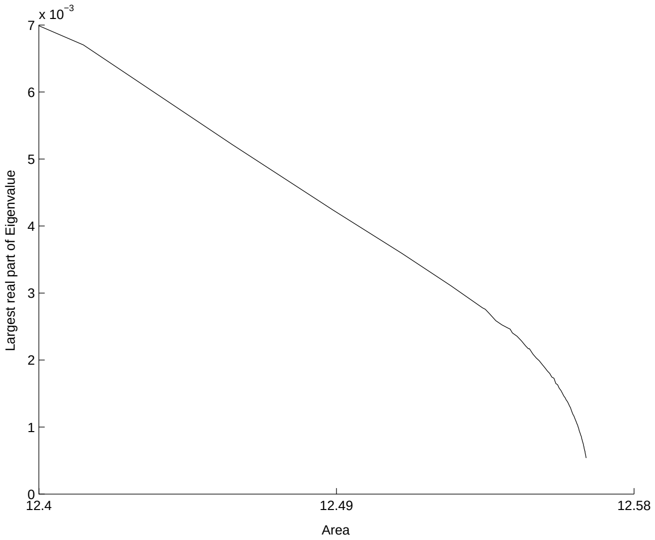

Fig. 4.22: Plot of maximum real part of eigenvalues against patch area for $n = 3$, $\theta = 135$

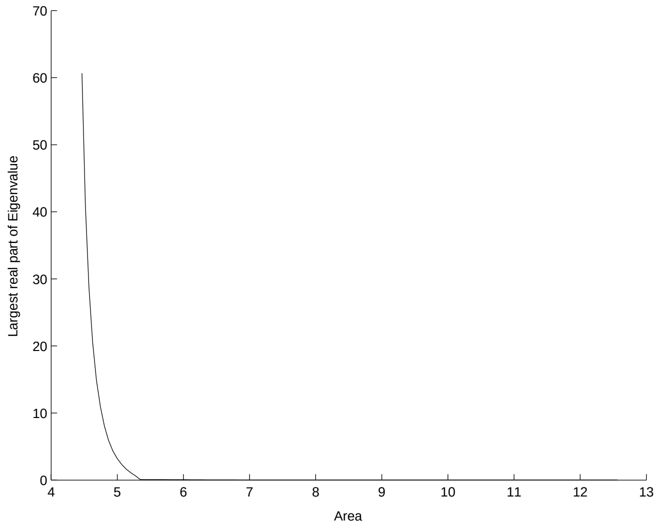

Fig. 4.23: Plot of maximum real part of eigenvalues against patch area for $n = 3$, $\theta = 160$

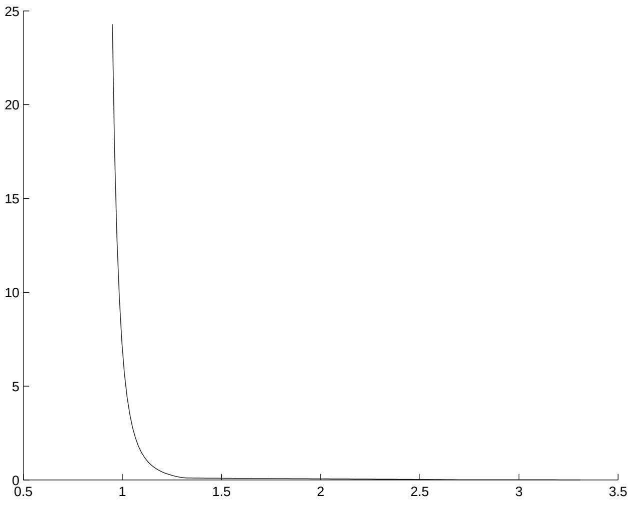

Fig. 4.24: Zoomed plot of maximum real part of eigenvalues against patch area for $n = 3$, $\theta = 160$

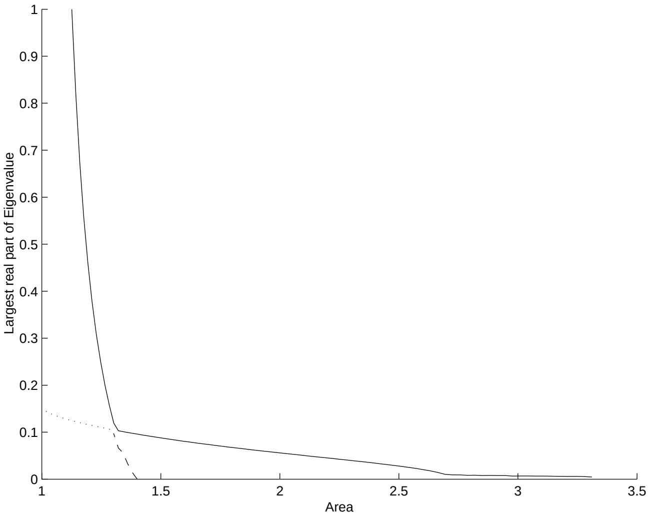

Fig. 4.25: Base state solution for $n = 3$, $\theta_0 = 160$, patch area $= 1.322$

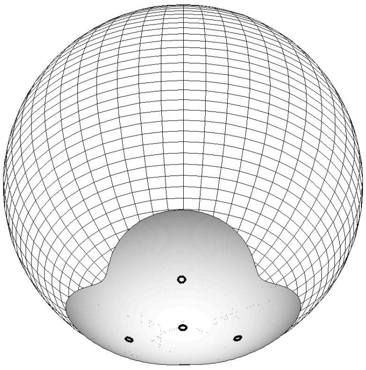

Fig. 4.26: Plot of maximum real part of eigenvalues against patch area for $n = 4$, $\theta = 90$

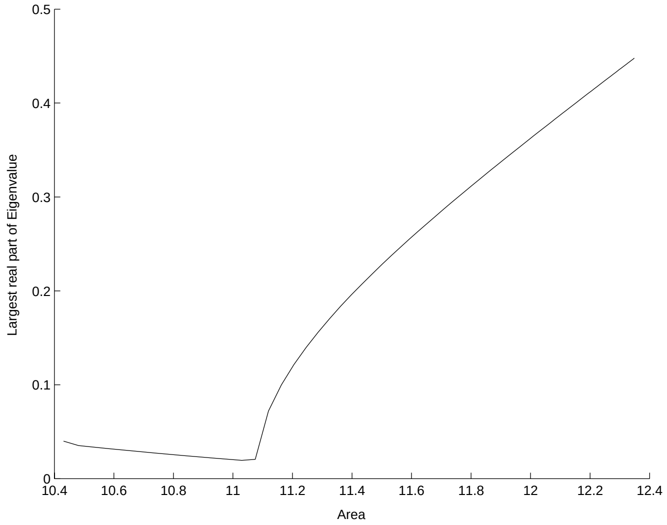

Stability of $n = 4$ solutions

In the $n = 4$, pentapolar case, the range of θ_0 for which multipolar solutions are admissible fall with in the unstable region of the $\omega = 0$ curve in the point vortex model. Hence for all solutions, as $A \to 4\pi$, the solutions are unstable. Figures 4.26, 4.27 and 4.29 show the largest unstable eigenvalue for $\theta_0 = 90$, $\theta_0 = 135$ and $\theta_0 = 160$. The instability for high A is in the eigenmodes associated with the satellite vortex. The size of the real part of these unstable eigenvalues decreases as A decreases, and hence the patch boundary becomes closer to the ring of vortices. As with the $n = 2$ case, this is taken to be caused by a stabilising effect in the patch to point vortex interactions. However, before the unstable satellite vortex modes become stable, the patch boundary modes exhibit an instability, as it approaches the cusped configuration. This boundary instability then increases as the boundary becomes more cusped.

Fig. 4.27: Plot of maximum real part of eigenvalues against patch area for $n = 4$, $\theta = 135$

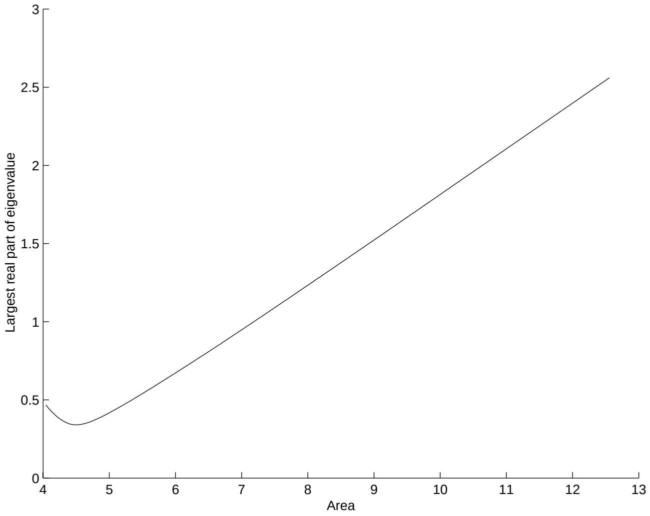

Fig. 4.28: Plot of maximum real part of eigenvalues against patch area for $n = 4$, $\theta = 160$

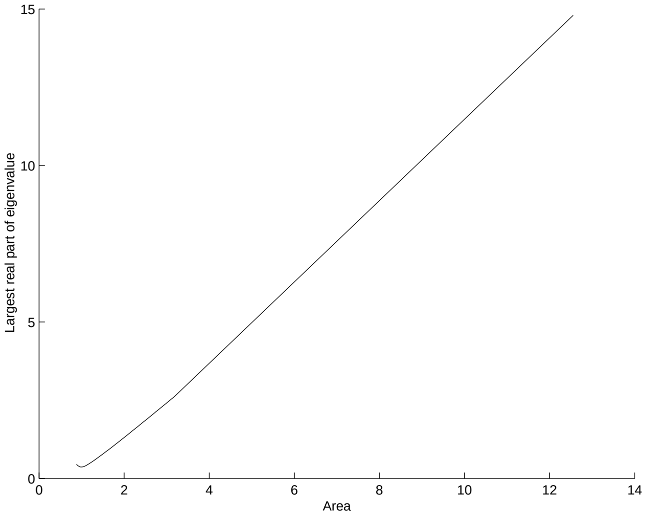

Fig. 4.29: Zoomed plot of maximum real part of eigenvalues against patch area for $n = 4$, $\theta = 160$

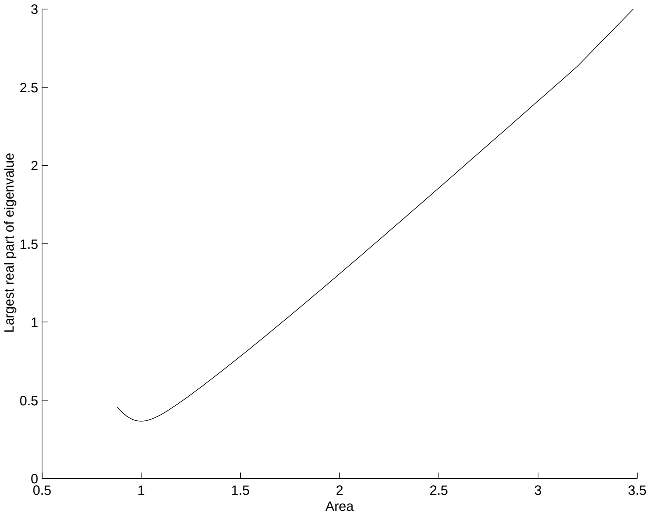

Fig. 4.30: Plot of maximum real part of eigenvalues against patch area for $n = 5$, $\theta = 0.7$ radians.

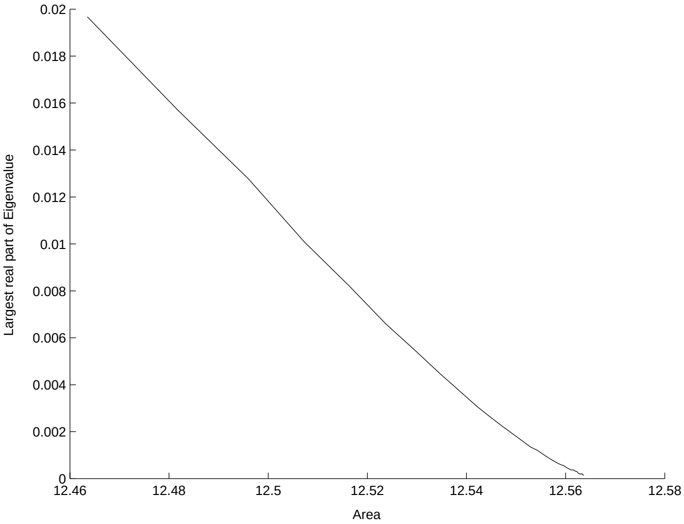

Stability of $n = 5$ solutions

Figures 4.30, 4.31 and 4.32 show the largest unstable eigenvalue for $\theta_0 = 0.7$, $\theta_0 = 45$ and $\theta_0 = 135$. The sextapolar case exhibits two distinct behaviours. For distributions such that $A \to 4\pi$ is stable, the behaviour is dominated by the growth of the instability associated with the boundary mode. For θ_0 where $A \to 4\pi$ is unstable, through satellite mode instabilities, this instability decreases as A decreases, until it is overtaken by boundary instabilities, as in the pentapolar solutions.

Fig. 4.31: Plot of maximum real part of eigenvalues against patch area for $n = 5$, $\theta = 45$.

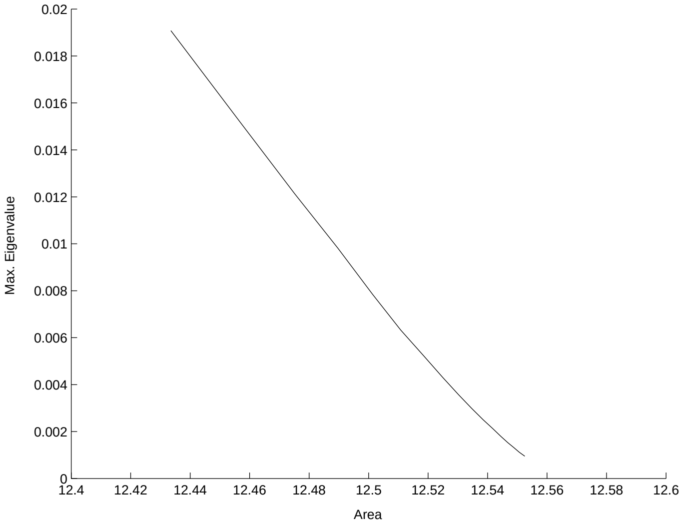

Fig. 4.32: Plot of maximum real part of eigenvalues against patch area for $n = 5$, $\theta = 135$

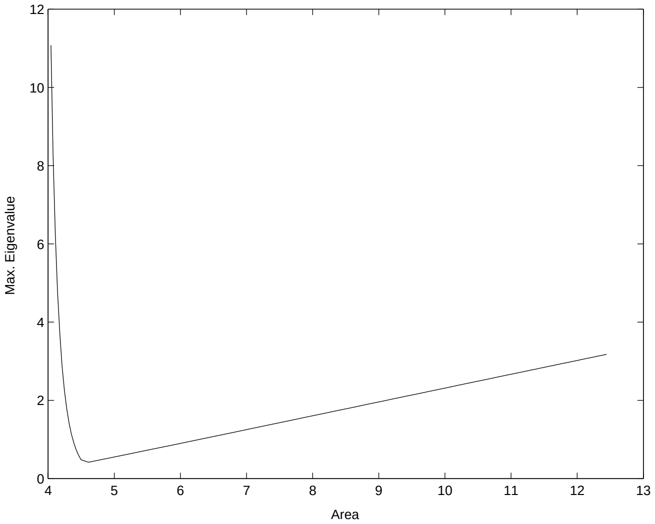

4.4.12 Discussion

In general, the stability behaviour of the multipolar solutions on the sphere is dominated by two effects. Firstly, the point vortex stability, which is the major effect for solutions with the patch covering a large area of the sphere. Here the stability behaviour can be largely predicted by the point vortex model of Section 4.1. Then, as the patch boundary draws closer to the point vortices, it becomes distorted from circular. For all $n > 2$, this distortion results in the patch boundary becoming unstable. Hence the general behaviour can be divided into 3 cases.

1. $n = 2$. Here the stability of the tripole behaves in a similar manner to the plane, due to the absence of boundary instability. Hence for $A \to 4\pi$, which corresponds to a large in the planar results of Section 2.7, the distribution is unstable , with this instability decreasing as the area of the patch decreases.
2. $n > 2$, point vortex model stable. Here, for $A < 4\pi$, the stability is dominated by any point vortex instability which arises (this occurs in $n = 3$, but not for $n = 5$), and then for sufficiently low A, by the boundary instability. Hence these structures are stable only for the limit $A = 4\pi$.
3. $n > 2$, point vortex model unstable. In these cases, as area decreases from 4π, there is a decreasing vortex mode instability, the patch boundary approach stabilising the satellite vortex instability. For some area, this is overtaken by the boundary instability, which then increases as area decreases. Hence these cases are unstable for all patch areas.

The main difference in stability behaviour on the sphere as compared to the plane is the instability induced in the patch boundary as it becomes more distorted. In [28], Polvani and Dritschel find that curvature effects on the sphere have a destabilising effect on point vortex arrays. A similar destabilising effect seems present with the multipolar solutions presented here, if the boundary is sufficiently asymmetric. For the $n = 2$, and indeed circular shielded Rankine vortex case, the high degree of symmetry prevents the curvature effects destabilising the patch boundary even when distorted around the point vortices.

CHAPTER 5

Singly periodic vortex equilibria combining patch vorticity and point vortices

5.1 Introduction

We now present a class of solutions to the two-dimensional Euler equations using the methods of [3], which are singly period. Each period will consist of a symmetric region of constant vorticity, with either one or three line vortices superposed on the real axis.

Singly periodic point vortex distributions of have long been used to model fluid phenomena. The most well known of these is the Karman vortex street [46, 47], which models the laminar wake of a circular cylinder in a moderately viscous fluid. Lamb [39] also presents an infinite row of point vortices and examines the stability. Distributions with more than one point vortex per period are examined in [48]. Singly periodic finite area vortices have also been presented. Inviscid models include the model of Saffman and Schatzman [49], which has a finite area core. In common with the multipolar work, contour dynamics have also been used to create and examine finite area equilibria [50, 51].

Again, the point vortex model is more tractable analytically, while the finite area patch models are physically more realistic. The combination of patch and point vorticity therefore again captures some of the more complex shape characteristics while allowing exact solutions to be obtained.

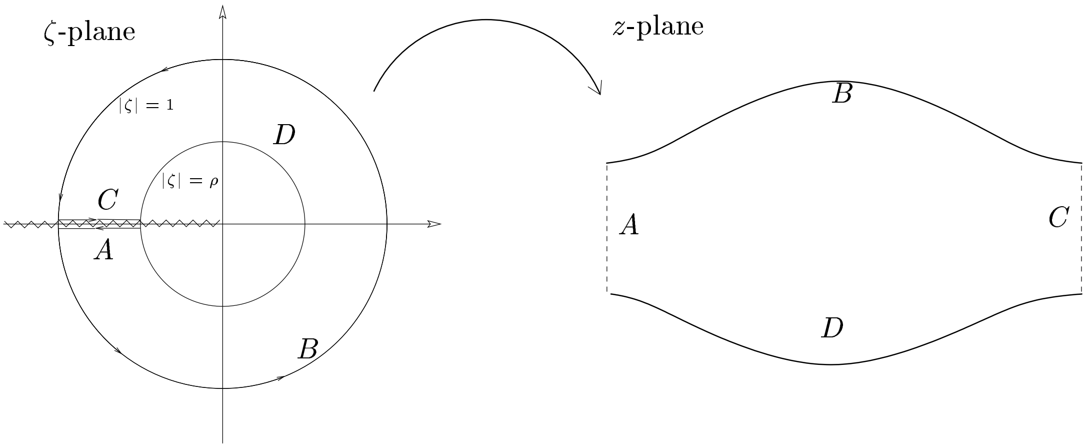

Fig. 5.1: Conformal map from ζ-plane annulus to the z-plane. A, B, C and D mark the boundaries in each plane.

5.2 Exact solutions with one vortex per period

As in [3], we wish for a velocity field of form

$$u - iv = \begin{cases} \frac{i\omega_0 \bar{z}}{2} - \frac{i\omega_0}{2} S(z), & z \in D \\ 0, & z \notin D \end{cases} \tag{5.1}$$

where $S(z)$ is the Schwarz function. D has previously been some simply connected region. We now replace this D with a more complex domain. We previously used a conformal map from the unit circle in the ζ-plane to the z-plane to define D. We now replace this map from the unit circle in the ζ-plane with a map from some annulus. We will present a conformal map which takes this annulus to an infinite band in the z-plane. As before, we require that singularities in $S(z)$ are in the form of simple poles with real residues, and that the line vortices corresponding to these poles are stationary.

5.2.1 The conformal map

A meromorphic function $f(\zeta)$ on the annulus $\rho < |\zeta| < 1/\rho$ is *loxodromic* if

$$f(\rho^2 \zeta) = f(\zeta). \tag{5.2}$$

Hence the annulus $\rho < |\zeta| < 1/\rho$ is the fundamental domain of $f(\zeta)$, and f is periodic radially.

A meromorphic function $f(\zeta)$ on the annulus $\rho < |\zeta| < 1/\rho$ is *quasi-loxodromic* if

$$f(\rho^2\zeta) = f(\zeta) + C, \tag{5.3}$$

where $C \in \mathbb{C}$ is some constant.

Define a function $P(\zeta;\rho)$ such that

$$P(\zeta;\rho) = (1-\zeta)\prod_{k=1}^{\infty}(1-\rho^{2k}\zeta)(1-\rho^{2k}/\zeta). \tag{5.4}$$

We take $\rho < 1$. Then the following properties can be derived:

$$\begin{aligned} P(\rho^2\zeta;\rho) = &\quad -\frac{1}{\zeta}P(\zeta;\rho), \\ P(\zeta^{-1};\rho) = &\quad -\frac{1}{\zeta}P(\zeta;\rho). \end{aligned} \tag{5.5}$$

Additionally, define a function $K(\zeta;\rho)$ such that

$$K(\zeta;\rho) = \zeta\frac{P'(\zeta;\rho)}{P(\zeta;\rho)}. \tag{5.6}$$

Then, using the properties (5.5), it can be shown that

$$K(\rho^2\zeta;\rho) = K(\zeta;\rho) - 1, \tag{5.7}$$

and hence $K(\zeta;\rho)$ is a quasi-loxodromic function. In addition within the fundamental domain $\rho < |\zeta| < 1/\rho$, $K(\zeta;\rho)$ has only a simple pole at the point $\zeta = 1$.

5.2.2 A periodic solution with one line vortex

Using these two function, we form the conformal map

$$z(\zeta) = -\frac{i\lambda}{2\pi}\left[\log\zeta + R_1(\rho)K(\zeta\sqrt{\rho},\rho) + R_2(\rho)\right], \tag{5.8}$$

where $\lambda, \rho \in \mathbb{R}$ are parameters of the map, and $R_1(\rho), R_2(\rho) \in \mathbb{R}$ are constants. ρ is taken such that $0 < \rho < 1$. $z(\zeta)$ maps from the annular domain $\mathcal{D} = \{\zeta; \rho < |\zeta| < 1\}$ to the complex z-plane (see Fig. 5.1). The domain $\mathcal{D}$ is defined to occupy the same Riemann surface as $\log(\zeta)$, due to the branch cut in the log function. Define also $D = \{z(\zeta); \zeta \in \mathcal{D}\}$ as the image of the domain. We restrict attention from now on to the specific Riemann sheet on which $\arg(\zeta) \in [-\pi, \pi]$. We take the branch cut of $\log(\zeta)$ to be from the origin to $-\infty$, and no other functions in $z(\zeta)$ have branch cuts. Then for $\zeta \in \mathcal{D}$, the z-plane image of the top of the branch cut will map to the right hand edge of the domain D. The bottom of the branch cut will map to the left-hand edge, and the boundaries $|\zeta| = \rho$ and $|\zeta| = 1$ will map to the upper and lower boundaries of D respectively. λ is the length of the domain in the z-plane. R_1 and R_2 are to be set to satisfy the physical conditions.

We form again a velocity field

$$u - iv = \begin{cases} \dfrac{i\omega_0 \bar{z}}{2} - \dfrac{i\omega_0}{2} S(z), & z \in D \\ 0, & z \notin D \end{cases} \tag{5.9}$$

However the domain D considered now has two boundaries, corresponding to $\{z(\zeta); |\zeta| = 1\}$, and $\{z(\zeta); |\zeta| = \rho\}$. We define two Schwarz functions, one for each boundary,

$$S_1(z) = \bar{z}(1/\zeta) \tag{5.10}$$

$$S_2(z) = \bar{z}(\rho^2/\zeta), \tag{5.11}$$

equal to $\overline{z(\zeta)}$ on the top and bottom z-plane boundaries respectively. We require that $S_1(z)$ and $S_2(z)$ be equal, thus guaranteeing continuity of velocity across both patch boundaries. Then

$$S_1(z(\zeta)) \quad = \quad \frac{i\lambda}{2\pi} \left\{ \log \frac{1}{\zeta} + R_1(\rho) K(\frac{\sqrt{\rho}}{\zeta}; \rho) + R_2(\rho) \right\}, \tag{5.12}$$

$$S_2(z(\zeta)) \quad = \quad \frac{i\lambda}{2\pi} \left\{ \log \frac{\rho^2}{\zeta} + R_1(\rho)(K(\frac{\sqrt{\rho}}{\zeta}; \rho) - 1) + R_2(\rho) \right\}, \tag{5.13}$$

after applying (5.7). As $S_1(z(\zeta))$ and $S_2(z(\zeta))$ must be equal, this sets that

$$R_1(\rho) = 2 \log \rho. \tag{5.14}$$

Next, by requiring that the pre-image of the physical origin is the point $\sqrt{\rho}$, i.e. that $z(\sqrt{\rho}) = 0$, it can be seen that

$$R_2(\rho) = -\frac{1}{2}\log\rho. \tag{5.15}$$

Hence the conformal map is given by

$$z(\zeta) = -\frac{i\lambda}{2\pi}\left[\log\zeta + 2\log\rho K(\zeta\sqrt{\rho};\rho) - \frac{1}{2}\log(\rho)\right]. \tag{5.16}$$

This map is a function only of the parameter ρ and the wavelength, λ, and the corresponding Schwarz function by

$$S(z(\zeta)) = \frac{i\lambda}{2\pi}\left\{-\log\zeta + 2\log\rho K(\frac{\sqrt{\rho}}{\zeta};\rho) - \frac{1}{2}\log(\rho)\right\}. \tag{5.17}$$

Examining $S(z(\zeta))$, we see that the term $K(\sqrt{\rho}/\zeta)$ has a simple pole at $\zeta = \sqrt{\rho}$, and hence there is a line vortex in the corresponding velocity field. We now find the residue of this simple pole, and hence find the strength of the point vortex, and show it is stationary.

5.2.3 Point vortex strength

The K function will be singular at zeros of the P function. Write

$$P(\zeta,\rho) = (1-\zeta)\hat{P}(\zeta,\rho), \tag{5.18}$$

where

$$\hat{P}(\zeta,\rho) = \prod_{k=1}^{\infty}(1-\rho^{2k}\zeta)(1-\rho^{2k}/\zeta). \tag{5.19}$$

$\hat{P}(\zeta,\rho)$ has zeros only at $\zeta = \rho^{\pm 2k}$, which are outside the fundamental domain.

Hence, in our fundamental domain, the function $K(u\zeta)$ has only a simple pole at $\zeta = 1/u$.

Write

$$\hat{K}(\zeta) = \frac{\zeta P'(\zeta)}{\hat{P}(\zeta)}, \tag{5.20}$$

so $\hat{K}(\zeta)$ is analytic at $\zeta = 1$. In the velocity field, (5.9) the Schwarz function contains terms of form $K(\sqrt{\rho}/\zeta)$, singular at $\zeta = \sqrt{\rho}$. Then near $\zeta = \sqrt{\rho}$,

$$K\left(\frac{\sqrt{\rho}}{\zeta}\right) = \frac{A_{-1}}{\zeta - \sqrt{\rho}} + A_0 + A_1(\zeta - \sqrt{\rho}) + \dots \tag{5.21}$$

Then

$$\begin{aligned} K\left(\frac{\sqrt{\rho}}{\zeta}\right) &= \hat{K}\left(\frac{\sqrt{\rho}}{\zeta}\right)\frac{1}{1-\sqrt{\rho}/\zeta} \\ &= \frac{\zeta}{\zeta - \sqrt{\rho}}\hat{K}\left(\frac{\sqrt{\rho}}{\zeta}\right). \end{aligned} \tag{5.22}$$

where $\zeta\hat{K}(\sqrt{\rho}/\zeta)$ is analytic near $\zeta = \sqrt{\rho}$, and hence has a Taylor series,

$$\zeta\hat{K}\left(\frac{\sqrt{\rho}}{\zeta}\right) = \sqrt{\rho}\hat{K}(1) + \frac{\partial}{\partial\zeta}\left\{\zeta\hat{K}\left(\frac{\sqrt{\rho}}{\zeta}\right)\right\}_{\zeta=\sqrt{\rho}} + \dots \tag{5.23}$$

Then

$$A_{-1} = \sqrt{\rho}\hat{K}(1) \tag{5.24}$$

$$A_0 = \frac{\partial}{\partial\zeta}\left\{\zeta\hat{K}(\frac{\sqrt{\rho}}{\zeta})\right\}_{\zeta=\sqrt{\rho}}. \tag{5.25}$$

However, to find the strength of the line vortex at $\zeta = \sqrt{\rho}$, we must expand in the z-plane. For $z(\zeta)$ near $z(\sqrt{\rho})$, recalling that $z(\sqrt{\rho})$ is mapped to the origin,

$$S(z(\zeta)) = \frac{b_{-1}}{z(\zeta)} + b_0 + \dots \tag{5.26}$$

The conformal map can itself be expressed as a Taylor series manipulation of which gives

$$z(\zeta) = (\zeta - \sqrt{\rho})\left\{z'(\sqrt{\rho}) + \frac{z''(\sqrt{\rho})}{2}(\zeta - \sqrt{\rho}) + \dots\right\} \tag{5.27}$$

We hence transform (5.22) to the z-plane, giving

$$\begin{aligned} K\left(\frac{\sqrt{\rho}}{\zeta}\right) &\sim \frac{A_{-1}z_\zeta(\sqrt{\rho})}{z(\zeta)} + \frac{A_{-1}z_{\zeta\zeta}(\sqrt{\rho})}{2z_\zeta(\sqrt{\rho})} + A_0 + ... && (5.28) \\ &\sim \frac{b_{-1}}{z(\zeta)} + b_0 + ... && (5.29) \\ & && (5.30) \end{aligned}$$

Hence

$$\begin{aligned} b_{-1} &= A_{-1}z_\zeta(\sqrt{\rho}) && (5.31) \\ b_0 &= \frac{A_{-1}z_{\zeta\zeta}(\sqrt{\rho})}{2z_\zeta(\sqrt{\rho})} + A_0. && (5.32) \end{aligned}$$

Recalling the definition of a point vortex with strength Γ_0 at $z = z_0$ to be

$$u - iv = -\frac{i\Gamma_0}{2\pi(z - z_0)}. \quad (5.33)$$

Examining (5.9), we see the most singular term is

$$u - iv = \frac{-\lambda\omega_0}{2\pi}\log\rho\frac{A_{-1}z_\zeta(\sqrt{\rho})}{z(\zeta)} + \dots \quad (5.34)$$

Hence, the strength of the line vortex at $\zeta = \sqrt{\rho}$ is given by

$$\Gamma_c = -i\omega_0\lambda\log(\rho)\sqrt{\rho}\hat{K}(1)z_\zeta(\sqrt{\rho}). \quad (5.35)$$

5.2.4 Stationarity condition

We must enforce the stationarity condition on this solution, which is clearly that the constant term in the Laurent expansion of (5.9) for $z(\zeta)$ near $z(\sqrt{\rho})$ is equal to zero. This is true if

$$\frac{\sqrt{\rho}\hat{K}(1)z_{\zeta\zeta}(\sqrt{\rho})}{2z_\zeta(\sqrt{\rho})} + \frac{\partial}{\partial\zeta}\left[\zeta\hat{K}\left(\frac{\sqrt{\rho}}{\zeta}\right)\right]_{\zeta=\sqrt{\rho}} = -\frac{\log(\sqrt{\rho})}{\log\rho}. \quad (5.36)$$

This is found by numerical means to be true for $0 < \rho < 1$.

5.2.5 Solutions

We find a range of solutions for ρ varying from 0 to 1. This forms a one parameter family of solutions. We consider however the more physical quantity, area of uniform vorticity per period, where

$$\text{Area} = \frac{1}{2}\Im\left[\oint_{\partial\mathcal{D}} \bar{z}z_\zeta \mathrm{d}\zeta\right]. \tag{5.37}$$

The area is found numerically to be a monotonically decreasing function of ρ.

As the structure has zero circulation per period, it is again true that

$$\Gamma_c = \omega_0 A. \tag{5.38}$$

We fix $\lambda = 1$, $\omega_0 = 1$. Then we find two limits which are of interest. Firstly, for $\rho \to 1$, the patch boundary tends to a circle with radius $r = 1/2$. Then the distribution tends to an infinite row of touching shielded Rankine vortices, each with area $\pi/4$. In this limit the solutions become cusped. This limiting case of the shielded Rankine vortex is seen also in both the planar and spherical multipolar solutions, and highlights the role of the shielded Rankine vortex as the simplest form of this combined point and patch vorticity. The left hand panel of Fig. 5.2 shows this limit.

As $\rho \to 0$,the patch tends to a band with height $z(1) - z(\rho) \to 2.8614$. This is shown in the left hand panel of Fig. 5.3.

The right hand panel of Fig. 5.2 shows an intermediate solutions, possessing a symmetric boundary of variable curvature. In the right hand panel of Fig. 5.3, the vortex circulation Γ is plotted against ρ. As expected, in the $\rho \to 1$ limit this tends to $\pi/4$, in the $\rho \to 0$ limit to 2.8614. The graph of Γ against area is not shown, as from (5.38), Γ is linear with area.

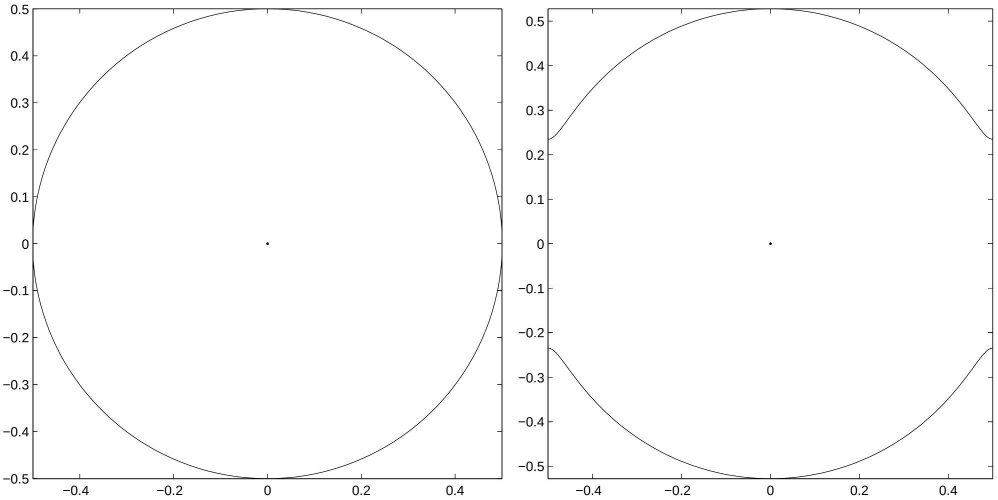

Fig. 5.2: Singly periodic patch solutions with a single point vortex. Left panel shows $\rho = 10^{-5}$, area $= 2.8614$. Right panel shows $\rho = 0.01$, area $= 0.8696$.

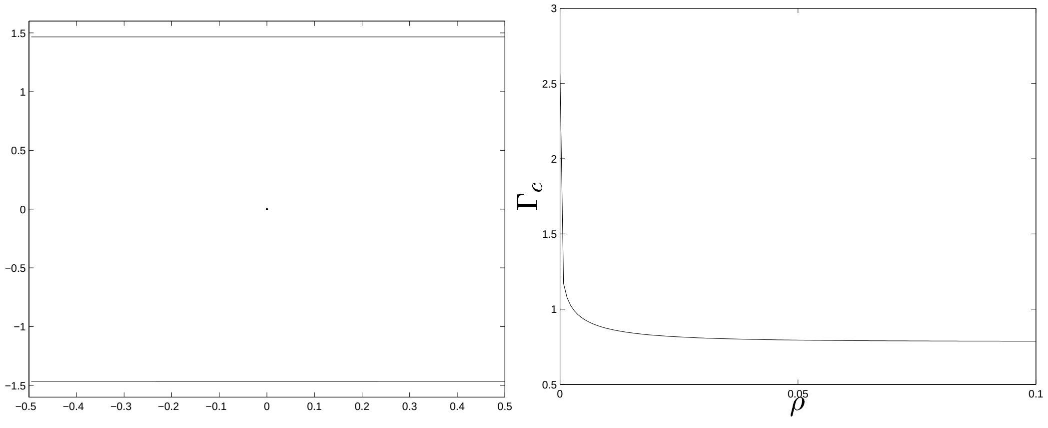

Fig. 5.3: Singly periodic solutions with a single point vortex. Left panel shows $\rho = 0.1$, area $= 0.7866$. Right panel shows the vortex circulation Γ_c against ρ.

5.3 Exact solutions with three vortices per period

We wish to add extra line vortices to our model. To this end, we postulate the form of the conformal map to be

$$z(\zeta) = -\frac{i\lambda}{2\pi}\left[\log\zeta + A_2K(\sqrt{\rho}\zeta) + A_3K(u_1\zeta) + A_4K(u_2\zeta) + A_5\right], \tag{5.39}$$

where $A_2, A_3, A_4, A_5 \in \mathbb{R}$ are constants, and u_1 , u_2 are the pre-images in the ζ-plane of the extra line vortices. We shall map from the same annulus,$\mathcal{D} = \{\zeta; \rho < |\zeta| < 1\}$ to the complex z-plane, and form a velocity field using the Schwarz function method.

To be a physically admissible solution, this must again satisfy the following conditions:

1. $S_1 = S_2$, i.e. the two boundaries must have the same Schwarz function;
2. $z(\sqrt{\rho}) = 0$;
3. Any line vortices must be stationary;
4. The conformal map must be univalent.

Applying condition (1), we require that $\bar{z}(1/\zeta) = \bar{z}(\rho^2/\zeta)$. This reduces to the condition

$$2\log\rho = A_2 + A_3 + A_4. \tag{5.40}$$

Condition (2) gives

$$A_5 = -\frac{\log\rho}{2} - A_3K(u_1\sqrt{\rho}) - A_4K(u_2\sqrt{\rho}). \tag{5.41}$$

The line vortex circulations will be given by

$$\Gamma_c = \quad -i\omega_0\lambda\log(\rho)\sqrt{\rho}\hat{K}(1)z_\zeta(\sqrt{\rho}) \tag{5.42}$$

$$\Gamma_1 = \quad -\frac{i\omega_0\lambda}{2}A_3u_1\hat{K}(1)z_\zeta(u_1) \tag{5.43}$$

$$\Gamma_2 = \quad -\frac{i\omega_0\lambda}{2}A_4u_2\hat{K}(1)z_\zeta(u_2), \tag{5.44}$$

where Γ_c is the circulation of the vortex at $z = 0$, and Γ_1, Γ_2 the circulations of the vortices at $z = u_1$ and $z = u_2$ respectively. Recall also that the strength κ_c of each vortex is related to the circulation by $\kappa = \Gamma/2\pi$.

We now consider two specific distributions.

5.3.1 Extra line vortices on the real axis, equal strengths

Suppose we place two extra line vortices with equal circulations on the real axis, an equal distance either side of the central line vortex. Initially, we will have the two line vortices with equal vorticity, Γ_S.

We expect a relation to exist between θ and Γ_s. For this case, we set

$$u_1 = \sqrt{\rho}e^{i\theta} \quad u_2 = \sqrt{\rho}e^{-i\theta} = \bar{u_1}, \tag{5.45}$$

and

$$A_3 = A_4. \tag{5.46}$$

We then derive the condition

$$A_3 = \log\rho - \frac{A_2}{2}. \tag{5.47}$$

from the Schwarz function requirement (5.40), that the Schwarz functions on the two boundaries are equal. Note this has no θ dependence.

Condition (5.41) gives that

$$A_5 = -\frac{1}{2}\log\rho - (\log\rho - \frac{A_2}{2})\left[K(\sqrt{\rho}u_1) + K(\sqrt{\rho}\bar{u_1})\right]. \tag{5.48}$$

Note that as $\theta \to 0$, we recover $A_5 = -\frac{1}{2}\log\rho$, since $K(\rho) = 0$.

The stationarity condition for the satellite vortex at $\zeta = u_1$ is given by

$$\begin{aligned} A_2K(\frac{\rho^3/2}{u_1}) + (\log\rho - \frac{A_2}{2})K(\frac{\rho^2}{u_1^2}) + 2A_5 + A_2K\left(\frac{\sqrt{\rho}}{u_1}\right) + \\ (\log\rho - \frac{A_2}{2})K\left(\frac{\sqrt{\rho}}{u_1^2}\right) + (\log\rho - \frac{A_2}{2})\left[\frac{u_1\hat{K}(1)z_{\zeta\zeta}(u_1)}{2z_\zeta(u_1)} + \frac{\partial}{\partial\zeta}\left\{\zeta\hat{K}\left(\frac{u_1}{\zeta}\right)\right\}\right]_{\zeta=u_1} = 0, \end{aligned} \tag{5.49}$$

after recalling that $K(\sqrt{\rho}) = 0$. The equation for $\zeta = u_2$ is the complex conjugate of this. The central line vortex has the stationarity condition

$$\begin{aligned}(\log\rho - \frac{A_2}{2})K(\frac{\rho^{3/2}}{u_1}) + (\log\rho - \frac{A_2}{2})K(\frac{\rho^{3/2}}{u_2}) + 2A_5 + (\log\rho - \frac{A_2}{2})K(\frac{u_1}{\sqrt{\rho}}) + \\ (\log\rho - \frac{A_2}{2})K(\frac{\bar{u}_1}{\sqrt{\rho}}) + A_2\left\{\frac{\sqrt{\rho}\hat{K}(1)z_{\zeta\zeta}(\sqrt{\rho})}{2z_\zeta(\sqrt{\rho})} + \frac{\partial}{\partial\zeta}\left[\zeta\hat{K}\left(\frac{\sqrt{\rho}}{\zeta}\right)\right]_{\zeta=\sqrt{\rho}}\right\} = 0.\end{aligned} \tag{5.50}$$

Then given λ and ω_1, we set ρ and use Newton iteration on A_2 and θ_0 to solve the stationarity conditions. Although these are complex equations, the imaginary part is found to be identically zero, and hence the problem is tractable.

5.3.2 Results

Results are shown for $\lambda = 1$ and $\omega_0 = 1$. Figure 5.4 shows solutions with varying area. As with the single vortex case, we consider area rather than ρ as it is a physically interpretable quantity. With fixed $\lambda = 1$, $\omega_0 = 1$, and $A_3 = A_4$, we find a single parameter family of exact steady solutions, parameterised by the patch area in a single period. The strengths of the line vortices are given by (5.42). Due to the zero circulation of the solutions,

$$\Gamma_c + 2\Gamma_s = A, \tag{5.51}$$

where A is the patch area.

As might be expected from comparison with the single vortex solutions, in the limit $\rho \to 1$ the patch tends to two touching shielded Rankine vortices, separated at the point where the boundary would touch at $z = 0$, by a central line vortex. The strength of the central line vortex in this limit tends to zero. As ρ decreases and hence the patch area increases, the boundary becomes less curved, and as $\rho \to 0$, tends to a band of constant vorticity with height $z(1) - z(\rho)$. The positions of the satellite vortices remain at roughly ±0.25.

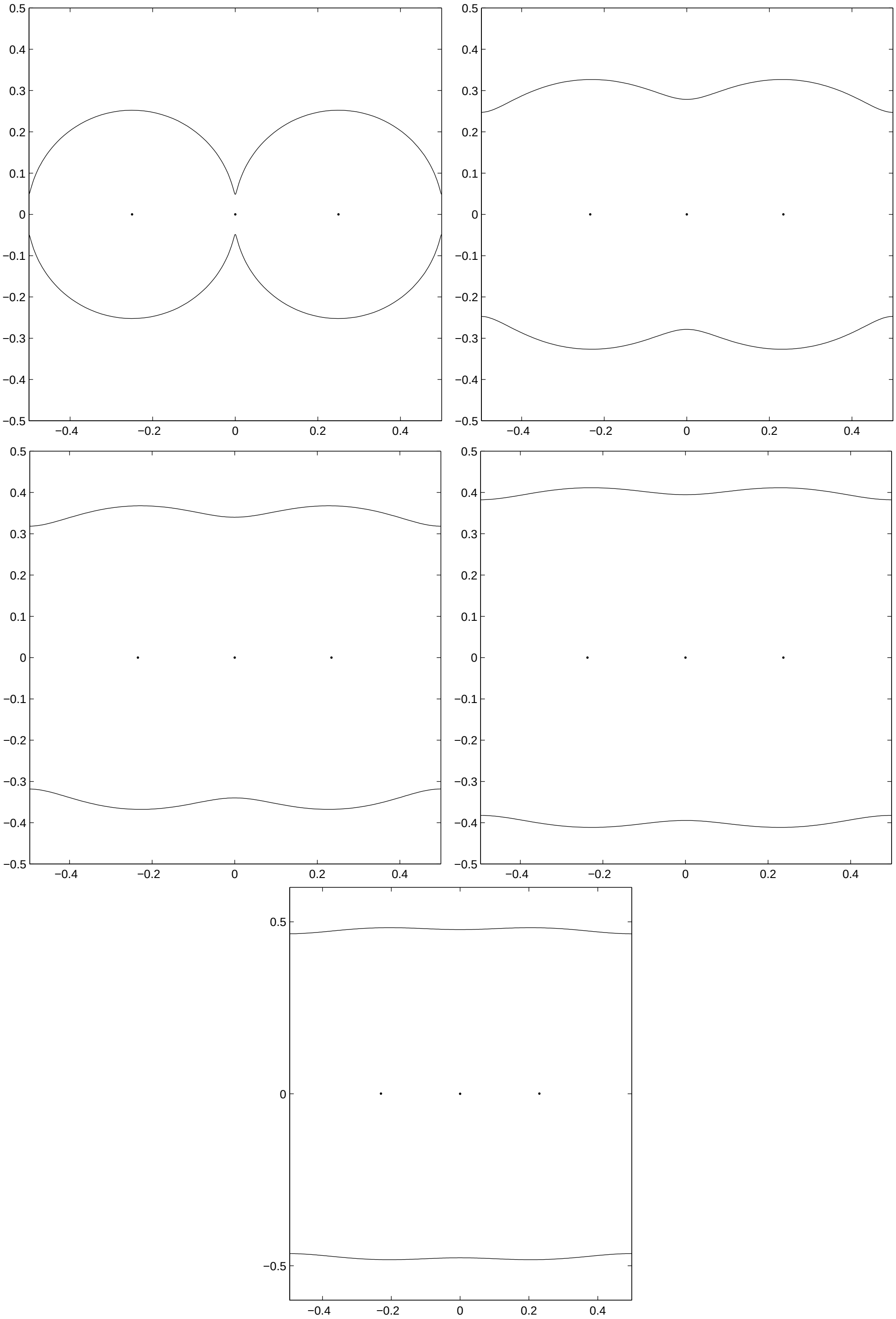

Fig. 5.4: Singly periodic patch solutions with three point vortices on the real axis, $Q = 1$. Top left panel shows the solution with area 0.4, $\kappa_c = 10^{-5}, \kappa_s = 0.2$. The x-coordinates for the line vortex are given by $x = \pm 0.25$. Top right panel shows the solution with area $0.6, Q = 1, \kappa_c = -0.025119, \kappa_1 = 0.31256, \kappa_2 = 0.31256$. The x-coordinates for the line vortex are given by $x = \pm 0.2339$. Middle left panel shows the solution with area $0.7, Q = 1, \kappa_c = -0.030407, \kappa_1 = 0.3652, \kappa_2 = 0.3652$. The x-coordinates for the line vortex are given by $x = \pm 0.2345$. Middle right panel shows the solution with area $0.8, Q = 1, \kappa_c = -0.032017, \kappa_1 = 0.41601, \kappa_2 = 0.41601$.The x-coordinates for the line vortex are given by $x = \pm 0.2373$. Bottom panel shows the solution with area $0.95, Q = 1, \kappa_c = -0.072082, \kappa_1 = 0.51104, \kappa_2 = 0.51104$.The x-coordinates for the line vortex are given by $x = \pm 0.2302$.

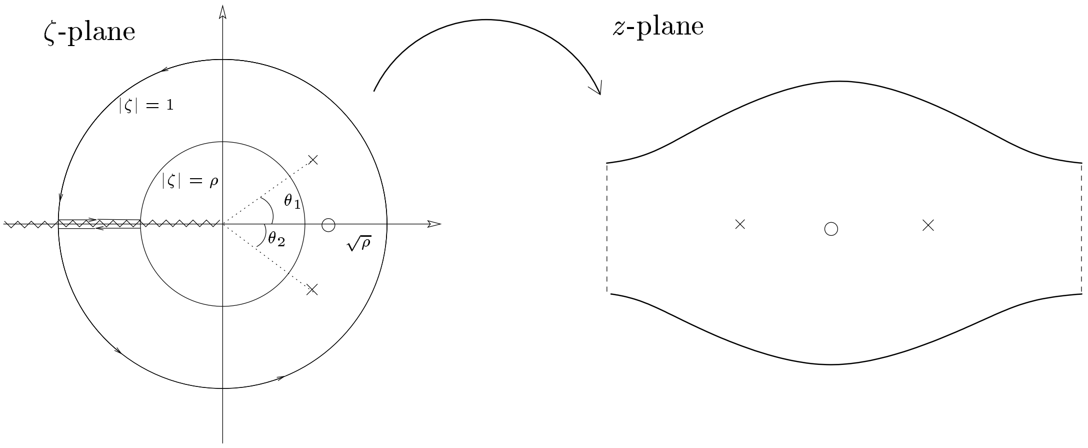

Fig. 5.5: Conformal mapping from ζ-plane annulus to the z-plane, with three line vortices on the real axis.

5.4 Real axis, unequal vortex strengths

Suppose that the strength of the two satellite vortices in (5.39) are no longer equal. Then we postulate now that the pre-images of the satellite line vortices will be given by (5.42)

$$u_1 = \sqrt{\rho}e^{i\theta_1}, \quad u_2 = \sqrt{\rho}e^{i\theta_2}. \tag{5.52}$$

If we now define some ratio, $A_4/A_3 = Q$, then the condition $2\log\rho = A_2 + A_3 + A_4$ implies that

$$A_3 = \frac{2\log\rho - A_2}{(1+Q)}, \tag{5.53}$$

with the case $Q = -1$, i.e. satellites of opposite polarity, excluded.

Then requiring that $z(\sqrt{\rho}) = 0$, we see that

$$A_5 = -\frac{\log\rho}{2} - A_3K(u_1\sqrt{\rho}) - QA_3K(u_2\sqrt{\rho}). \tag{5.54}$$

The stationarity condition for the central line vortex is given by

$$\begin{aligned} A_3K(\frac{\rho^{3/2}}{u_1}) + QA_4K(\frac{\rho^{3/2}}{u_2}) + A_3K\left(\frac{u_1}{\sqrt{\rho}}\right) + A_4K\left(\frac{u_2}{\sqrt{\rho}}\right) \\ +A_2\left\{\frac{\sqrt{\rho}\hat{K}(1)z_{\zeta\zeta}(\sqrt{\rho})}{2z_\zeta(\sqrt{\rho})} + \frac{\partial}{\partial\zeta}\left[\zeta\hat{K}\left(\frac{\sqrt{\rho}}{\zeta}\right)\right]_{\zeta=\sqrt{\rho}}\right\} = 0. \end{aligned} \tag{5.55}$$

For the satellite line vortex at $z(u_1)$, we have

$$A_2 K\left(\frac{\rho^{3/2}}{u_1}\right) A_3 K\left(\frac{\rho^2}{u_1^2}\right) + QA_3 K\left(\frac{\rho^2}{u_1 u_2}\right) + A_2 K\left(\frac{\sqrt{\rho}}{u_1}\right) + QA_3 K\left(\frac{u_2}{u_1}\right) + 2A_5$$
$$+A_3\left[\frac{u_1 \hat{K}(1) z_{\zeta\zeta}(u_1)}{2z_\zeta(u_1)} + \frac{\partial}{\partial\zeta}\left\{\zeta\hat{K}\left(\frac{u_1}{\zeta}\right)\right\}\right]_{\zeta=u_1} = 0, \tag{5.56}$$

and for the satellite at $z(u_2)$ that

$$A_2 K\left(\frac{\rho^{3/2}}{u_2}\right) A_3 K\left(\frac{\rho^2}{u_1 u_2}\right) + QA_3 K\left(\frac{\rho^2}{u_2^2}\right) + 2A_5 A_2 K\left(\frac{\sqrt{\rho}}{\zeta}\right) + A_3 K\left(\frac{u_1}{u_2}\right)$$
$$+QA_3\left[\frac{u_2 \hat{K}(1) z_{\zeta\zeta}(u_2)}{2z_\zeta(u_2)} + \frac{\partial}{\partial\zeta}\left\{\zeta\hat{K}\left(\frac{u_2}{\zeta}\right)\right\}\right]_{\zeta=u_2} = 0. \tag{5.57}$$

We here have only three real unknowns, A_2, θ_1 and θ_2, and three complex equations to be satisfied. However, numerical examination shows that the imaginary part of (5.55), (5.56) and (5.57) are zero uniformly, although no analytic proof of this seems apparent. The three unknowns, A_2, θ_1 and θ_2 are then sufficient for a well posed problem, which is solved using a 3-d Newton iteration scheme.

5.4.1 Results

Results are presented for $Q > 1$, $Q < 1$ being the reflection in the imaginary axis. Point vortex circulations and strengths are again obtained using (5.42). These solutions form a two parameter family, parameterised by the patch area and the ratio of vortex strengths, Q. Initial parameter values for iteration by the three dimensional Newton routine were obtained from the $Q = 1$ limit. A solutions for $Q = Q_1 = Q_0 + \epsilon$ was then increased, and the parameters obtained for the Q_n solution then provided initial estimates for Q_{n+1} parameters. Figure 5.6 presents solutions with a range of patch area, for fixed ratio Q. It can be seen that, as with the equal outer vortex case, $Q = 1$, decreasing area is accomplished through the patch becoming more circular. Due to the strengths of the outer vortices being equal in this case, the symmetry of the pair of almost joined shielded Rankine vortices is not achieved. As the area increases, the patch boundary becomes less curved, and tends to some distortion of the channel observed with $Q = 1$. Due to the asymmetry of the vortex strengths, the limiting straight boundary limit was not observed.

Figure 5.7 shows, for fixed area, the effects of increasing Q. An asymmetry in the boundary is created , which increases in size until, for large Q, the boundary is close to a series of co-joined circles, with a centre displaced from the origin, so that a single circle spans more than one period. The relatively large strength of the left hand vortex here prevents the boundary pinching at the point where the circles join.

Figure 5.8 plots graphs of vortex strength against the ratio Q. As Q increases, the equilibria for all areas have a weak central vortex and one weak outer vortex. Recall that the aggregate strength of the line vortices is a constant (as area is held constant). The rearrangement of the patch shape as Q increases from the symmetric $Q = 1$ configuration is initially accompanied by an the negative strength of the central vortex becoming more negative. As Q increases, and the patch tends towards a circle with the centre to the right of the origin (see Fig. 5.7), the central and right-hand vortices become weak and approach each other. An isolated pair of opposite signed point vortices would translate upwards, but the effects of the large positive left hand line vortex and vortices present in the other periods prevents this.

It has not been possible to find solutions of this form with point vortices placed away from the real axis. In [40], it is noted that non-zero circulation singly periodic point vortex arrays containing three vortices per period are constrained in the positioning of the point vortex. It is possible that a similar constraint exists when a patch is superposed also. Zero circulation point vortex arrays are not of interest in this case, as we require the circulation of the total period, including the patch, to be equal to zero.

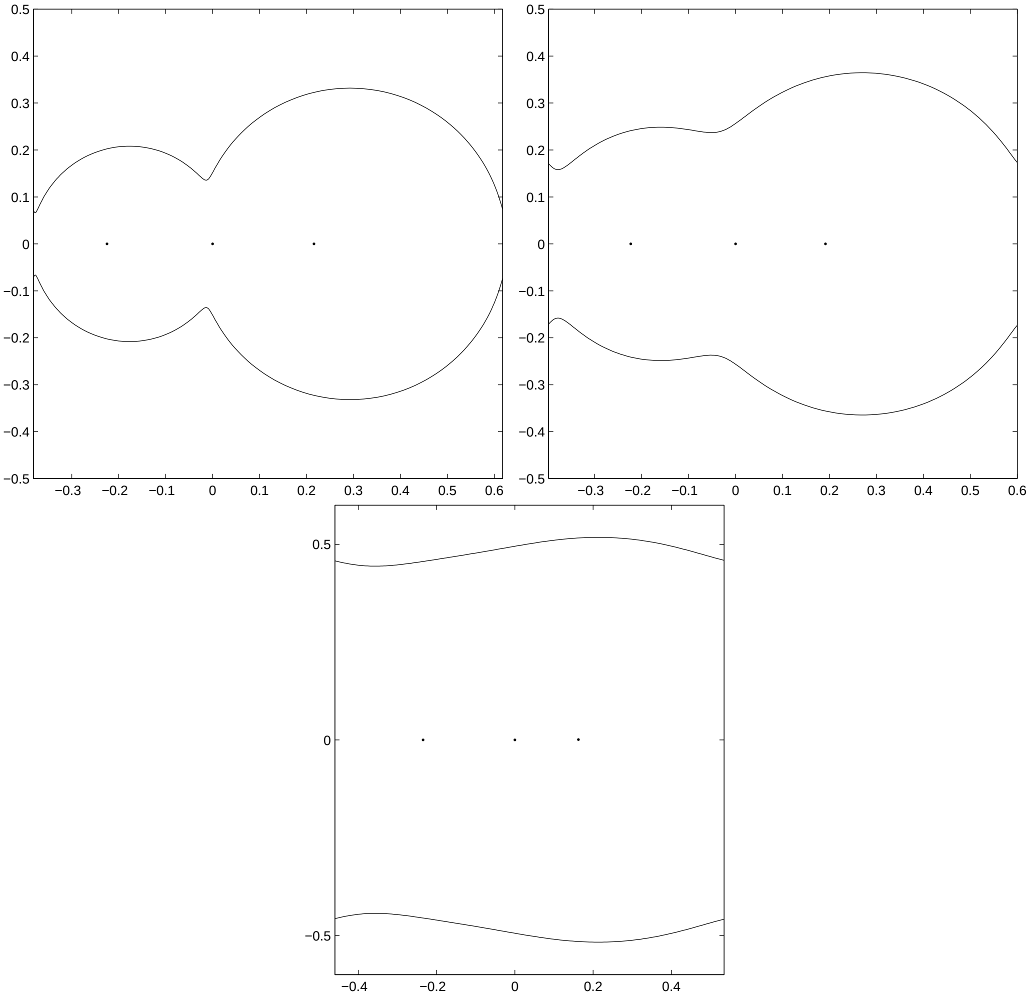

Fig. 5.6: Singly periodic patch solutions with three point vortices on the real axis, with varying area, $Q = 1.65$. Top left panel shows the solution with area 0.4, ,$Q = 1.65, \kappa_c = -0.015878, \kappa_1 = 0.20364, \kappa_2 = 0.2122$. $x_1 = 0.2159$, $x_2 = -0.2248$. Top right shows the solution with area 0.5, $Q = 1.6667, \kappa_c = -0.04773, \kappa_1 = 0.24909, \kappa_2 = 0.29864 . x_1 = 0.1914$, $x_2 = -0.2231$. Bottom panel shows the solution with area 0.95, $Q = 1.65, \kappa_0 = -0.12264, \kappa_1 = 0.41543, \kappa_2 = 0.65721$. $x_1 = 0.1626$, $x_2 = -0.2344$.

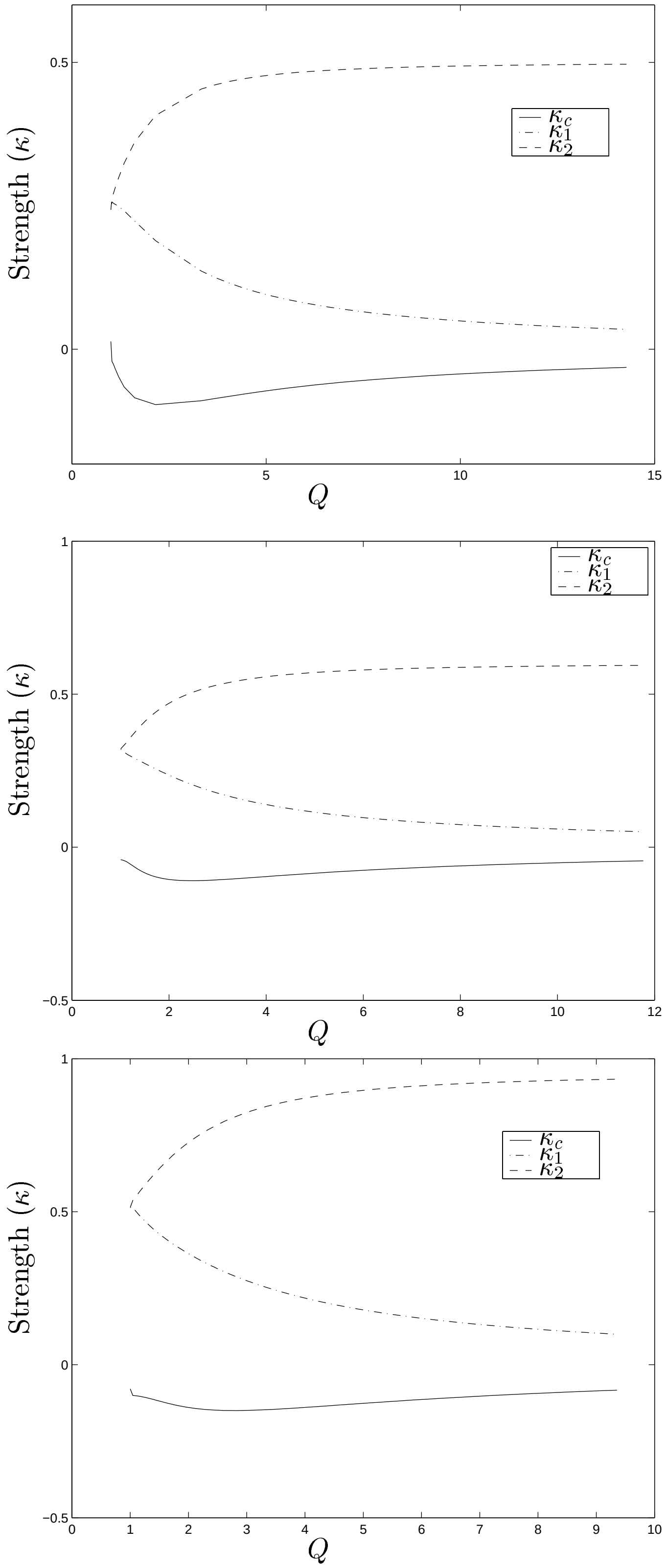

Fig. 5.7: Plot of vortex strengths κ_c, κ_1 and κ_2 against the ratio Q. Top graph shows plot for area $= 0.5$. Middle graph shows area $= 0.6$. Bottom graph shows area $= 0.95$.

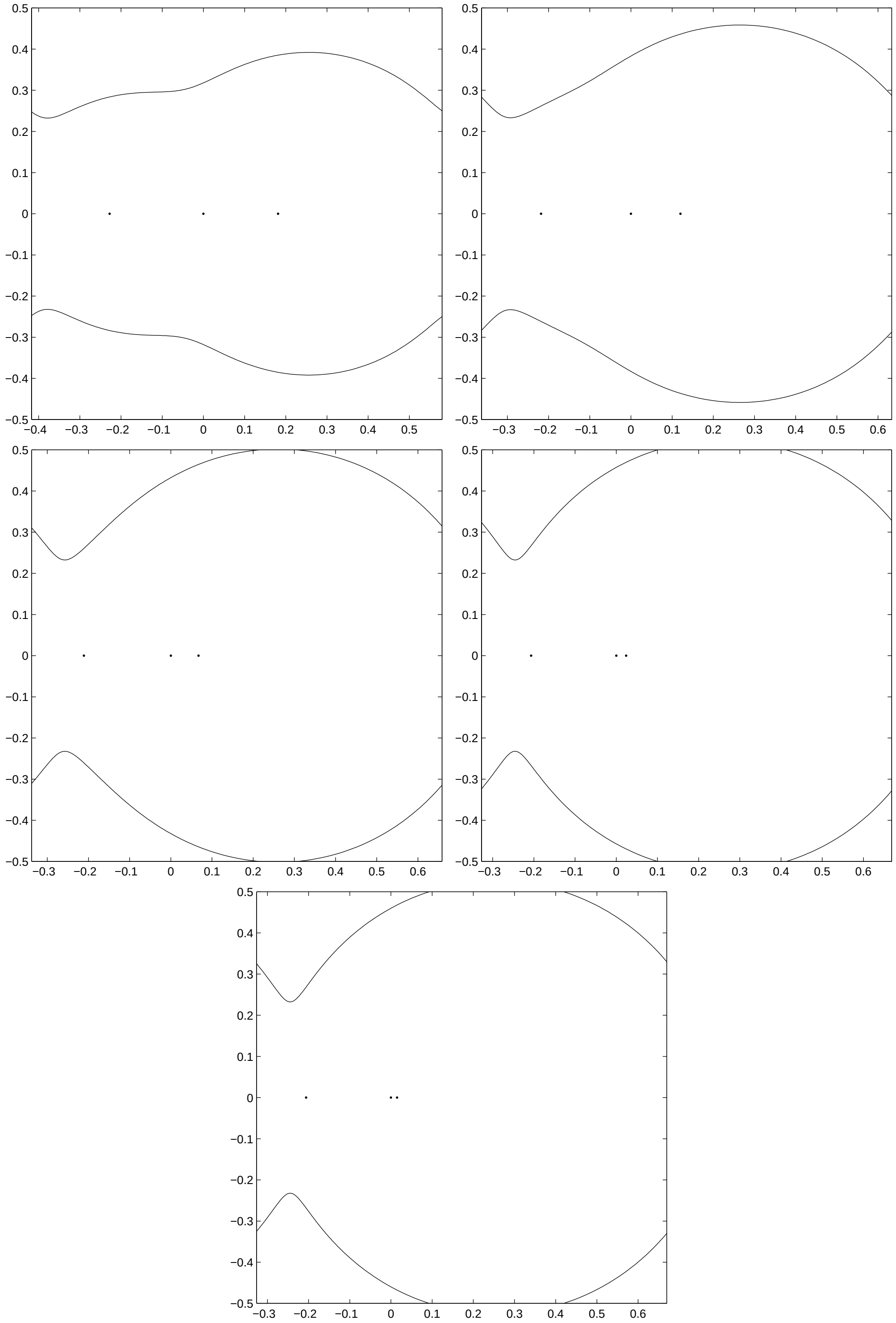

Fig. 5.8: Singly periodic patch solutions with three point vortices on the real axis, with varying Q, area $= 0.6$. Top left panel shows the solution with area $0.6, Q = 1.65, \kappa_0 = -0.067418, \kappa_1 = 0.28621, \kappa_2 = 0.3812$. The x-positions are given by $x_1 = 0.1813$, $x_2 = -0.2277$. Top right panel shows the solution with area $0.6, Q = 2.7, \kappa_0 = -0.10459, \kappa_1 = 0.23413, \kappa_2 = 0.47046$. $x_1 = 0.1295$, $x_2 = -0.2197$. Middle left panel shows the solution with area $0.6, Q = 4.7, \kappa_0 = -0.10062, \kappa_1 = 0.1541, \kappa_2 = 0.54653$. $x_1 = 0.0704$, $x_2 = -0.2115$. Middle right panel shows the solution with area $0.6, Q = 12.5, \kappa_0 = -0.051834, \kappa_1 = 0.060369, \kappa_2 = 0.59147$, $x_1 = 0.0250$, $x_2 = -0.2067$. Bottom panel shows the solution with area $0.6, Q = 20, \kappa_0 = -0.034293$, $\kappa_1 = 0.037696, \kappa_2 = 0.5966$. $x_2 = 0.0148$, $x_1 = -0.2061$.

CHAPTER 6

Conclusion and further work

The intention of the preceding chapters has been to develop the techniques presented by Crowdy [3] for the creation of vortical equilibria of the two dimensional Euler equations combining patch and point vorticity. This combination has not been considered on the plane before [3], although we argue that it can be motivated by the form of point vorticity on the sphere. To this end, Chapter 2 reviews the methods of [3] before presenting a stability analysis of Crowdy's planar multipolar solutions. Apart from the tripolar distribution, stability results are shown to correspond to the observed atmospheric, laboratory and numerical multipolar distributions of other researchers in both linear and non-linear perturbations. The linear results are also found to indicate the stability under non-linear perturbations. The quadrupolar results are found to be neutrally stable for the whole range of parameter a. The tripolar case is suggested to be unstable due to the twin requirement of zero circulation and being non-rotating. It is to be remembered however, that this is an exact class of solutions, and does not cover the whole class of possible multipolar vortical equilibria. Hence the fact that stability of this particular case does not correspond to the more general observations is not completely surprising. However, the remaining cases do indeed mirror other observed stability.

Chapter 3 examines fluid flow on the surface of the sphere. Isolated point vortices on the sphere are required to be combined with a patch of vorticity, to ensure that the integral of vorticity over the surface is equal to zero. The form of the equations of motions utilising the stereographic are derived. Using this, the spherical equivalent of the class of multipolar solutions presented in [3] is presented. This new class is shown to be a two-parameter family, as opposed to the one-parameter family on the plane. Solutions are presented for a range of satellite ring latitude and the area of the sphere covered by the patch of constant vorticity. In the case where the patch covers the whole surface of the sphere, the point vortex strengths are shown to tend to that of a purely point vortex model.

Chapter 4 examines the linear stability of two fundamental spherical vortex equilibria, before examining the stability of the full multipolar solutions on the surface of the sphere. The first model to be examined is the ring of N point vortices of identical strength around a central line vortex, an extension of the planar Morikawa and Swenson distribution. The spherical geometry is found to be a destabilising effect on the ring of satellite vortices, and a stabilising effect for the central vortex, until the satellites are far enough from the south pole for the motion to decouple. When the ring of point vortices is near the north pole, then, the stability is identical to a ring of vortices with no central vortex. Subsequently, the stability of a generalisation of the shielded Rankine vortex is studied. This is found to be neutrally stable for all θ_0, the latitudinal angle of the patch boundary. As the patch boundary approaches the north pole, and hence covers the whole surface of the sphere, eigenvalues $\pm i/2$ are recovered, as with the planar case. The final part of this chapter is concerned with the linear stability of the full multipolar solutions. For the tripole, stability results are qualitatively the same as on the plane. For solutions with greater numbers of points vortices, however, it can be seen that the patch boundary begins to exhibit instabilities when sufficiently deformed from the circular limit. These dominate the stability behaviour as the patch approaches the line vortices, whereas when the patch is far from the point vortices, stability is dominated by the stability behaviour of the point vortex limit. In general then, we find that for $n > 2$, the curvature effects of the sphere provide a destabilising influence on the patch to point vortex interactions.

In conclusion then, the study here of stability on the surface of the sphere suggests two main instability procedures. With the purely point vortex model, for $n > 3$ the ring of vortices is less stable on the sphere than on the plane. This is due to the potentially stabilising effect of the central line vortex being shielded by the curvature. So in this case the greater instability is effectively caused by a stabilising influence becoming masked. In the full multipolar solutions, the increased instability is conjectured to be caused by interactions of the shape modes forming the deformation.

In Chapter 5, we present a class of singly periodic solutions to the Euler equations with both patch and point vorticity. Solutions are found with one vortex per period, three vortices per period with identical circulation of the outer vortices, and three vortices per period with differing circulation outer vortices. All of these cases possess a limit which tends to a band of constant vorticity. The single point vortex per period case also has a limit in which the distribution tends to an infinite series of touching shielded Rankine vortices. For the case of three vortices per period with equal circulation outer vortices, there exists a limit which tends to two almost touching shielded Rankine vortices per period, with a single very weak line vortex between them. It is noted that this limiting case of the shielded Rankine vortex is achieved in each of the three classes of solution considered. This emphasizes the important nature of this as the simplest example of combined point and patch vorticity.

6.1 Further work

There are a number of extensions to the work presented here which could be undertaken, of which a couple are presented. Contour dynamics routines on the sphere or an infinite periodic region could have point vortex equations of motion added, which could be used to examine the non-linear stability of the presented solutions. Previous work, both here, and in [34] suggest that the nonlinear stability boundaries of this type of distribution is closely related to linear stability.

The linear stability of the singly periodic solutions could also be examined. Following the method of §2.5, this would involve replacing the Schwarz function term with the expression for point vortices placed in the relevant positions, and some irrotational correction to the flow. Hence for the single point vortex case per period, the expression

$$u - iv = \left\{ \begin{array}{ll} 0 & z \in D_{upper} \\ 2i\left(\bar{z} - \frac{\Gamma_0}{2\lambda}\cot(\pi z/\lambda) - F(z)\right) & z \in D \\ 0 & z \in D_{lower} \end{array} \right\}. \qquad (6.1)$$

would be formed, the cot term representing the infinite row of vortices. The conformal map would then be perturbed, and a Riemann-Hilbert problem then be formed, to allow the unknown perturbations to the upper and lower flows to be expanded in terms of the perturbation coefficients. Two kinematic boundary conditions would then results, as well as the line vortex equations of motion.

APPENDIX A

Patch Area

In spherical polars, we have that

$$\mathrm{d}\sigma = \sin\theta \mathrm{d}\theta \mathrm{d}\phi \tag{A.1}$$

If x, y are coordinates on the stereographically projected plane such that $\zeta = x + iy$, then

$$\begin{aligned} \mathrm{d}\theta \mathrm{d}\phi &= \left| \frac{\partial(\theta, \phi)}{\partial(x, y)} \right| \mathrm{d}x \mathrm{d}y \\ &= \frac{(1 - \cos\theta)^2}{\sin\theta} \\ &= \frac{4}{(1 + \zeta\bar{\zeta})^2}, \end{aligned} \tag{A.2}$$

using (3.3).

Thus

$$\begin{aligned} \mathcal{A} &= \int\int_{\bar{D}} \mathrm{d}\sigma \\ &= \int\int_{\bar{D}} \frac{4 \mathrm{d}x \mathrm{d}y}{(1 + \zeta\bar{\zeta})^2} \\ &= \int\int_{\bar{D}} \frac{\partial}{\partial\bar{\zeta}} \left(\frac{4\bar{\zeta}}{(1 + \zeta\bar{\zeta})} \right) \mathrm{d}x \mathrm{d}y. \end{aligned} \tag{A.3}$$

Then applying the complex form of Greens Theorem,

$$\begin{aligned} \mathcal{A} &= \frac{1}{2i} \oint_{\partial D} \frac{4\bar{\zeta}}{(1 + \zeta\bar{\zeta})} \mathrm{d}\zeta \\ &= \frac{1}{2i} \oint_{|\eta|=1} \frac{4\zeta(\eta^{-1})\zeta_\eta(\eta)}{(1 + \zeta(\eta)\bar{\zeta}(\eta))} \mathrm{d}\eta. \end{aligned} \tag{A.4}$$

Note that for our conformal map, the integrand occur only at the positions of the point vortices, and the sum of the residues is $N\Gamma_s + \Gamma_c$,

$$\omega_0 \mathcal{A} = 4\pi(N\Gamma_s + \Gamma_c), \tag{A.5}$$

where Γ_s and Γ_c are given by (3.62).

References

[1] J. C. McWilliams, “The emergence of isolated coherent vortices in the turbulent flow.“, J. Fluid Mech., **146**, 21–43, 1984.

[2] J. C. McWilliams, “The vortices of two-dimensional turbulence.“, J. Fluid Mech., **219**, 21–43, 1990.

[3] D. Crowdy, “A class of exact multipolar vortices”, Phys. Fluids **11**, 2556, 1997.

[4] D. Crowdy , M. Cloke, “Stability analysis of a class of two-dimensional multipolar vortex equilibria”, Phys. Fluids 1**4(6)**: 1862-1876, Jun 2002.

[5] D. Crowdy , M. Cloke, “Analytical solutions for distributed multipolar vortex equilibria on a sphere”, Phys. Fluids **15 (1)**: 22-34, Jan 2003

[6] , D.W.Moore and P.G. Saffman, “The density of organised vortices in a turbulent mixing layer”, J. Fluid Mech., 69, 465-73

[7] , G. F. Carnevale and R. C. Kloosterziel, “Emergence and evolution of triangular vortices”, J. Fluid Mech. **259**, 305, 1994.

[8] R. C. Kloosterziel and G. F. Carnevale, “On the evolution and saturation of instabilities of two–dimensional isolated circular vortices”, J. Fluid Mech. **388**, 217, 1999.

[9] X. J. Carton, “On the merger of shielded vortices“, Europhys. Lett. **18** 697, 1992

[10] X. J. Carton, G. R. Flierl and L. M. Polvani, “The generation of tripoles from unstable axisymmetric isolated vortex structures”, Europhys. Lett. **9**, 339, 1989.

[11] L. M. Polvani and X. J. Carton, “The tripole: a new coherent vortex structure of incompressible two–dimensional flows”, Geophys. Astrophys. Fluid Dyn. **51**, 87, 1990.

[12] D. G. Dritschel, "Contour surgery: A topological reconnection scheme for extended interactions using contour dynamics", J. Comput. Phys. **77**, 240, 1988.

[13] P. G. Saffman, *Vortex Dymamics* (Cambridge University Press, Cambridge, 1992).

[14] M. J. Ablowitz, A. S. Fokas, *Complex Analysis: Introduction and Applications* (Cambridge Texts in Applied Maths, CUP, 2003).

[15] J. Jimenez, "Linear stability of a non-symmetric, inviscid Karman street of small uniform vortices", J. Fluid Mech., **189**, 337-48, 1988.

[16] E. A. Overman, "Steady-state solutions of the Euler equations in two dimensions; local analysis of limiting V-states", SIAM J. Appl. Math., **46**, 765, 1986.

[17] G.R. Flierl,"On the instability of geostrophic vortices", J. Fluid Mech. **197**, 349 (1988).

[18] Y.G. Morel and X. J. Carton, "Multipolar vortices in two-dimensional incompressible flows", J. Fluid Mech. **267**, 23 (1994).

[19] G.K. Morikawa and E.V. Swenson, "Interacting motion of rectilinear geostrophic vortices", Phys. Fluids **14**, 1058 (1971).

[20] D. A. Schecter, D. H. E. Dubin, K. S. Fine and C. F. Driscoll, "Vortex crystals from two-dimensional Euler flow: Experiment and simulation", Phys. Fluids **11(4)**, 905 (1998)

[21] J. J. Thompson, "On the motion of vortex rings", Macmillan, London, 1883.

[22] H. P. Greenspan, "The Theory of Rotating Fluids", Cambridge University Press, 1968.

[23] D. Durkin and J. Fajans, "Experimental Dynamics of a Vortex within a Vortex", Physical Rev. Letters **85(19)**, 4052 (2000)

[24] D. Z. Jin and D. H. E. Dubin, "Point vortex dynamics within a background vorticity patch", Phys. Fluids **31(3)**, 677 (2001).

[25] G. S. Deem and N. J. Zabusky, "Vortex waves: stationary V-states, interactions,recurrence and breaking," PHys. Rev. Lett. **40**, 859 (1978).

[26] V. A. Bogomolotov, “The dynamics of vorticity on a sphere”, Fluid Dynamics, **13 (6)**, 863–870, 1977.

[27] V.A. Bogomolotov, “Two-Dimensional Fluid Dynamics on a Sphere”, Atmospheric and Oceanic Physics, **15 (1)**, 18–22, 1979.

[28] Lorenzo M. Polvani, David G. Dritschel, “Wave and vortex dynamics on the surface of a sphere”, J. Fluid Mech. **255**, 35–64, 1993

[29] C. Lim, J. Montaldi, M. Roberts, “Relative equilibria of point vortices on the sphere“, Physica D, **148**, 97–135, 2001

[30] Y. Kimura, “Vortex motion on surfaces with constant curvature“, Proc. R. Soc. Lond. A, **455**, 245–259, 1999

[31] H. M. Wu, E. A. Overman, N. J. Zabusky, “Steady-state solutions of the Euler equations in two dimensions: rotating and translating V-states with limiting cases. I. Numerical algorithms and results.” J. Comput. Phys., **53 (1)**, 42–71,1984.

[32] J. J. Thompson, *A treatise on the motion of vortex rings* (Macmillan, 1883).

[33] D. G. Dritschel, “The stability and energetics of corotating uniform vortices”, J. Fluid Mech. **157**, 95-134, 1985.

[34] S.Boatto, H. E. Cabral, “Nonlinear Stability of a Latitudinal Ring of Point-Vortices on a Nonrotating Sphere”, SIAM J. App. Maths **64(1)**, 216 - 230, 2003

[35] S. G. Krantz, “The Riemann Mapping Theorem.”, *Handbook of Complex Variables* (Birkhauser, 1999), pp. 86-87

[36] Y. Kimura, H. Okamoto, “Vortex motion on a sphere”, J. Phys. Soc. Japan **56(12)**, 4203–4206, 1987

[37] M. Dibattista,L. M. Polvani, “Barotropic vortex pairs on a rotating sphere”, J. Fluid Mech. **358**, 107–133, 1998.

[38] P. J. Davis, *The Schwarz function and its applications* (Carus Mathematical Monographs, The Mathematical Association of America), 1974.

[39] H. Lamb, *Hydrodynamics*, (Cambridge University Press), 1932

[40] M. A. Stremler, "Relative equilibira of singly peridioc point vortex arrays", Physics of fluids, **15(12)**, 3767–3775, 2003.

[41] R. D. Pingree, B. LeCann, "Three anticyclonic slope water oceanic eddies (swoddies) in the southern Bay of Biscay, Deep-Sea Res., Part A **39**, 1147, 1992.

[42] Shian-Jiann Lin, "Contour Dynamics of Tornado-like Vortices", J. Atmos. Sc., **4918**, 1745, 1991.

[43] J. Snow, "A review of recent advances in Tornado Vortex Dynamics", Rev. Geo. Sp. Phys., **204**, 953, 1982.

[44] D.I. Meiron, P.G. Saffman and J.C. Schatzman, "The linear two-dimensional stability of inviscid vortex streets of finite-cored vortices", J. Fluid Mech.,**147**, 187, 1984.

[45] D.J. Hill, "Vortex Dynamics in Wake Models", PhD Thesis, Caltech, 1998

[46] Th. von Karman, "Uber den Mechanismus des Widerstandes, den ein bewegter Korper in einer Flussigkeit erfahrt. 1. Teil ", Gottinger Nachrichten Math-Phys. Klasse **509**, 1911

[47] Th. von Karman, "Uber den Mechanismus des Widerstandes, den ein bewegter Korper in einer Flussigkeit erfahrt. 2. Teil ", Gottinger Nachrichten Math-Phys. Klasse **547**, 1912

[48] H. Aref, M.A. Stremler, "On the motion of three vortices in a periodic strip", J. Fluid Mech, **314**, 1 (1996)

[49] P.G. Saffman, J.C. Schatzman, " An inviscid model for the vortex street wake", J. Fluid Mech., **122**, 467-86 (1982)

[50] P.G. Saffman, R. Szeto, "Structure of a linear array of uniform vortices", Stud. Appl. Math. **65**, 223 (1981)

[51] R.T. Pierrehumbert and S.E. Widnall, "The structure of organised vortices in a free shear layer", J. Fluid Mech. **102**, 301 (1981)